A Proposal for the DarkLight Experiment at the Jefferson Laboratory Free Electron Laser

J. Balewski, J. Bernauer, W. Bertozzi, J. Bessuille, B. Buck, R. Cowan, K. Dow, C. Epstein, P. Fisher *, S. Gilad, E. Ihloff, Y. Kahn, A. Kelleher, J. Kelsey, R. Milner, C. Moran, L. Ou, R. Russell, B. Schmookler, J. Thaler, C. Tschalaer, C. Vidal, A. Winnebeck

Laboratory for Nuclear Science, Massachusetts Institute of Technology, Cambridge, MA 02139, USA and the Bates Research and Engineering Center, Middleton MA 01949

S. Benson, C. Gould, G. Biallas, J. Boyce, J. Coleman, D. Douglas, R. Ent, P. Evtushenko, H. C. Fenker, J. Gubeli, F. Hannon, J. Huang, K. Jordan, R. Legg, M. Marchlik, W. Moore, G. Neil, M. Shinn, C. Tennant, R. Walker, G. Williams, S. Zhang

Jefferson Lab, 12000 Jefferson Avenue, Newport News, VA 23606

M. Freytsis

Physics Dept., U.C. Berkeley, Berkeley, CA

R. Fiorito, P. O'Shea

Institute for Research in Electronics and Applied Physics University of Maryland, College Park, MD

R. Alarcon, R. Dipert

Physics Department, Arizona State University, Tempe, AZ

G. Ovanesyan

Los Alamos National Laboratory, Los Alamos NM

T. Gunter, N. Kalantarians, M. Kohl

Physics Dept., Hampton University, Hampton, VA 23668 and Jefferson Lab, 12000 Jefferson Avenue, Newport News, VA 23606

I. Albayrak, M. Carmignotto, T. Horn

* Corresponding author (fisherp@mit.edu)

Physics Dept., Catholic University of America, Washington, DC 20064

D. S. Gunarathne, C. J. Martoff, D. L. Olvitt, B. Surrow, X. Li

Physics Dept., Temple University, Philadelphia, PA 19122

E. Long

Physics Dept., Kent State University, Kent, OH, 44242

R. Beck, R. Schmitz, D. Walther

University Bonn, D - 53115 Bonn Germany

K. Brinkmann, H. Zaunig

. Physikalisches Institut Justus-Liebig-Universitt Giessen, D-35392 Giessen Germany

J.Kossler

Physics Dept., College of William and Mary, Williamsburg VA 23185

(Dated: May 4, 2012)

New theories of dark matter predict A' gauge bosons in the mass range of 0.01–10 GeV that couple to charged fermions with a strength of $\alpha'/\alpha_{\rm EM} = 10^{-4}$ of the photon or less. We propose to design, construct and operate an experiment called DarkLight (Detecting A Resonance Kinematically with eLectrons Incident on a Gaseous Hydrogen Target) to use the 1 MW 100 MeV electron beam at the Jefferson Lab Free Electron Laser incident on a 10^{19}cm^2 thick target to study the process $e^- + p \rightarrow e^- + p + e^- + e^+$. A dark force particle would show up as a narrow resonance in the radiated $e^+ - e^-$ system. Our experiment would explore the A' mass region 10-100 MeV and couplings as low as $\alpha' \sim 10^{-9}$ with 1/ab of data, which would require 60 days of data taking (assuming 100% efficiency) at the Jefferson Lab Free Electron Laser. We also plan for 30 days of running (assuming accelerator 100% efficiency) for beam studies, calibration and commissioning.

I. INTRODUCTION

Dark matter comprises 23% of the energy of the universe, and in the past ten years detection of dark matter and elucidation of its nature has moved to the forefront of experimental particle physics. Until recently, axions and weakly interacting massive particles (WIMPS) were the favored candidates and the focus of experimental investigation. Recent results, however, from both underground and cosmic ray experiments suggest that dark matter may be explained by a new theory that predicts vector or scalar bosons in the 10 MeV–10 GeV mass range that couple to electrons and positrons. Current experimental bounds limit the coupling to less than 10^{-2}–10^{-3} of the QED coupling, depending on the boson mass. This motivates us to consider experiments able to probe this new theory using a 1 MW, 100 MeV electron beam at the Jefferson Laboratory Free Electron Laser (FEL).

The DarkLight experiment is designed to search for a narrow resonance in the e+e- spectrum of elastic electron-proton scattering below pion threshold (i.e. at 100 MeV incident electron energy). Such a resonance will rest on the QED radiative tail. The final state proton recoils with low kinetic energy and DarkLight is designed to detect all final state particles using a large acceptance magnetic spectrometer. Vertex detectors for both recoil proton and final-state leptons are planned as well as large drift chambers in each sector of the magnetic toroid. The windowless gas target with multi-stage differential pumping system is embedded in the magnetic solenoid.

In December 2009, we submitted a letter of intent to carry out a new experimental search using the JLab FEL. The LOI was favorably reviewed by PAC35. We submitted a proposal to PAC37, requesting conditional approval to carry out beam tests and background measurements at the FEL to ensure we can achieve the beam control and background conditions necessary to carry out the experiment. Conditional approval was granted and we have a beam test scheduled for July 2012.

We now seek full approval for DarkLight, contingent on the success of the beam test. If DarkLight receives approval, this will allow the DarkLight collaboration to begin working with the DOE to secure funding for the operation of the FEL and construction of the detector. This proposal outlines our physics case (Section II), the FEL, backgrounds and detector designs (Sections III and V), expected performance (Section VI) and required resources and schedule (Section VII).

II. PHYSICS MOTIVATION

Recent interest in new light bosons has been sparked by their possible connection to dark matter physics. Here, we summarize the dark matter motivation for new A' bosons, and list some existing experimental constraints and search strategies.

A. Dark Matter and Dark Forces

By now, the gravitational evidence for dark matter is overwhelming [1–4]. While the precise nature and origin of dark matter is unknown, thermal freezeout of a weakly interacting massive particle (WIMP) is a successful paradigm that arises in many theories beyond the standard model. In the WIMP paradigm, dark matter is a TeV-scale particle that interacts with standard model particles via electroweak interactions. There is a wide range of searches that are sensitive to WIMPs, including direct detection in nuclear recoil experiments, direct production in collider experiments, and indirect detection in cosmic ray experiments.

In the past three years, however, a new paradigm for dark matter has emerged where dark matter is still a TeV-scale particle, but interacts dominantly through a "dark force" [5–8]. The carrier for this (short-range) force is a new GeV-scale particle, which we refer to as A'. To confirm this new paradigm, one would like to gain direct evidence for this A' boson.

These dark force models are motivated by three astrophysical anomalies that hint at excess electron/positron production in the Milky Way: the WMAP Haze [9, 10], the PAMELA, FERMI, and H.E.S.S. e^+/e^- excesses [11–14], and the INTEGRAL 511 keV excess [15, 16]. Such dark force models may also play a role in explaining the DAMA annual modulation signal [17]. Intriguingly, these anomalies can be explained in terms of dark matter annihilation, decay, and/or up-scattering in the Milky Way halo, though not with a standard WIMP. Rather, the peculiar features of these anomalies hint that dark matter is interacting with a light A' boson and that A' bosons are being produced in these dark matter interactions. To explain the anomalies while evading other astrophysical bounds, the A' boson must dominantly decay to electrons, muons, pions and/or taus, with little hadronic activity [18–20]. In addition, the most recent e^+e^- data gives a Standard Model prediction for $(g-2)_\mu$ which lies 3.6 σ away from the measurement [21]. Corrections from a dark force carrier in the 10–100 MeV range could explain this difference.

There are a variety of different dark force scenarios, but the most popular models invoke a new vector boson that kinetically mixes with the standard model photon [6, 7]:

$$\mathcal{L} = \epsilon F'_{\mu\nu} F^{\mu\nu}_{\rm EM}. \tag{1}$$

Through this "photonic portal", the A' boson inherits electromagnetic couplings, albeit with a reduced coupling strength

$$\alpha' = \epsilon^2 \alpha_{\rm EM}, \tag{2}$$

where $\alpha_{\rm EM} \sim 1/137$. The coupling α' and the mass $m_{A'}$ are both free parameters in these models. While other dark force models are equally plausible, we focus on the photonic portal case for concreteness, since it is the one most studied in the literature.

B. Searching for the Dark Force

Spurred by this new dark force paradigm, there has been much recent interest on how to find the light A' boson. There is a huge range of $\{\alpha', m_{A'}\}$ values that are consistent with existing astrophysical measurements, so multiple experiments will be necessary to probe the full parameter space. To date, a number of possible avenues for discovery have been explored, including:

- Production in lepton colliers through $e^+e^- \to \gamma + X$ [22–28]. When A' decays promptly to $\mu^+\mu^-$, existing B-factory data already places a constraint.

- Production in fixed-target experiments. Previous searches for light axions are also sensitive to A' bosons if A' is sufficiently long-lived [29, 30]. There are ongoing effort to do data mining on prior experiments, and Refs. [26, 31, 32] include a number of new fixed-target proposals. Of particular relevance for Jefferson Lab, the APEX experiment has completed a trial run in Hall A, and the HPS experiment is proposed for Hall B.

- Rare meson decays [23, 26, 33, 34]. Any meson decay that yields a photon could have a suppressed branching fraction to a dark photon. In particular, a reanalysis of KTeV data [35] would be sensitive to $\pi^0 \to \gamma + X$ with $X \to e^+e^-$.

- Production in fixed-target experiments with a positron beam [36].

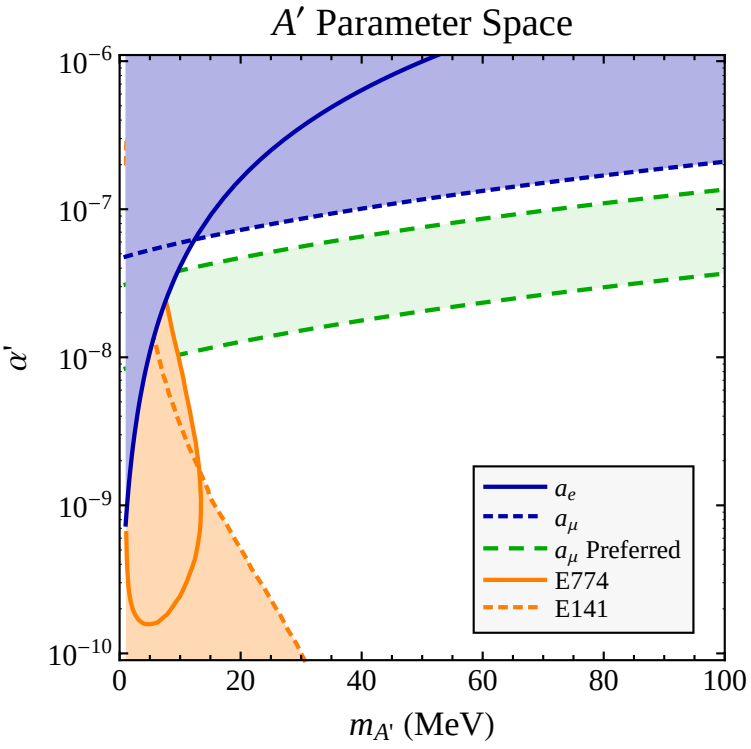

FIG. 1: The A' boson parameter space considered in the proposed search. The blue shaded regions correspond to bounds on the anomalous magnetic moment of the electron (a_e) and muon (a_μ) [23, 34]. The A' boson can actually reconcile the 3.6σ discrepancy with the measured value of a_μ in the "a_μ Preferred" region.. The orange shaded regions correspond to bound from previous beam dump experiments, E774 at Fermilab [30] and E141 at SLAC [29], where the A' boson is sufficiently long-lived to yield a displaced vertex.

However, the muon anomalous magnetic moment results pick out the region $m_{A'}$ =10-100 MeV [23, 34], so DarkLight focusses on this region.

The goal of the present proposal is to study couplings in the range $10^{-9} < \alpha' < 10^{-6}$, and masses in the range 10 MeV $< m_{A'} <$ 100 MeV. In this parameter range, the A' boson dominantly decays promptly as $A' \to e^+e^-$ with $c\tau > 10^{-2}$ cm. This parameter space is illustrated in Fig. 1, with the most important constraints indicated. We believe we can reach couplings in the range $\alpha' = 10^{-9} - 10^{-7}$ over the mass range 10–90 MeV with a 60 days (assuming accelerator 100% efficiency) of running at the JLab FEL, Fig. 2.

The DarkLight experiment has other physics goals that we have summarized in Appendix A. We believe we can also carry out these measurements, but have not considered them extensively in the development of the experiment so far.

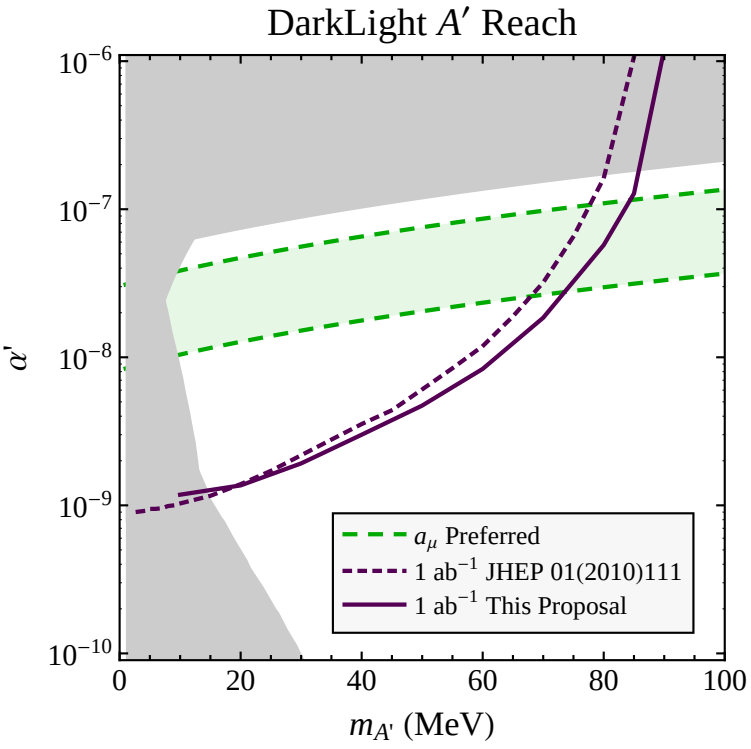

FIG. 2: The A' boson parameter space probed by DarkLight.

III. THE FREE ELECTRON LASER

As the only currently operating free-electron laser (FEL) based on a CW superconducting energy recovering linac (ERL), the Jefferson Laboratory FEL Upgrade remains unique as an FEL driver[37, 38], and, with minor modification, as the basis for the Darklight experiments. The present system represents the culmination of years of effort in the areas of SRF technology, ERL operation, lattice design, high power optics and DC photocathode gun technology. The layout of the JLab FEL Facility is shown in 3. There are two FELs, one operating in the infrared (IR), and one in the ultraviolet (UV). The machine as it stands delivers 7 micron emittance bunches of 135 pC at average currents up to 10 mA (74.85 MHz repetition rate). The present beam energy is 130 MeV although it has operated up to 160 MeV in the past. The system has lased in the 0.364 to 11 micron region and produced up to 14.3 kW of average power at 1.6 microns. At lower powers it can tune rapidly over factors of 8 in wavelength. The stable performance of this machine over many years establishes a solid foundation for future light sources and other applications such as the experiment proposed in this report.

The ERL accelerator is comprised of a 9 MeV injector, a linac consisting of three Jefferson Lab cryomodules generating a total of 80 to 125 MeV of energy gain, and a recirculator. The latter provides beam transport to, and phase space conditioning of, the accelerated electron beam for the FELs and then returns and prepares the drive beam for energy recovery in the linac. The beam is typically accelerated (energy recovered) off crest (off trough) so as to impose a phase energy correlation on the longitudinal phase space used in subsequent transport to longitudinally match the beam to the required phase space at the wiggler (dump). That is to say, the bunch is kept relatively long during acceleration, compressed to high peak current and 100 fs rms pulse lengths just before the wiggler, then temporally expanded before reinsertion into the energy recovery phase of the linac. The recirculation transport is, however, operationally flexible and can accommodate configurations providing very small momentum spread to users - though at commensurately longer bunch length.

The electron beam can be sent through the IR wiggler beam path or through the UV wiggler. Switching between the operational modes is accomplished by shorting half the coils of the corner dipoles. The energy recovery transport consists of a second Bates-style end loop followed by a six-quad telescope. The beam is matched to the arc by the second telescope of the FEL insertion; the energy recovery telescope matches beam envelopes from the arc to the linac acceptance. During FEL operation, energy recovery occurs off-trough. The imposed phase-energy correlations are selected to generate energy compression during energy recovery, yielding a long, low momentum spread bunch at the dump. Calculations and measurements show that the emittance growth due to Coherent Synchrotron Radiation (CSR) is not a problem for lower charge but may impact operation at higher charge. As indicated above, this operating mode can be modified to provide small momentum spread and longer bunches; this will alleviate CSR-driven beam quality degradation.

For the proposed Darklight experiment, the machine will operate in either a different on-crest acceleration scheme or with a cross-phased tuning, so as to provide smaller momentum spread and longer bunch, instead of the nominal off-crest now used for FEL operation. It is desired that both beam-halo and emittance be eventually measured at the experimental location - the UV wiggler pit. However, an opportunity exists in the shorter term to validate the beam halo and emittance with relatively minor modifications in the 3F region on the IR line. This choice has the added advantage of performing initial halo studies in the most operationally flexible and heavily instrumented region of the system.

A. FEL Beam Test Plans

The FEL has gained extensive experience and has in place the necessary beam controls to deal with halo along the beam line. A simple halo monitor will be integrated into the DarkLight experiment target chamber for observation of the beam halo at low duty-cycle for the test in summer of 2012. However, it may be necessary to remove the halo-monitor from its legacy position downstream of the second recirculation arc and reinstall it in a cross near 3F06 region on the IR line. In regard to the relevance of halo measurements at the IR beamline as opposed to on the UV beamline, it has been pointed out that although this location is not where the DarkLight experiment is eventually intended to take place, the measurement will provide valuable experience and data needed for a preliminary beam analysis, uncover potential effects that may be seen in the final location, and thus inform the design of the beam line to the DarkLight detector in the UV section of the ERL accelerator.

For the final configuration of the DarkLight experiment, it will be desirable to minimize the emittance of the electron beam by running the accelerator at low charge (10∼20pC), and high repetition rate (748.5MHz). In order to run the machine this way for the Darklight experiment, certain modifications and additions to the electron photocathode gun drive laser and to the injector tuning are needed, which will be detailed in the following discussion.

The goal of this investigation is to simulate some of the most challenging aspects of high-power ERL operation with an internal gas target, with particular emphasis on control of power deposition from beam loss and impedance/wake effects from both beam core and halo components during transport through a short (10 cm long) small aperture (6, 4, or 2 mm diameter) test aperture. To this end, the ERL operational configuration and beam transport system must meet certain requirements.

1. The beam momentum spread should be small to provide a narrow source energy spectrum.

2. Bunch length should be long so as to avoid resistive wall and other wake effects

3. The core transverse beam size should be small; in particular, it should be betatron-matched to the aperture constraint (nominally, a waist with $\beta_x = \beta_y = L_{aperture}/2$ at the center of the aperture)

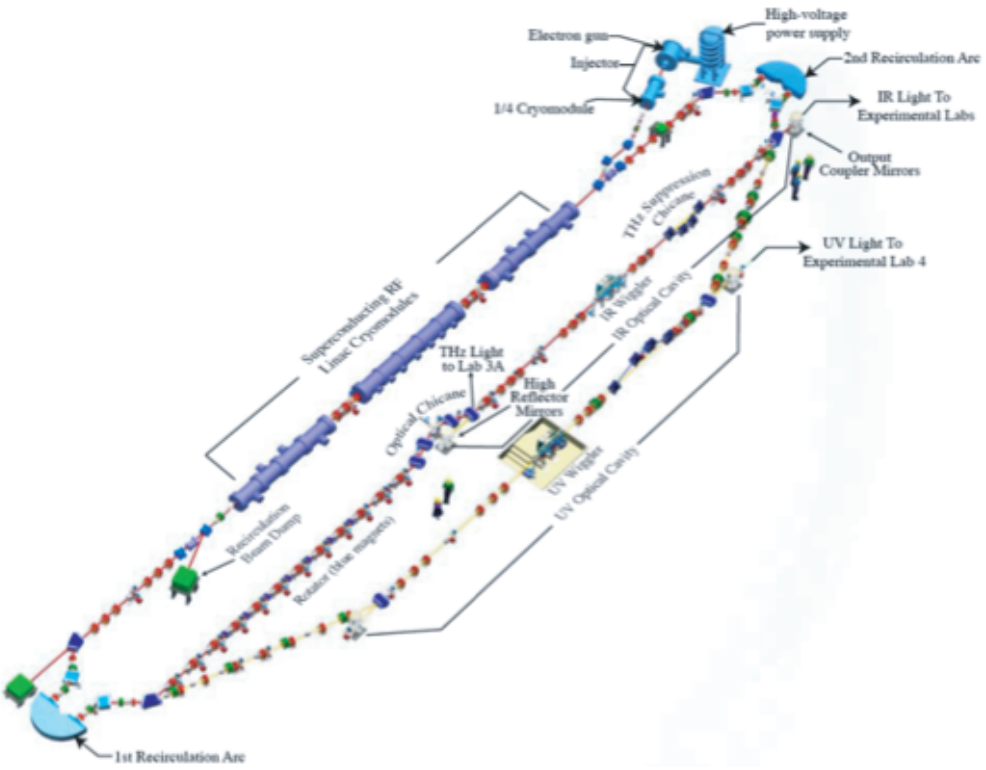

FIG. 3: Schematic of the existing JLab light source facility.

4. In order to control beam halo (independently of core beam), betatron phase advance should be independently variable in both transverse planes over at least a half-betatron wavelength. This will allow control of halo envelopes at the aperture while constraining the core beam betatron match.

5. The test should simulate an implementation of a fixed-target-based detector system; it should thus simulate focusing onto an internal gas target embedded within a detector system by providing a stand-off distance of order 1 m to and from the aperture constraint.

These requirements can be met using the existing JLab IR Upgrade beam transport system with only minor modifications. Requirements 1 and 2 are constraints on the longitudinal match. These are readily satisfied by operation either on crest/in trough or cross-phased, a linac phase set-point in which FL03 (the center cryomodule) is set to operate on the opposite side of crest from FL02/4 (the first/last cryomodules). Either configuration will result in a small momentum spread and long bunch through the recirculator; both are most readily implemented by tuning the recirculator to be isochronous. This is readily done, given the

IR Upgrades demonstrated operational flexibility in longitudinal matching.

Requirements 3-5 are readily met in the so-called 3F region of the present IR Upgrade transport system (see Fig.5 in Section C for a illustration of the ERL accelerator), provided minor modifications are implemented. If the test apertures are placed at the symmetry point of the region (now occupied by MQX3F06S), there will be available a set of no fewer than eight quadrupoles both upstream and downstream of the test aperture: MQX3F01, 2, 3, 3S, 4, 4S, 5, 5S, and 6 upstream, and MQX3F07, 7S, 8, 8S, 9, 9S, 10, 11, and 12 downstream. Assuming 5S and 7S are rotated into normal quads (these changes constitute the aforementioned minor modifications; 3S and 9S are already in the normal configuration), the resulting installation has the following features.

First, it mimics a typical collider/detector interaction region, with appropriate stand-off distance of the final focus quads from the interaction region (in this case, the aperture/adjacent quad separation is 3/4 m, about the 1 m notionally required for the full implementation). Secondly given the availability of eight quadrupole families both upstream and downstream, a betatron match to and from the test apertures can be executed with phase advance control into and out of the test assembly. This allows both independent control of the halo envelopes at the test aperture (needed to insure halo transmission) and turn-to-turn control of betatron phase advance (by adjusting the 3F07-onward match downstream of the test aperture) while providing fixed downstream beam envelopes (needed for control of the beam break up instability while controlling core beam betatron matching through the wiggler insertion and energy recovery transport). Finally, it moves the final focus elements in close enough to the test aperture to allow matching to the geometric acceptance of the test aperture while keeping the beam and halo within the geometric acceptance of the surrounding transport system.

In this regard, we note that the acceptance match for the test aperture in its most constrained configuration is defined by the length of the aperture, viz., 10 cm. Thus, the optimal match will be a waist at the center of the optimal with $\beta_x = \beta_y$=0.05 m. At the ends of the aperture, we thus have $\beta_x = \beta_y$=0.1 m. At 1 m up- and downstream of the aperture midpoint, this will result in $\beta_x = \beta_y$=20 m, with a peak envelope in the adjacent quad triplets of order 50-100 m. Given the minimum 1 mm radial aperture, the geometric acceptance will be 0.001m/20m, or 5 mm-mrad. This is 100 times the nominal beam emittance of 0.05 mm-mrad (10 mm-mrad at 100 MeV). Assuming an upstream/downstream match with beam

envelopes under 100 m, the acceptance of the up/down-stream transport with its 0.0375 m radial aperture (3 full bore) is at least 0.0375 m/100 m, or 37.5 mm-mrad, well above that constrained by the smallest test aperture.

In conclusion, minor modifications (as described above and detailed below) of the existing JLab IR Upgrade 3F region will allow flexible, independent, and robust control of core and halo components of the beam at a properly located test aperture. This will provide a high-fidelity analogue simulation of the critical challenges associated with the operation of an internal gas target such as that needed for DarkLight.

Follow-on effort must address the impact of embedding the gas-jet target in a relatively strong (0.5 kG) solenoid. This will introduce significant coupling of the electron beam; this can be in principle addressed by appropriate provisions for coupling/decoupling the incoming/outgoing electron beam in the vicinity of the target and detector (as is done in all collider/internal target rings). In practice, we will address this issue when the detector design is complete and the specific implementation of the experiment in the UV Demo transport line is more completely defined.

B. Resistive-wall Heating Effect

The primary goal of the presently proposed DarkLight experiment is to thread a high current e-beam through several tubes in a metal block with diameters ranging from 2 mm to 6 mm. Beam energy loss onto the target wall may be detrimental to the DarkLight experiment. There are two sources that may lead to the beam loss, one is the low intensity beam-halo and the other is the parasitic energy loss due to the resistive-wall impedance. The interaction of beam-halo with the beam tube generates background radiation and heating on the target wall. A high contrast measurement of the beam profile is needed in order to reveal details of the beam-halo. The resistive-wall effect, on the other hand, can be estimated based on the previous studies and resources. Due to the resistive-wall impedance, the wakefield generated by short electron bunches in the beam tube induces parasitic loss, leading to resistive-wall heating effect. Knowing how severe the heating effect would possibly be is important to the experiment and very helpful to the target design.

The parasitic energy loss due to the resistive-wall impedance of beam pipe has been studied and reported in many literatures [39–42]. There are a few useful simulation codes

[9] developed to calculate the effects associated with Wakefields. Analytical expressions for both longitudinal and transverse resistive-wall impedances for round pipes are also available. It has been shown that parasitic loss induced by the longitudinal impedance in a high current ERL accelerator, due to its much shorter electron bunch length, appears to be a more serious issue than other synchrotron light source. Following the equations by Nakamura [43] and the parameters for JLab ERL machine, we calculated the loss factor and parasitic power loss for the three different tubes designed for the DarkLight test. The result is shown in Fig. 4 and 5.

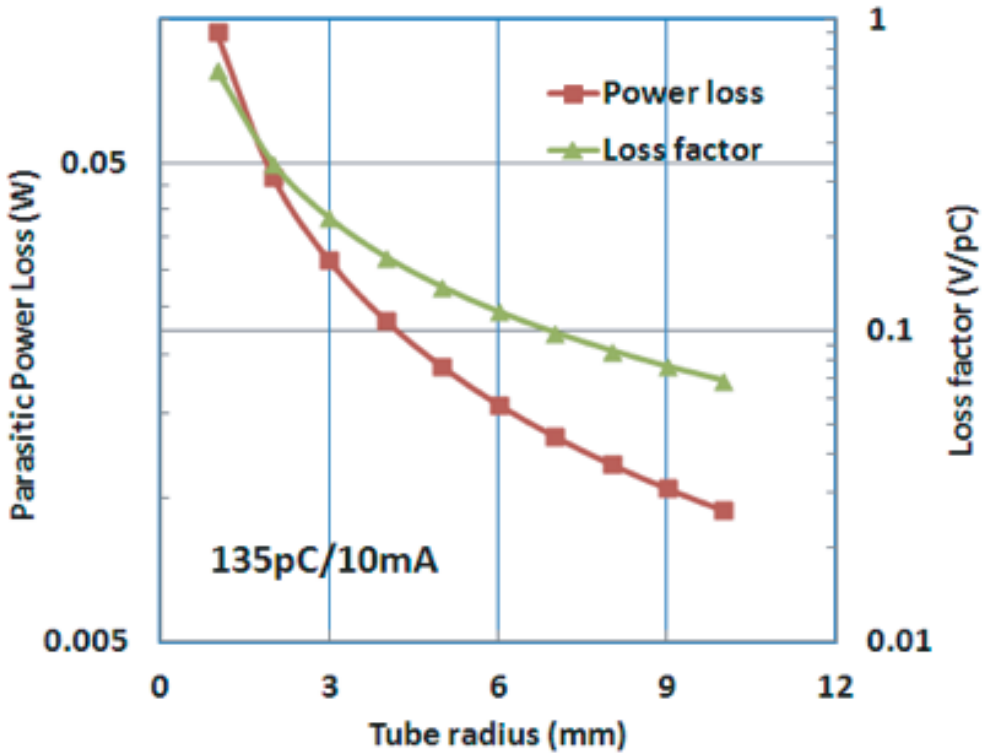

FIG. 4: Calculation results of loss factor and resistive power loss versus tube radius. Aluminum pipe: 100mm long, Conductivity: 3.56e7(1/m), RMS e-bunch length: 1mm (3.3ps), E-Bunch: 135pC/75MHz (average current 10mA)

Gaussian distribution is assumed for the electron bunch in all calculations for Fig. 4 and 5. The DarkLight test machine configuration is significantly different from that of an nominal FEL configuration (bunch length about 100 300fs RMS), the expected electron bunch length will be much longer (a few ps). In Figure B-1, 1 mm (or 3.3ps) bunch length is used in the calculation. We can see the power loss is only on the order of mW even

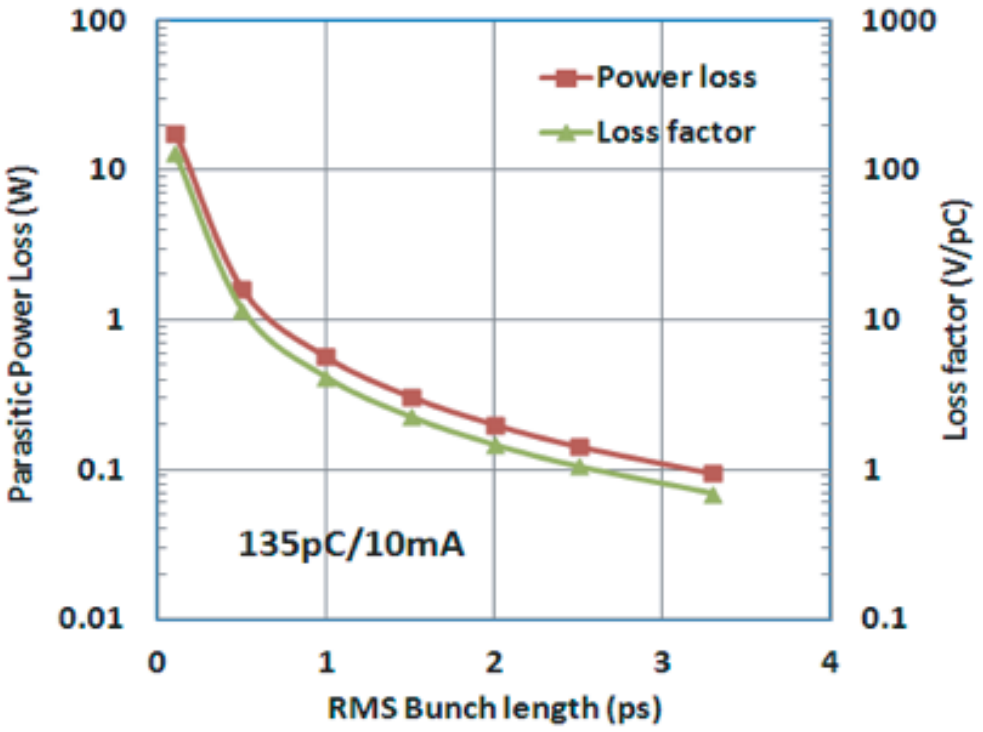

FIG. 5: Calculation results of loss factor and resistive power loss versus electron bunch length. Aluminum pipe: 2mm in diameter, 100mm long, Conductivity: 3.56e7(1/m), E-Bunch: 135pC/75MHz (average current of 10 mA).

for the smallest tube diameter (2mm). But the situation appears to be rather different in case of a very short bunch. As shown in Figure 5, the power loss is close to 20W for 100fs bunches and a 2mm diameter tube. To draw a conclusion, the resistive-wall loss does not appear to be a concern in case of the DarkLight experiment for which the accelerator runs longer electron bunches. The loss will be further reduced by a factor of 10 when we operate the machine under the low charge and high repetition rate mode.

C. FEL Machine Modification

The test to be performed at JLab FEL facility in 2012 is the first step of the whole DarkLight experiment and consists of two parts:

1. High current electron beam threading experiment: the goal is to demonstrate that JLab FEL high current electron beam can be cleanly and stably threaded through a target assembly consisting of three 100mm long tubes with different diameters (2

mm, 4 mm and 6 mm). A section of the FEL IR beam line (3F) has been identified as the place to install the target assembly and the hardware for the designed beam configuration to achieve small beam emittance and size. A schematic of the target chamber structure is shown in Fig. 6.

2. Radiation background measurement: in order to design the detector, it is necessary to understand the background from the electron beam and FEL machine. Knowledge of the radiation background is necessary to ensure the DarkLight's tracking detectors are able to operate successfully in the FEL vault. The background measurement will be performed concurrently with the beam-threading experiment to study the beam scattering effect by the tube walls and to verify it does not constitute an important source of background for the DarkLight detector. A large part of this experiment can take advantage of beam operations for other scheduled FEL programs. The detectors, electronics and other peripheral equipment are available and will be provided by MIT, W & M, and JLab.

Based on the beam configuration design described in Section B, the designated experiment location is the 3F region on the FEL IR beamline as shown in Fig. 7. This beamline installation is preferred in view of the very tight budget and machine schedule. The main advantages are that it has nearly all the needed diagnostics already in place, and it will have larger and more robust focusing dynamic range. This is important for varying the phase advance to control halo and for beam break up (BBU) suppression, as the rotator will be eliminated. The disadvantage is the relative short 1.5m space available for the target assembly.

As we know, any change of experimental location will always require a specific machine setup in order to be able to tightly focus the beam so it can pass cleanly through the small tubes. In this experiment the tubes are 2 mm, 4 mm, 6 mm in diameter and 100 mm long. The machine configuration must also provide enough room for the target chamber and the necessary beam diagnostics. The estimated beam β function is quite small ($\sim$50 mm) for this configuration at this location. Three beam viewers are needed for beam size and emittance measurement, one upstream, one downstream and one in the center of the beam-tube assembly. The viewers are expected to be as close to the chamber center as possible. It should be mentioned the nominal beam energy for the DarkLight experiment is 100 MeV,

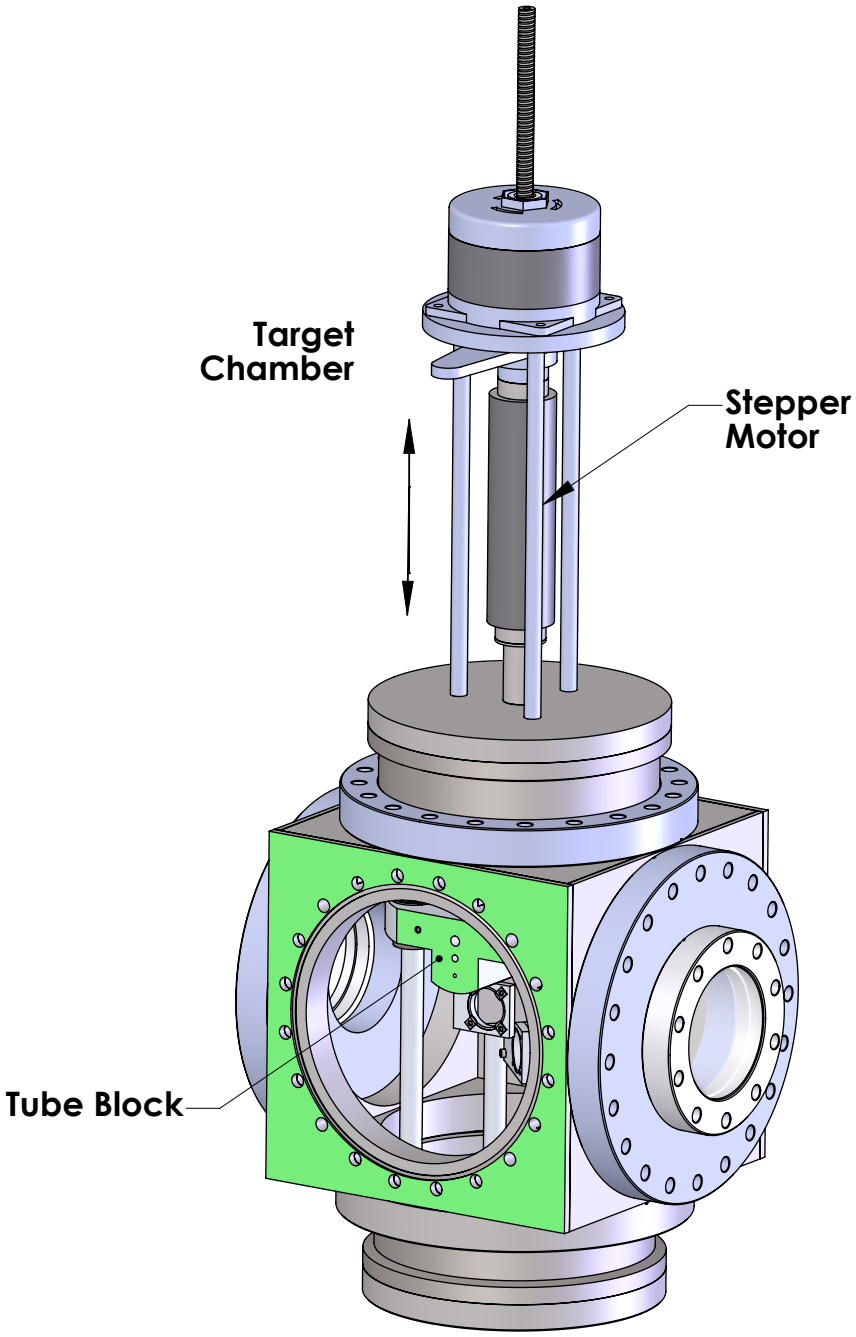

FIG. 6: Schematic of the 6 cross target chamber. Three beam tubes are also shown inside the chamber. The tube block is driven by a stepper motor to move in and out of the e-beam.

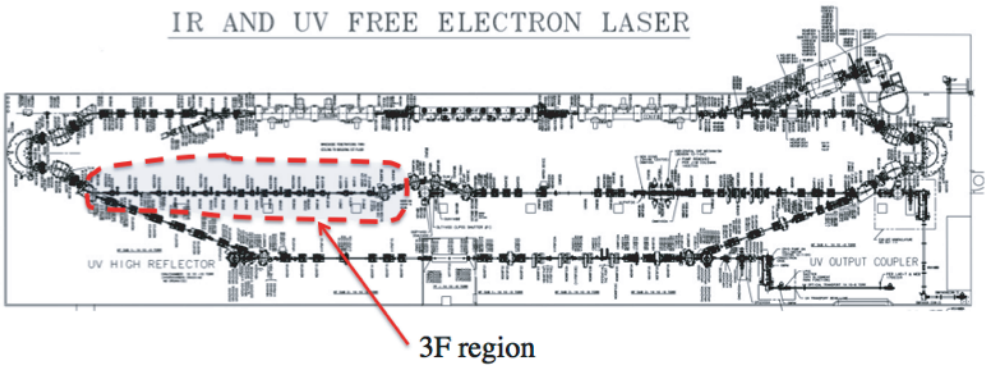

FIG. 7: JLab FEL Facility and the location (3F) for the intended DarkLight experiment.

which is quite different from the routine operational beam energy of 130MeV. In addition, as will be discussed later in Section E, a low energy, low charge, and high repetition rate beam mode is highly desirable, therefore a considerable amount of time will be necessary for machine tune-up.

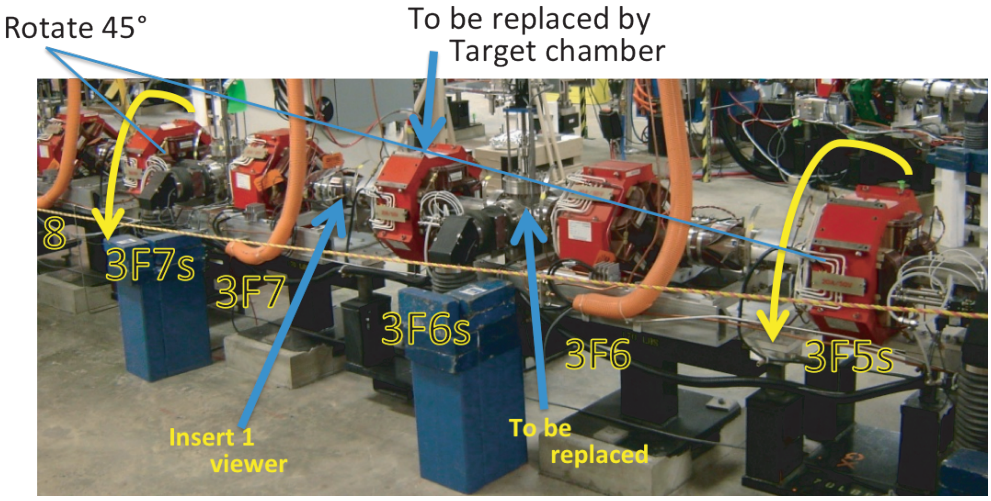

FIG. 8: A picture of the components on the beamline at 3F region. Each red quadrupole magnet is marked with its component number.

Fig. 8 is a picture of the beam components on one section of the beamline in the 3F region. This is where the DarkLight target chamber will be installed. Specifically, the machine modification includes:

1. Rotate two magnets 3F5S and 3F7S by 45 to a normal quad configuration. This is a fairly straightforward work and can be implemented by FEL technical staff. However,

the girders beneath these two magnets have to be lowered by approximately 1 inch after the rotation in order to center the magnets to the e-beam axis. We have carefully measured the stands and decided that the existing mechanical mechanisms can provide the adjustment without adding any extra hardware.

2. Replace one magnet (3F6S) with the target chamber.

3. Modify the viewer between 3F6 and 3F6s. The existing viewer has a thin aluminum foil as OTR material and will be replaced with a silicon wafer for better performance.

4. Add one standard silicon-type beam viewer between 3F6S and 3F7.

5. Install 2nd corrector on girders 3F6 and 3F7.

6. Align all the components to required precision.

7. Install one beam viewer on each side of the chamber for beam size and halo measurements.

8. Design and install control software to move the small tubes in the chamber.

9. Install detectors and their shielding for radiation background measurements.

Fig. 10 presents an illustration of the beamline after the target chamber and a new viewer are installed. The chamber and two viewers are mounted on the same girder and stand as one unit. The existing girder will be replaced by a shorter one in order to fit the whole unit into the beamline. Fig. 8 shows a top-view of the same assembly as in Fig. 9, with two more additional optical systems installed on the sides of the target chamber. More details will be given in Section D, the idea is to attach a silicon wafer and a YAG crystal under the tube block for both beam size and halo measurement. The tubes, wafer, and the YAG are aligned at different vertical position so that each of them can be moved into the e-beam by the stepper-motor at a time as needed. The silicon wafer is mounted at 45 to the beam axis to kick out the OTR light to one side window while a 45 mirror at the back of the YAG crystal reflects florescent light out of the chamber through another side window. The cameras and optics in these two systems are different. One of them is the same as other standard viewer systems and will be used with the YAG scintillator inside the chamber,

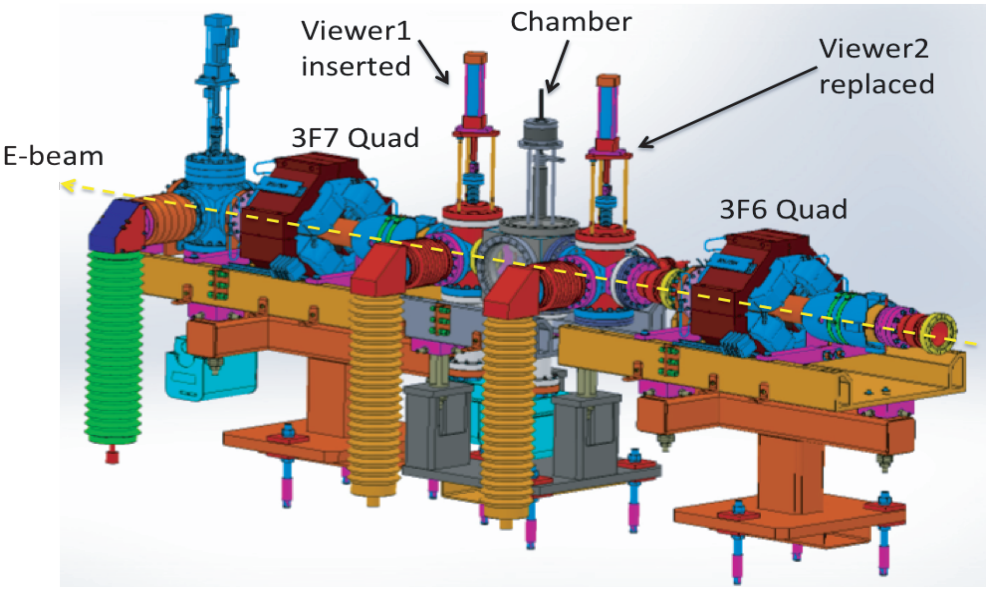

FIG. 9: Drawing illustrating the assembly with two beam-viewer systems and the target chamber installed. The optical imaging system for the chamber viewer and halo monitor are not shown.

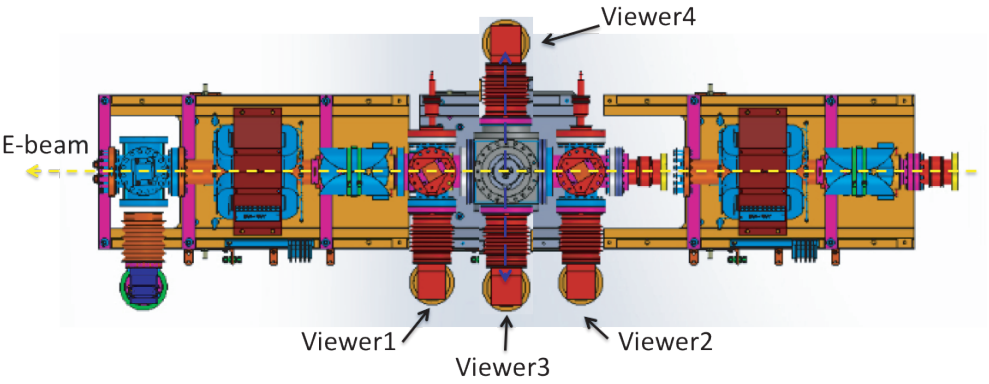

FIG. 10: A top-view for the same system shown in Fig. 9 with one optical system installed on each side of the target chamber. Viewers 1, 2, and 3 are silicon wafer beam viewers. Viewer 3 is for halo measurement using YAG.

the other one is designed for measuring the small beam focus with high magnification and resolution.

After the installation of the all the components, a high precision alignment will be performed. The chamber and the beam block will be first aligned and fudicialized in a lab at MIT before delivery to JLab FEL for integration with viewers and girders. The chamber assembly and all the magnets can be aligned within 50∼100 μm to the beam axis by JLab

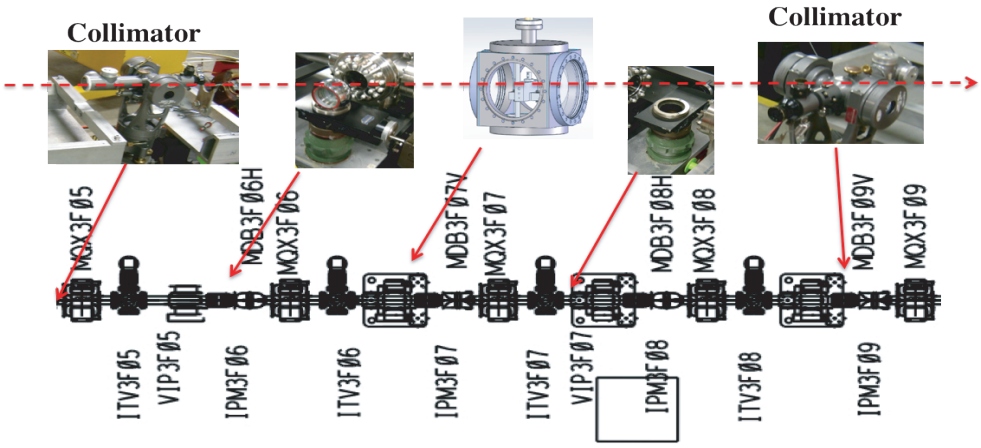

FIG. 11: Layout showing the alignment method and the position for each of the tools and instruments on the 3F beamline.

Survey group with conventional alignment procedures by using laser tracker and collimation telescopes. As shown in Fig. 11, the beam tube inside the chamber can be collimated with one collimation scope upstream and one downstream of the target chamber. This process has to be executed under air and can not be possible once the component is under vacuum. It is helpful if a laser beam can be used to check and align the beam tubes during the operation when the viewers can register the e-beam positions before and after the target chamber.

A laser alignment schematic is shown in Fig. 12, taking advantage of an existing setup established for other application. The laser is a He-Ne laser tube with a beam size of 0.5mm at 633nm wavelength. To see if the laser beam size is small and clean enough around the target area, a diffractive propagation simulation was carried out and the result is given in Fig. 13. It is clear that the laser beam size is about 0.2mm (1/e2 Gaussian beam) with a 30cm range in the target center area. This is good enough in view of the much larger beam tube (2 mm minimum) and the short distance between the beam viewers upstream and downstream of the chamber. The two steering mirrors (M1, M2) will be controlled remotely for online adjustment with the help of beam viewers during machine operation.

There will be no significant modification of the control and electrical hardware work expected for the current DarkLight test period which ends before August 1, 2012 when a lab-wide shutdown will be in effect. The target chamber assembly will go though a bench test to check the electronics and control. The final EPICS control software for the target motor

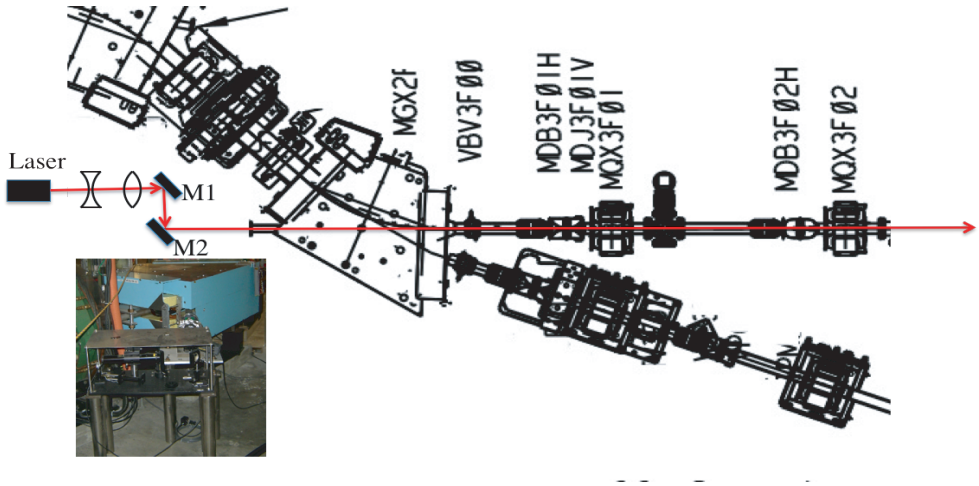

FIG. 12: Layout showing the alignment method and the position for each of the tools and instruments on the 3F beamline.

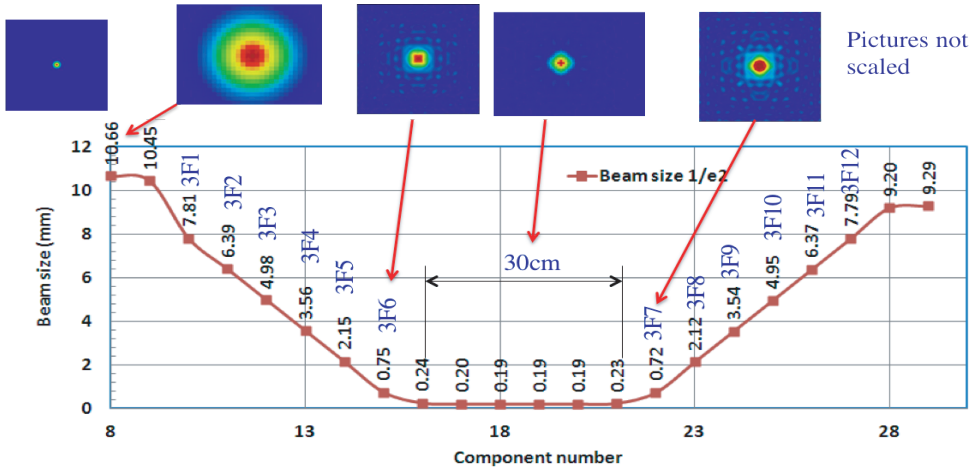

FIG. 13: Simulation result of laser propagation along the 3F beamline. The horizontal axis stands for component numbers. The area around component 18 (the target chamber) is expanded for a better view of the focus area. The magnet names (in blue) are also shown.

and viewers will be designed in advance and then installed and tested after the installation of all the beam components into the beamline.

D. Beam Diagnostics and Characterization

As mentioned in previous sections, it is necessary to perform beam characterizations in order to know the important experimental parameters such as the transverse beam emittance

and the beam size, in particular, the beam halo, for the proposed DarkLight experiment. The beam emittance along the target area can be measured by using three beam viewers (viewers 1, 2 and 3 in Fig. 10) to be installed upstream, downstream, and in the center, of the target chamber. Such measurement is a standard beam emittance measurement technique. The idea here is that, with the beam size measurements at three different locations in the drift space containing the beam waist, emittance and Twiss parameters can be measured without changing the beam optics. This in principle will speed up the setup of the transverse match. The transverse beam size in the target area depends on the transverse emittance. Operation of the injector and recirculator with the bunch charge intended for the DarkLight is a non-standard FEL machine operation mode. One of the objectives of the test is to measure the emittance and the smallest achievable beam size. The three viewers aforementioned will be the Optical Transition Radiation (OTR) viewers which are routinely used at the FEL for transverse beam profile measurements. Assuming the normalized transverse emittance of the beam is about 10 mm-mrad, the smallest beam size in the middle of the target chamber is expected to be 50 μm RMS. The transverse beam size scales as the square root of the emittance. The spatial resolution of the standard OTR setup at the JLab FEL is about 15 μm. Therefore, the optical imaging system of the OTR viewers need to be upgraded in order to achieve a much better resolution of about 5 μm. A convolution of the beam profile measurement with such a fine resolution (point spread function) will allow to detect changes in beam size that is significantly smaller than the projected 50 μm. In case this three-viewer measurement method fails to provide the expected resolution, more accurate measurements of beam emittance and Twiss parameters can be performed by quadrupole scan using one of the OTR viewers with improved resolution. To achieve a better imaging resolution and keep the field of view reasonably large, the pixel numbers of the required video cameras will be increased by a factor of 4 compared with those standard cameras presently used at FEL while our in-house 10-bit frame grabbers can still be used. The frame grabbers are capable of working with non-standard video signals and images containing large number of pixels.

The 3F region of the driver ERL is heavily instrumented and has been extensively used for beam characterization of this type. In addition to numerous beam viewers (useful for quadrupole scans as well as the more frequently used multi-monitor emittance measurements), there is a halo-management octupole at the entrance to the transport line. This can be employed to test the sensitivity of transmission through the test apertures to manipula-

tion of large amplitude beam components, without changes to the core. Since the DarkLight experiment must carefully control the behavior of beam halo (estimated a factor of as much as 10^5 lower than the beam core near the target wall) at the location of the test aperture(s), a high contrast beam profile measurement is desirable. Although a method accommodating both high current (CW) and low duty cycle beam is preferable, during this run we will, because of schedule and budget constraints, restrict attention to tune-up beam only. This will dramatically reduce the cost and time without compromising our ability to get valuable information about the beam halo; future efforts will work toward implementation of a CW beam halo monitoring system such as the one demonstrated recently at JLab FEL that uses synchrotron light and an optical coronagraph. It is worth mentioning that one simple alternative to detect beam halo effect on the target is to use PMT-based beam monitors, the same way that the radiation background measurement for the DarkLight experiment is performed. However, this measurement is only indicative, not comprehensive to the understanding of beam halo characteristics, as the important details such as the specific halo distribution will not be revealed.

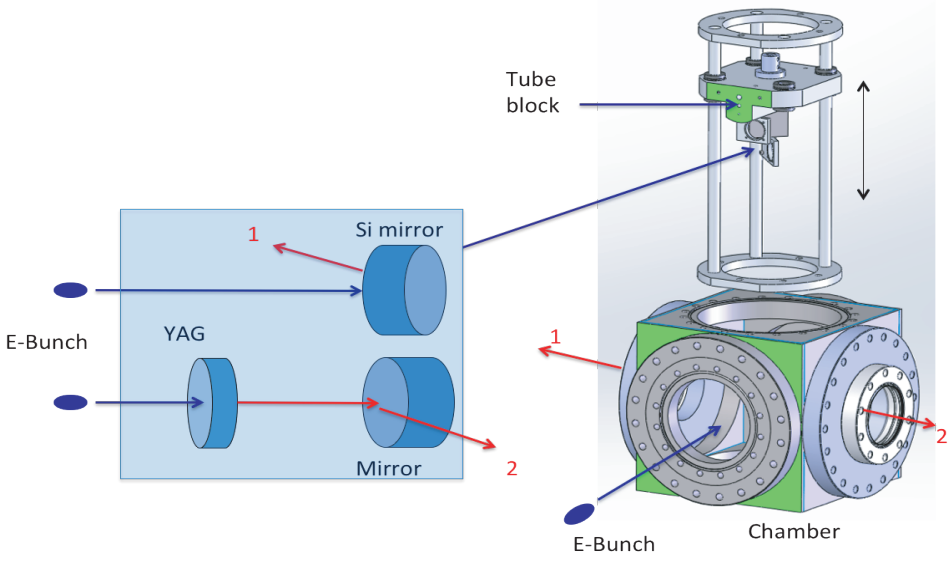

FIG. 14: Target chamber assembly with silicon wafer beam viewer and YAG crystal halo monitor attached together (drawing on the right). The left graph illustrates the basic idea about how the viewer and halo monitor operate. The flanges on top and the bottom of the chamber are not shown.

As for using low duty-cycle beam for the transverse beam profile measurements, a cost

effective way to get more detailed information about the transverse beam distribution with the large dynamic range is to employ a 100 μm thin yttrium aluminum garnet doped with Cerium (YAG:Ce) scintillator in the middle of the test chamber. YAG:Ce crystals are optically polished single crystal YAG:Ce scintillators. The key idea here is that with the same electron beam the amount of photons measured with the YAG viewer is about 100 times more than that measured with OTR viewers. This in principal should allow to extend the dynamic range on the low end by about two decades, compared to that with only OTR. Such beam viewers are already in use in the FEL injector. They also have been widely used in the beam diagnostic devices due to their high photon yield and excellent optical, mechanical and vacuum properties. The dynamic range of a conventional CCD camera is about 57 dB, only 3 dB smaller than a dynamic range of the 10-bit frame grabber. Thus the use of a YAG:Ce viewer should make the measurements about 100 times more sensitive, but will not extend the dynamic range by itself. To fully exploit the potentially high sensitivity of YAG:Ce crystals and to extend the dynamic range we will use a novel 2-CCD camera that is claimed to have reached a dynamic range near 120 dB. We have been evaluating the camera on the bench to gain initial experience. Work on the needed software to integrate the camera as a standard tool for FEL operation is also in progress.

Given the required resolution, the limited available space, and the physical size of the chamber, a chamber system has been designed that hosts both the beam tube block, a YAG crystal and a silicon wafer (as an viewer), as shown in Fig. 15. The concept for this assembly has been described in Section C.

E. High Repetition-rate Low Charge Mode

To keep the workload and cost at a minimum level, we will start the DarkLight experiment machine preparation with the current operation mode with a maximum 74.85 MHz repetition rate and perform important characterizations using various bunch charges including 13.5 pC, reduced by a factor of 10 from the nominal beam charge, as mentioned in previous beamline design section. This requires no modification on the present laser and pulse control system, but the maximum current will be limited to 1mA. There should be no essential difference in terms of the electron beam property at higher repetition rates. However, in order to do experiment at the full beam current (10mA) capability, it is deemed

necessary to reconfigure the machine for operation at high (748.5 MHz) repetition rate. Unlike FELs which put stringent requirement on both transverse and longitudinal emittance the DarkLight experiment only requires high average beam current and small transverse emittance; it places fewer constraints on the longitudinal phase space. This introduces the possibility to run accelerator at a much lower bunch charge and a higher pulse repetition rate, while keeping the machine at its equivalent maximum operation current level. A recent study [F. Hannons simulation] shows a much lower emittance may be achieved from the FEL injector with a low bunch charge (20pC), as shown in Fig. 13. This presents a significant improvement of the e-beam quality and brightness over the present beam which is about 7$\sim$8μm for 135pC bunch charge. The factor of ten emittance reduction means a much smaller beam size can be obtained. In principle, the injector beam brightness can be preserved as the beam is transported to the designated target area. It is very straightforward for the accelerator to run beam at any sub-harmonic frequency of its 1.497GHz driving RF frequency, the question is if we can reconfigure the FEL drive laser to run at a high repetition rate that meets the requirement. The FEL photo-cathode drive laser is a new laser system built on the state-of-the-art solid-state laser technology. Ever since it was commissioned, substantial reconfiguration and improvements have been made to keep up with the changing needs for machine operation and various R&D projects. This diode-pumped all-solid-state laser system consists of several sections [44], the oscillator which produces seed pulses, the multi-stage amplifiers, second-harmonic generator (SHG), the beam relay, and pulse control system.

The seed laser is a custom-built diode-pumped Nd:YVO4, passively mode-locked oscillator with 25 ps pulse width and over 500 mW output power at 1064 nm. This oscillator can be operated at two distinctively different repetition rates, one is 74.85 MHz (the 20th sub-harmonic of 1.497 GHz) and the other 748.5 MHz (2nd sub-harmonic of 1.497 GHz). The optical configuration has to be changed in order to switch to a different pulse repetition rate. The synchronization to the accelerator is achieved by phase-locking the laser to the RF drive signal. A phase loop actively adjusts the optical cavity length to minimize the pulse timing jitter. The rms timing jitter is usually about 0.5 ps. The amplification system contains four identical diode-pumped amplification modules. The first two amplifiers form a lower power channel (Channel 1) with over 20 W output. When all four amplifiers are running, the maximum power can reach 50 W (output Channel 2). After amplification, the

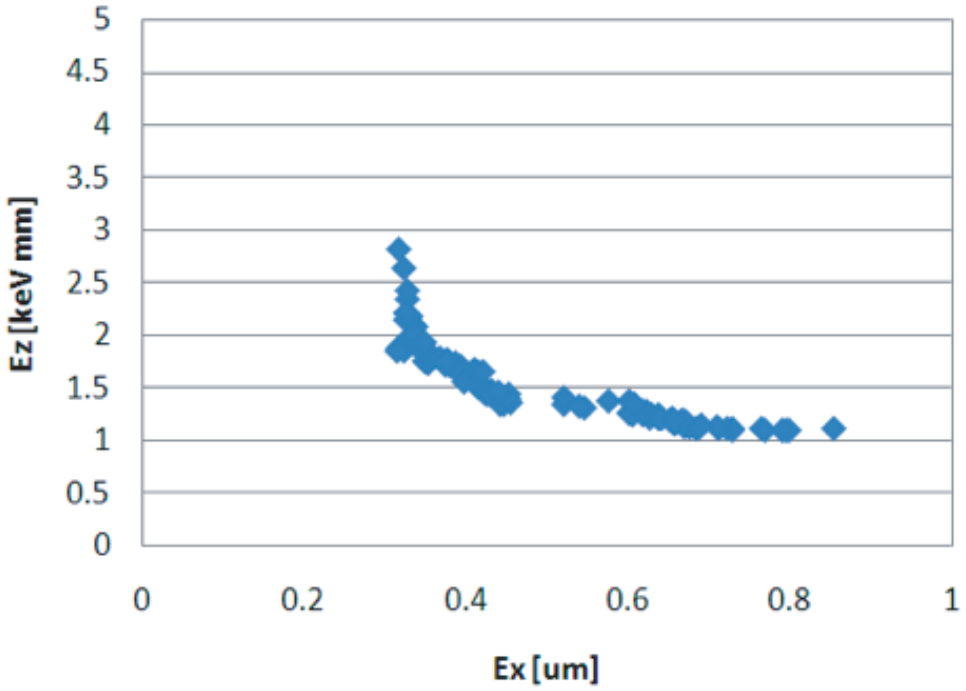

FIG. 15: Result of a beam emittance simulation for 20pC bunch charge from JLab FEL injector.

fundamental 1064 nm beam is frequency-doubled to 532 nm in a nonlinear crystal harmonic generator. At 74.85 MHz, the full laser power at 532 nm reaches 8 W from channel 1 and 25 W from channel 2. At 748.5MHz, about 13W was achieved due to lower SHG efficiency. With the existing FEL photocathode, about 4 W of average laser power at 532nm is needed to generate 10 mA electron beam current. Therefore the available laser power is sufficient if we run drive laser at 748.5 MHz and 10 20 pC bunch charge (the average beam current will be about 10 mA). However, some upgrades are necessary before the accelerator can operate under such a new beam mode. Specifically, we will need,

1. A new phase control system for 748.5 MHz laser oscillator. The key electronic components inside the phase-loop control chassis have to be replaced to accommodate the higher fundamental frequency. In addition, a new commercial phase-locking unit has to be purchased.

2. Upgrade of the drive laser pulse control system (DLPC) that currently only works at a maximum frequency of 74.85 MHz. The DLPC allows the accelerator to run at various beam-modes, in particular the tune-up mode at low duty-cycle routinely required during machine setup.

3. New electro-optic elements and drivers with much faster response.

4. Faster photo-detectors for pulse temporal pulse monitoring.

5. New laser pump diodes to replace the old ones in the laser.

All of these items are low risk. We have found that there may be a few lower charge pulses in a macropulse at either end of the macropulse but the fraction of beam in these pulses should be negligible. All the systems are commercial off-the-shelf or use an existing proven design.

F. Projected DarkLight Beam Test Schedule

The FEL machine has a busy running schedule in 2012 due to a lab-wide shutdown in August and relatively large number of experiments already planned to do. We were able to fit the DarkLight test into our crowded schedule, following are a tentative outline of time and work (subject to change depending on the progress of other experiments),

- 3/12 to 4/13
  Design and purchase Si wafer, YAG crystal, stepper motor and bellows (MIT)

- 4/4 to 5/16
  Mechanical design and Fabrication of target chamber (cube) girder and vacuum interface

- 4/16 to 5/7
  Procure mechanical parts to upgrade Viewer mounts (JLab)

- 4/16 to 5/18
  Fabricate target chamber Internals (including beam block, Si wafer and YAG crystal) (MIT) (JLab)

- 4/23 to 5/12
  Purchase optics and 3 High Resolution Cameras for beam viewers (JLab)

- 5/21 to 5/24
  Isolate, vent IR beamline and remove two viewers (ITV3F05, 06) (JLab) Rotate Quads (3F05S, 7S), and remove 3F06S Quad (at Target chamber position) (JLab)

- 4/23 to 5/11
  Repair the existing spare (3" dia.) beam viewer. Procure Si wafers for beam viewers (JLab)

- 5/22 to 5/28
  Install Si wafer on above beam viewers. Assemble Viewers & Align (JLab)

- 5/21 to 5/24
  Delivers target chamber to JLab (MIT). Bench test target chamber and control electronics (JLab, MIT)

- 5/25 to 5/31
  Check target chamber fiducials (JLab, MIT) Install target chamber and 2 beam viewers on Girder (JLab, MIT)

- 6/4 to 6/8
  Install final EPICS control S/W (JLab)

- 6/1 to 6/13
  Install target chamber and girder on 3F06S Stand (JLab) Install viewer, target chamber, cameras, and 2 pairs of correctors on girders 3F6 and 3F7. Install all power, LCW and signals (JLab)

- 6/14 to 6/20
  Test software, target chamber, electronics and beam viewers (JLab, MIT)

- 6/14 to 6/20
  Restore 3F beam pipe & Start Pumping (JLab) Pump Beam Line & Leak Check (JLab) Switch from UV to IR Beam Line (JLab)

- 6/19 to 6/21 High Precision align 6 Quads, Viewers, target chamber (JLab)

- 6/22 to 7/6 Setup machine and perform beam-based alignment (JLab)

- 7/9 to 7/13 Run Dark Light Beam Tests, Measure tube temperature & radiation (JLab, MIT)

IV. RADIATION MONITORS AND MEASUREMENT

To evaluate the radiation backgrounds in the FEL vault under typical running conditions, two types of measurements have been made. The first makes use of the existing RadCon Department's radiation monitors. The second uses two NaI/PMT detectors located adjacent to each other and positioned in the vault near the IR beamline, approximately adjacent to the end of the first full-length cryo module FL02.

A. RadCon monitors

Fig. 16 shows the locations of the detectors used in this study. Their data is available in the FEL stripchart system. A stripchart recording taken during sequential turn-on of the RF cryo modules is shown in Fig. 17. A substantial increase in the radiation level near the end of FL02 is seen by RM208-2 when FL02 is on. An increase at RM209-2, between FL03 and FL04, is seen when FL03 is on and a further increase when FL04 is on.

The monitor nearest the NaI/PMT detector location, RM208-3, shows a smaller but noticeable increase when FL02 is on, which predominates over contributions from the other cryomodules at this location.

B. NaI/PMT detector measurements

Two NaI/PMT detectors with their associated spectroscopy amplifiers, HV supplies, and cabling were positioned in the FEL vault near the IR line adjacent to the RM208-3 RadCon monitor. One is a College of William and Mary (W&M) unit, with a 3" NaI crystal, and the other an MIT unit with a 2" NaI crystal, Fig. 18. Readout of each is by two dedicated coaxial cables installed between the vault and Lab 1 upstairs. Each detector is read out by an MCA and computer in Lab 1. The detectors are at beam height from the floor and housed in lead brick enclosures, with a minimum thickness of 2 inches, Fig. 19.

Initially a 2" Pb shielding configuration was studied. This configuration was hermetic, with 2" of Pb on the top, bottom, sides, front, and back of the enclosure around each detector. A small gap between bricks was left open at the rear for cable access. Rates were observed to be significant, so two additional shielding configurations were studied. In the second configuration, an additional two inches of Pb on the front, top, and sides were placed

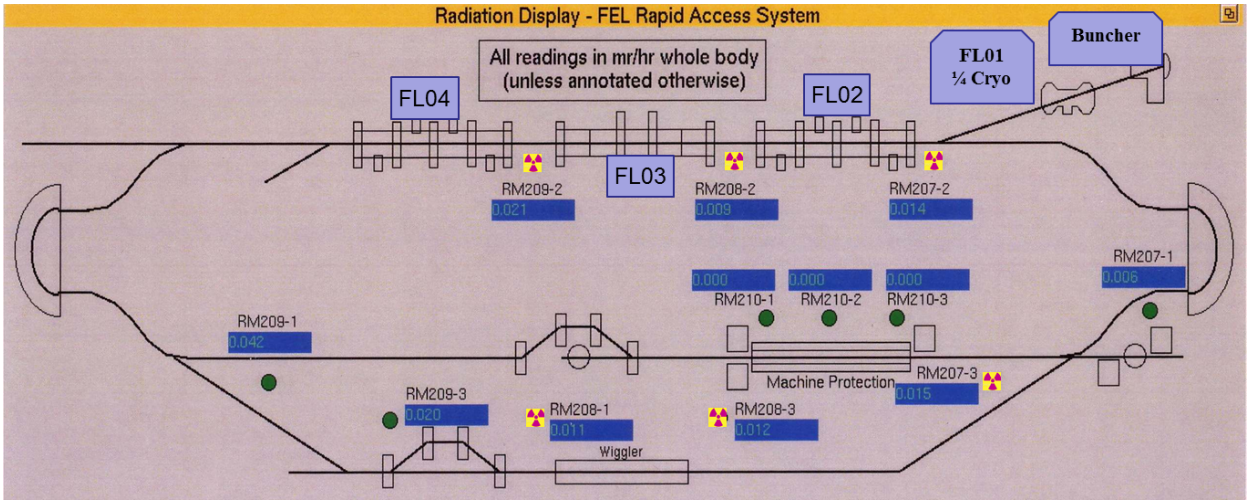

FIG. 16: Location of JLAB RadCon radiation monitors in the FEL vault. Locations are indicated by the trefoil symbols. Of particular interest are monitors RM207-2 (injection point), RM208-2 (between first two full-length cryo modules, FL02 and FL03), RM208-3 (between the IR and UV wigglers, adjacent to the NaI/PMT detectors), and RM209-2 (between the second and third full-length cryo modules, FL03 and FL04).

around the MIT NaI crystal, and in the third, another additional two inches of Pb were placed around the MIT NaI crysta, Fig. 20.

The detector setups were calibrated using ^{241}Am and ^{60}Co sources to cover an energy range from a few tens of keV up to about 2 MeV. Additional cross-checks were performed, including checking for noise sources. Tests were conducted with the PMTs HV turned off, while the RF was on. A number of data runs were taken under varying beam conditions.

Data were analyzed two slightly different ways. The first was a rough bin-by-bin summation from a selected region of each spectrum, without using an exact energy calibration, though the selected regions of the spectra were chosen to correspond approximately in energy, if not exactly. This was done (rather than just summing the entire spectrum) to avoid differences in pedestals at the low end of each spectrum between the MIT and W&M setups. Values of the integrated counts for each detector and their ratio are shown in Table I. From this table, it can be seen that the largest fraction of the observed backgrounds (70–75%) comes from having the RF on with no beam under all conditions studied.

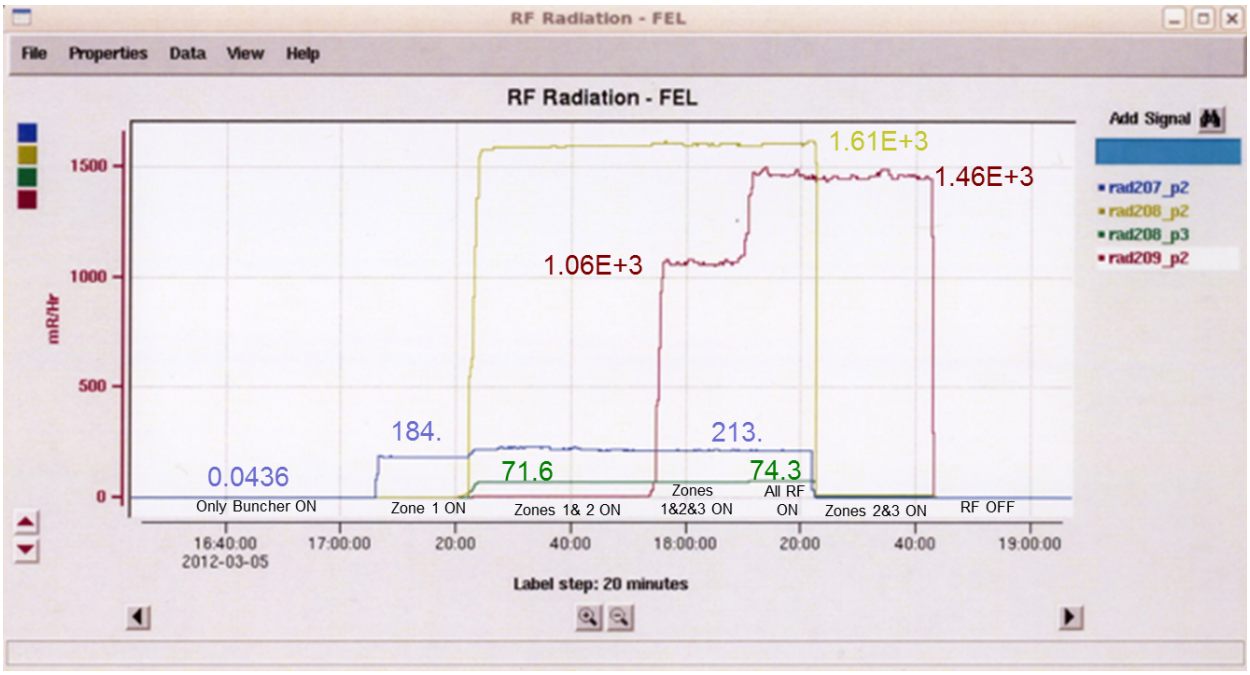

FIG. 17: Radiation levels in the FEL vault measured by selected RadCon monitors. Zones 1–4 refer to cryo modules FL01–FL04. Units are mR/hr, whole-body dose.

A second, and more precise, analysis was performed using spectra after the energy calibration had been applied. Two regions in each spectra were selected, the first from 0.5 to 1.0 MeV, and the second from 1.0 to 1.5 MeV. Counts in these regions were integrated. Results for the 0.5 to 1.5 MeV range are shown in Table II, and fits to the data points for both energy ranges in Fig. 22. It is clear that the shielding has an effect, yet the backgrounds seem to be very penetrating. Additional investigation to understand the backgrounds is needed, in particular to determine the relative contributions of photons and neutrons.

C. Summary of radiation measurements

In summary, the radiation measurements carried out to date in the FEL vault indicate the presence of a significant photon and/or neutron background in the range from a few keV up to a at least two MeV. Continued studies are underway. Goals are to determine the relative contributions of neutrons vs. photons and to study the effects of making the Pb shielding more hermetic, providing 4π coverage.

Run # range	Pb config.	Beam/RF	MIT ($\times 10^5$)	W&M ($\times 10^6$)	Ratio
002–003	4" shielding	0.6 mA	9.32	6.14	0.152
004–007	4" shielding	1 mA	9.17	6.51	0.141
008–010	4" shielding	RF only	7.04	4.97	0.142
011–013	6" shielding	0.6 mA	4.24	5.07	0.0836
014–017	6" shielding	1 mA	4.95	5.64	0.0878
018–020	6" shielding	RF only	3.56	4.23	0.0842
021–023	2" shielding	0.6 mA	24.1	5.54	0.435
024–026	2" shielding	1 mA	26.3	6.08	0.433
027–029	2" shielding	RF only	18.7	4.35	0.430
030	2" shielding	PMT HV off, 0.6 mA	0	0	N/A
033	2" shielding	PMT HV off, RF only	0	0	N/A

TABLE I: Running conditions investigated for the background measurements study. Data was taken on owl shift, April 24, 2012. Three runs were taken at each shielding/beam/RF combination and summed. The "MIT" column lists count integrals from approx 250 keV to 2 MeV spectra in the NaI/PMT setup whose shielding was varied. The "W&M" column lists integrated counts in the same energy range for the normalization detector (2 inches Pb). The last column is the ratio.

Pb (inches)	W&M counts	MIT counts	Ratio MIT/W&M
2	465848	139053	0.2985
4	552018	70893	0.1284
6	432012	26185	0.0606
8	—	—	0.02680
10	—	—	0.01207

TABLE II: After calibrating each detector system and converting channel numbers to energy in keV, counts in each spectrum were summed from 0.5 to 1.0 MeV and from 1.0 to 1.5 MeV. Results for the 0.5 to 1.0 MeV range are shown in columns two and three. Finally, the MIT numbers were normalized to the W&M numbers and are listed in the last column above. An exponential fit to the 2", 4", and 6" data was used to calculate expected rates for 8" and 10" Pb shielding.

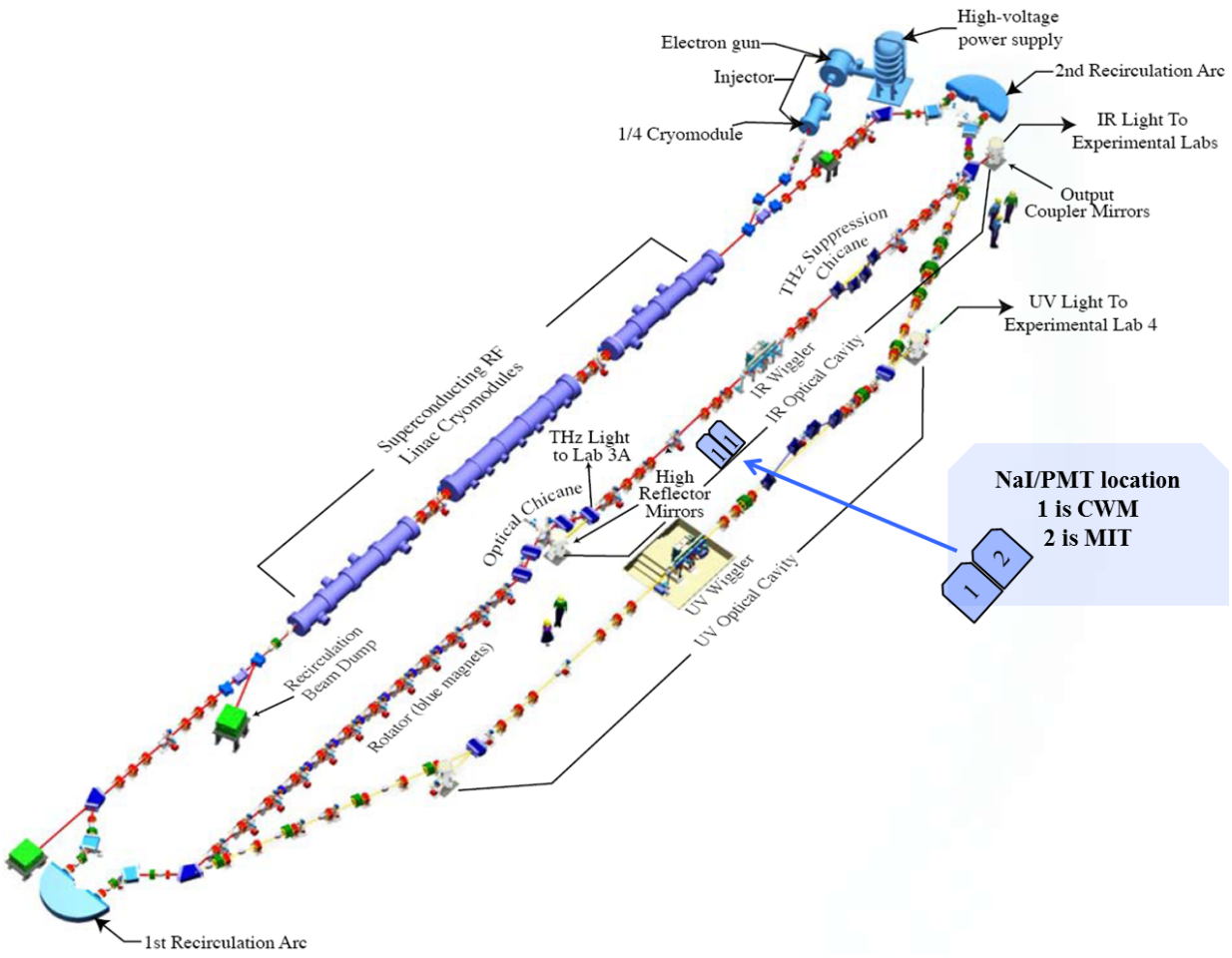

FIG. 18: Location of the two NaI/PMT detector setups near the IR line in the FEL vault.

It has been noted during these tests that beam-related backgrounds can vary by an order of magnitude or more under otherwise similar running conditions in terms of beam current, pulse rate, etc. (this is the reason for using one NaI/PMT detector for normalization). It may be that significant reduction of backgrounds is possible by careful choice of operating conditions by tuning of the beam, RF, and other beamline components during dedicated running for DarkLight. The bottom line, however, is that it appears that 8" of Pb may be required to reduce the photon background—assuming it is mostly photons—to acceptable background rates.

FIG. 19: Pb enclosures (blue) housing the two NaI/PMT detectors near the IR line. Cryo module FL02 is in the background.

V. EXPERIMENT DESIGN

In this section, the conceptual design of the DarkLight detector and target are described. The goal is to measure elastic electron proton scattering below pion threshold using the 100 MeV electron beam of the JLab FEL. With 10 mA of electron beam incident on a windowless gas target of thickness 10^{19} hydrogen atoms/cm^2, a data taking luminosity of 6×10^{35} cm^{-2} s^{-1} is attained. In 60 days of 100% efficient data taking, an integrated luminosity of 1 ab^{-1} is acquired. The experiment is designed to detect in coincidence with high efficiency the scattered electron, the recoil proton and the produced positron-electron

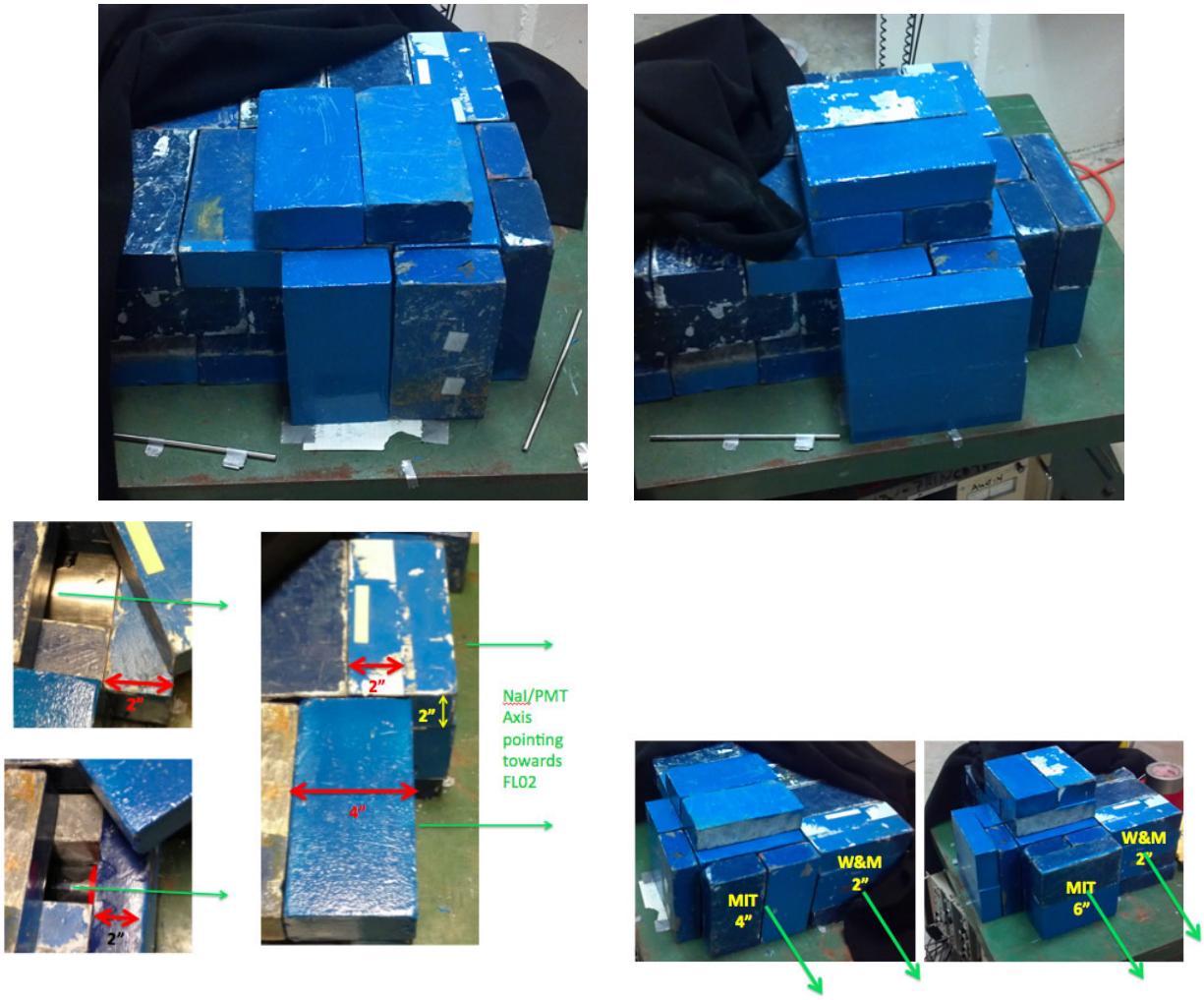

FIG. 20: Details of the 2", 4", and 6" Pb shielding configurations of the two NaI/PMT detectors. The MIT NaI/PMT detector shielding was varied over the three configurations: 2" all around, an additional 2" on top, sides, and front (the 4" configuration), and another additional 2" on top, sides, and front (the 6" configuration). The W&M NaI/PMT detector used for normalization was enclosed in 2" Pb shielding.

pair. The identification of all the final state particles allows the determination of the full event kinematics and efficient background rejection. The design of the DarkLight experiment is guided by the experience of members of the collaboration with the BLAST experiment at MIT-Bates [45, 46] and the OLYMPUS experiment now taking data at DESY [47].

Since the submission of the DarkLight proposal [48] in November 2010, the design of the experiment has been significantly revised. In particular, the high rate of Møller scattered

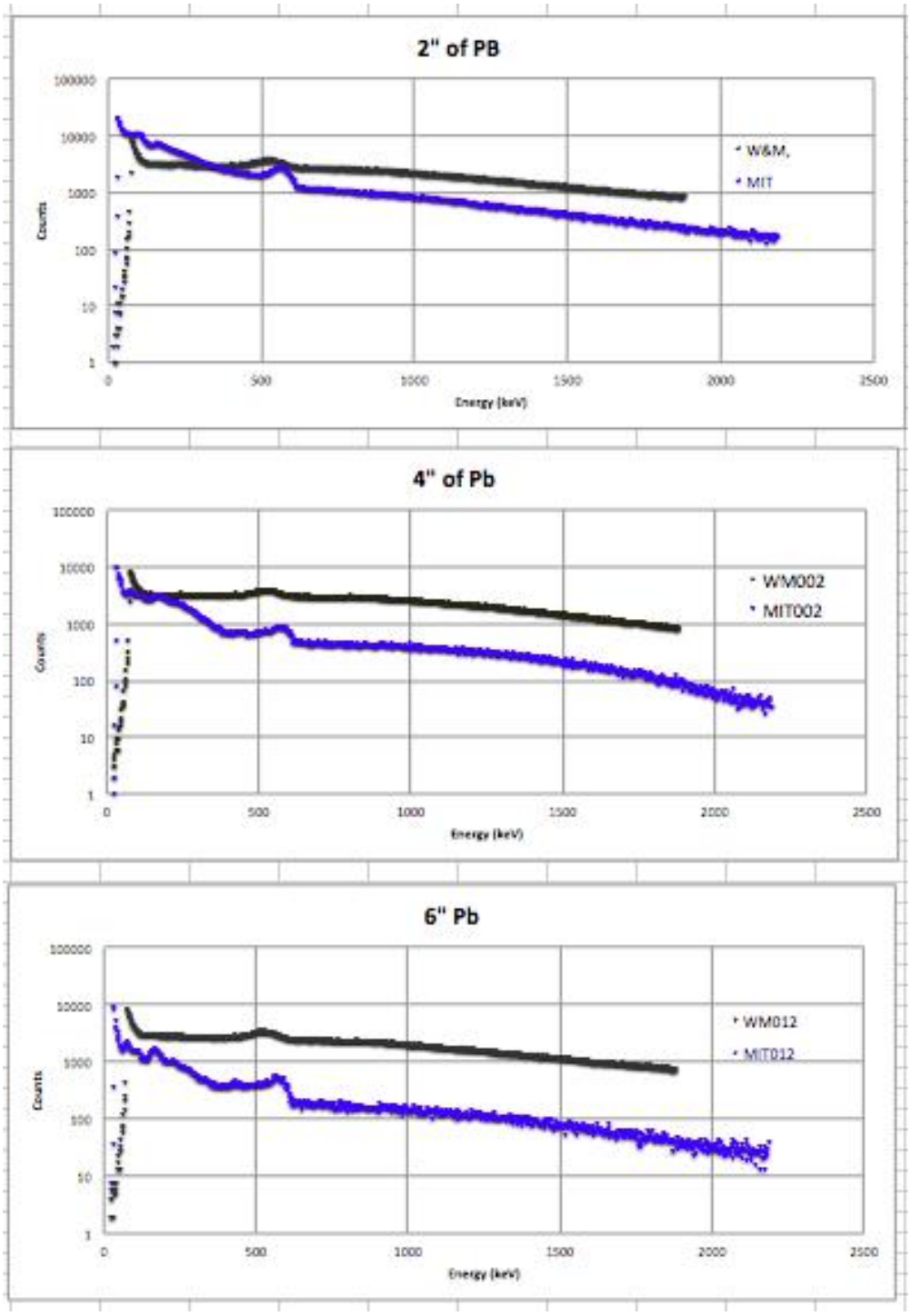

FIG. 21: FEL vault spectra as measured by MIT 2" NaI/PMT and W&M 3" NaI/PMT detectors for three different Pb shielding configurations surrounding the MIT detector. The W&M detector was shielded with 2" of Pb in all runs. Both detector systems were calibrated with ^{241}Am (59.54 keV) and ^{60}Co (1170 & 1330 keV) sources. All spectra were acquired in 60 second live-time runs. The pairs of spectra in each plot were taken simultaneously.

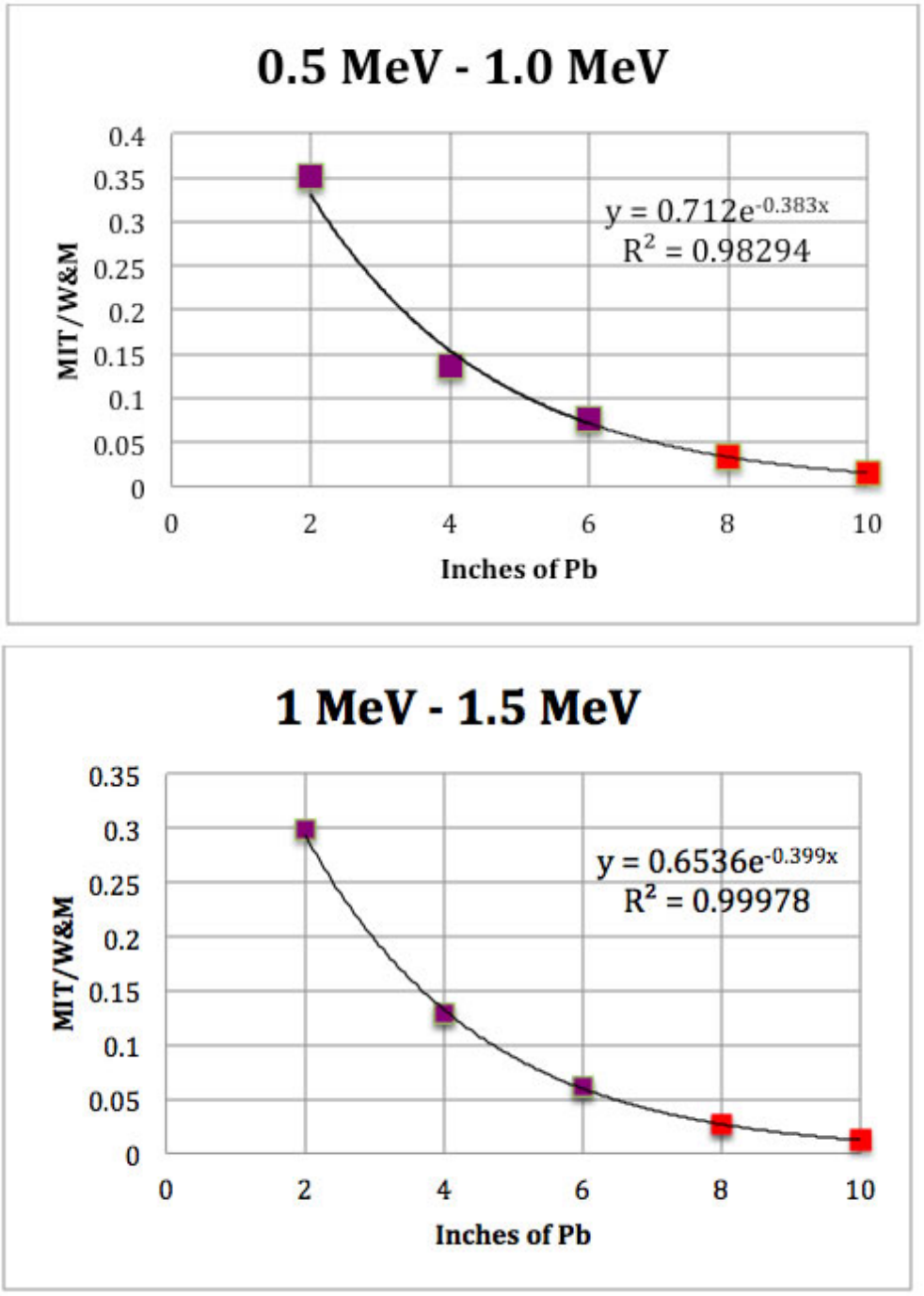

FIG. 22: Normalized counting rates (maroon points) in two energy ranges for the three Pb shielding configurations. Normalization was performed by taking the ratio of the MIT NaI/PMT spectra with the W&M NaI/PMT spectra. Curves are exponentials fitted to the three data points, and are extrapolated to 8 and 10 inches of Pb shielding (red points).

electrons in the forward direction demanded a longitudinal magnetic field of order 0.5 T to direct them out of the acceptance of the detector. Thus, the magnetic field used to track the final state leptons is now a solenoidal of magnitude 0.5 T. Shielding the lepton tracker from the large rate of associated radiative Møller photons requires a significant amount of shielding downstream of the target. The choice of technology for the lepton tracker is the GEM-TPC designed and built by a German collaboration [49]. An inner silicon detector will be used to detect the recoil proton from elastic scattering as well as provide tracking for the final state leptons.

A. Design considerations

TABLE III: Detector specifications for the DarkLight experiment.

Incident electron energy	100 MeV
A′ mass range	10 to 100 MeV
Scattered electron angle	25° to 165°
Final electron energy	5 to 100 MeV
Recoil proton kinetic energy	1 to 6 MeV
Recoil proton angle	6 to 163 degrees
Experimental A′ mass resolution	1 MeV
Total elastic rate within detector acceptance	10 MHz
QED trigger rate	1 kHz

1. Elastic scattering rate

Elastic scattering presents the major process and a significant source of background. The cross-section for elastic electron-proton scattering can be written as

$$\frac{d\sigma}{d\Omega} = \frac{4\alpha^2 E'^2 \cos^2\frac{\theta}{2}}{Q^4} \cdot \frac{E'}{E} \cdot \left[\frac{G_E^2 + \tau G_M^2}{1+\tau} + 2\tau G_M^2 \tan^2\frac{\theta}{2}\right] \tag{3}$$

where $\tau = \frac{Q^2}{4M^2}$ with M the proton mass; $G_E(Q^2) = [1 + Q^2/0.71\text{GeV}^2]^{-2} \approx 1$; $G_M(Q^2) = 1.79 \cdot [1 + Q^2/0.71\text{GeV}^2]^{-2} \approx 1.79$.

θ deg.	E' MeV	T_p MeV	Q^2 $(\mathrm{MeV/c})^2$	$\sin^2\theta/2$	θ_q deg.	rate MHz
15	99.6	0.4	677	0.017	82.5	148
30	98.6	1.4	2642	0.067	77	17
45	97.0	3.0	5665	0.146	66	5
90	90.4	9.6	18080	0.5	42	0.3
135	84.6	15.4	28899	0.854	21	0.2
155	83.1	16.9	31677	0.953	11	0.06

TABLE IV: Kinematics and rates for elastic electron-proton scattering in the DarkLight experiment. E' is the scattered electron energy, θ is the angle with respect to the electron beam direction and θ_q is the angle the recoil proton momentum vector makes with the beam axis.

The elastic electron-proton cross section has been calculated as a function of θ and the rate into bins of $\pm 2.5^\circ$ in θ and covering 2 π in azimuthal angle, i.e. $\Delta\Omega = 2\pi \sin\theta \Delta\theta$ determined. A luminosity of 6×10^{35} cm^{-2} s^{-1} has been assumed. The angle that the recoil proton makes with the incident electron beam θ_q is also calculated for each value of θ. The rates are summarized in Table IV.

2. Møller scattering rate

The Møller process, i.e. the scattering of beam electrons on target electrons, produces an enormous rate of scattered electrons which might overload the detectors. A calculation of the expected count rate for 1° wide detectors with 2π azimuthal coverage is shown in Fig 23.

As can be seen in Fig. 24, the momenta of electrons scattered at larger angles are very small and these electrons will not exit the target volume. At smaller angles, the electrons will be bent around the beam line by the solenoidal field so that they will not reach the detector elements.

The next leading electromagnetic process, i.e. internal radiation, gives rise to photons with a bremmstrahlung $\frac{dk}{k}$ spectrum with an angular distribution similar to Møller scattering. The total radiated Møller photon rate is estimated to be of order 0.5% of the Møller rate. These photons must not be allowed to interact with the lepton tracker.

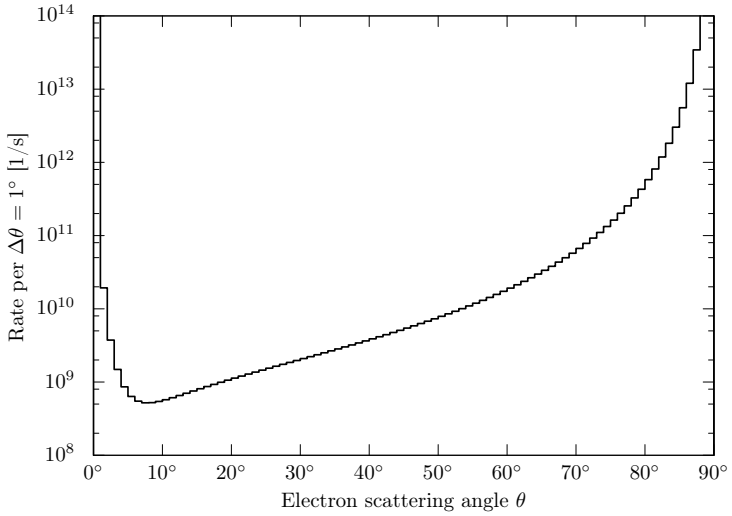

FIG. 23: The rate of Møller electrons on a 1° detector with 2π azimuthal coverage for the design luminosity of $6 \times 10^{35}\text{cm}^{-2}$ and an incident beam energy of 100 MeV.

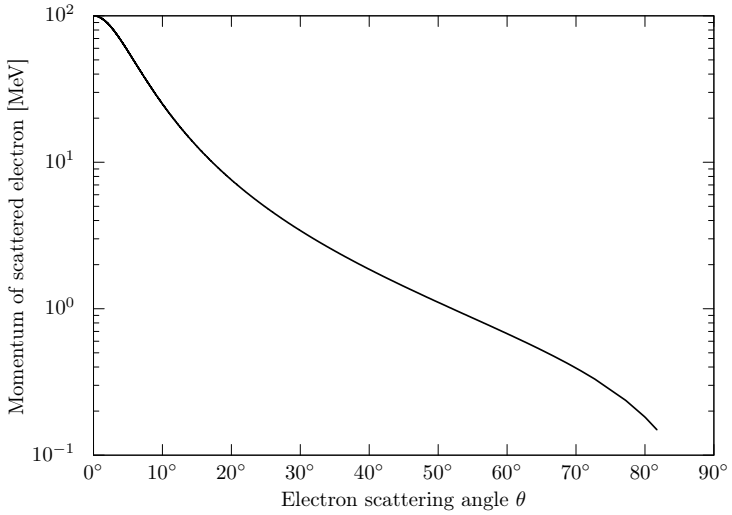

FIG. 24: The momenta of Møller electrons as a function of the scattering angle for an incident energy of 100 MeV.

3. QED background rate

The QED background process $e^- p \rightarrow e^- p e^+ e^-$ represents a smooth, irreducible background process for DarkLight on which the peak representing the decay of the A′ is sought. It has been calculated in detail in [50] which has been used extensively in the design described in this proposal. For example, the QED irreducible rate within the acceptance of

the detector described here is estimated at about 1 kHz, which is a manageable rate.

4. Summary of design constraints

The DarkLight detector must be able to detect with high efficiency an electron-positron-proton final state in the presence of a large QED background rate. This leads to a number of design constraints as follows:

- A magnetic field is required to both provide an invariant mass resolution of order 1 MeV and to shield the detectors from background process, e.g. Møller scattering and showering from halo particles. The longitudinal field of magnitude 0.5 Tesla is provided by a normal conducting solenoidal magnet. The solenoid will accept all scattered electrons from 25° to 165 °.

- Leptons from 5 MeV to 100 MeV must be tracked within the solenoid. A cylindrical GEM-TPC will be used to track the leptons. In addition, a scintillator hodoscope will be configured outside of the cylindrical tracker.

- The target will be a windowless storage cell with three stages of differential pumping on each side of the target. The silicon recoil proton detector will be located inside the gas volume.

- The final state proton will have a kinetic energy from about 1 to about 5 MeV. Two 300 μm silicon layers will be located around the gas target to detect the low energy, recoiling protons. This will be in the trigger at a high level.

- The elastic rate peaks in the forward direction for the final-state electron and at around 90° for the final state proton. By building a detector with no electron acceptance forward of 25° one would reduce the elastic rates very significantly. The minimum angle of detection needs to be determined in the context of maximizing the signal-to-noise. Correspondingly, the recoil proton rates are peaked at angles $\approx 90°$. The recoil protons from events where an e^+e^- pair is produced are all located forward of about 60° - see top right panel of Fig. 14 from [50].

- The total elastic electron-proton rate for a detector with electron detection only for $\theta > 30°$ and for proton detection $\theta_q < 60°$ is of order a few MHz from the above table.

B. Magnet

To meet its physics goals DarkLight requires a magnet to assist in the tracking detection of charged particles. In addition, a magnetic field is required to shield the detector from the very high rate of very low energy background electrons. A solenoid around the beam line and enclosing the detector elements can provide a longitudinal field of sufficient strength to both mitigate the background and allow for momentum analysis of charged leptons. An iron-type yoke around the solenoid is needed to provide a flux return. This in turn can substantially improve the field uniformity over the detection volume and can be used as part of the mechanical support of the solenoid. In the DarkLight pre-proposal a toroidal magnet was also considered as a design option. Although a toroid meets the field requirements in the detection region it would require the addition of a holding field around the target region to block the low energy background. Thus the adoption of the solenoid with a yoke return is seen as the most appropriate choice, one that will require a careful mapping of the magnetic field in the region of interest.

The magnetic field strength of the solenoid is chosen to be 0.5 T in order to trap most of the low energy background and allow electrons and positrons of interest to reach the detection region. The solenoid inner radius has to start around 30 cm from the axis to accommodate for the target and the detector elements. A preliminary design of the solenoidal magnet surrounding the target region is shown in Figure 25 where dimensions are given in mm. A cylindrical yoke 10 cm thick, with two end caps, and an inner radius of 50 cm is proposed to be made of C1010 steel.

The characteristics of the copper conductors chosen for this design are listed in Table VI. These conductors are commercially available and approximately half the area of the conductor is used for the water cooling bore. Table VII lists some of the yoke dimensions and the parameters that characterize how the conductors are arranged to form the solenoid coils. There are seven coil layers, each layer has 67 loops along the axis of the solenoid yielding a solenoid length of 1.48 m. The total number of turns is $7\times67 = 469$ and the conductor total length comes out to be 1237 m.

Table VIII lists some of the electrical and cooling main parameters. For a field strength of about 0.5 T the solenoid needs to be operated at a current density of about 516 A/cm^2 making it possible to cool the conductors using inlet water at room temperature. The mean

TABLE V: Specifications for the DarkLight magnet.

Field	0.5 T
Yoke outside radius	600 mm
Yoke length	1700 mm
Yoke outside chamfer	100 x 100 mm x mm
Coil inner radius	335 mm
Coil outer radius	490 mm
Coil length	1487 mm
Poletip hole radius	100 mm
Coil layers (radial)	7
Coil windings (long.)	67
Current	1274.6 A
Packing fraction	0.504
Coolant fraction	0.232 (m^3 water)/(m^3 coil)
Conductor	19.1 x 19.1 mm x mm
Cooling passage	12 mm

Height (mm)	Width (mm)	Corner (radius) (mm)	Cooling (dia) (mm)	Insulation (thickness) (mm)	Total area $(mm)^2$	Conductor area $(mm)^2$
19.1	19.1	2.5	12	1.5	488.4	246.3

TABLE VI: Dimensions of the normal conductors for the 0.5 T solenoid.

water temperature doing operation is 35 °C. The power dissipated by the solenoid is 151 kW.

The solenoidal magnet of Fig. 25 has been modeled with the code OPERA. The solenoid was built using a single coil, 1.48 m long with inside and outside radii of 33.5 cm and 49.1 cm, respectively. The solenoid was surrounded by a cylindrical yoke made of steel C1010 with the dimensions as shown in Fig. 25. The magnetization curve used in the code for the material C1010 is shown in Figure 26. The magnet was located inside a cubic volume of 27 m^3. The current density was set to approximately match the parameters presented in

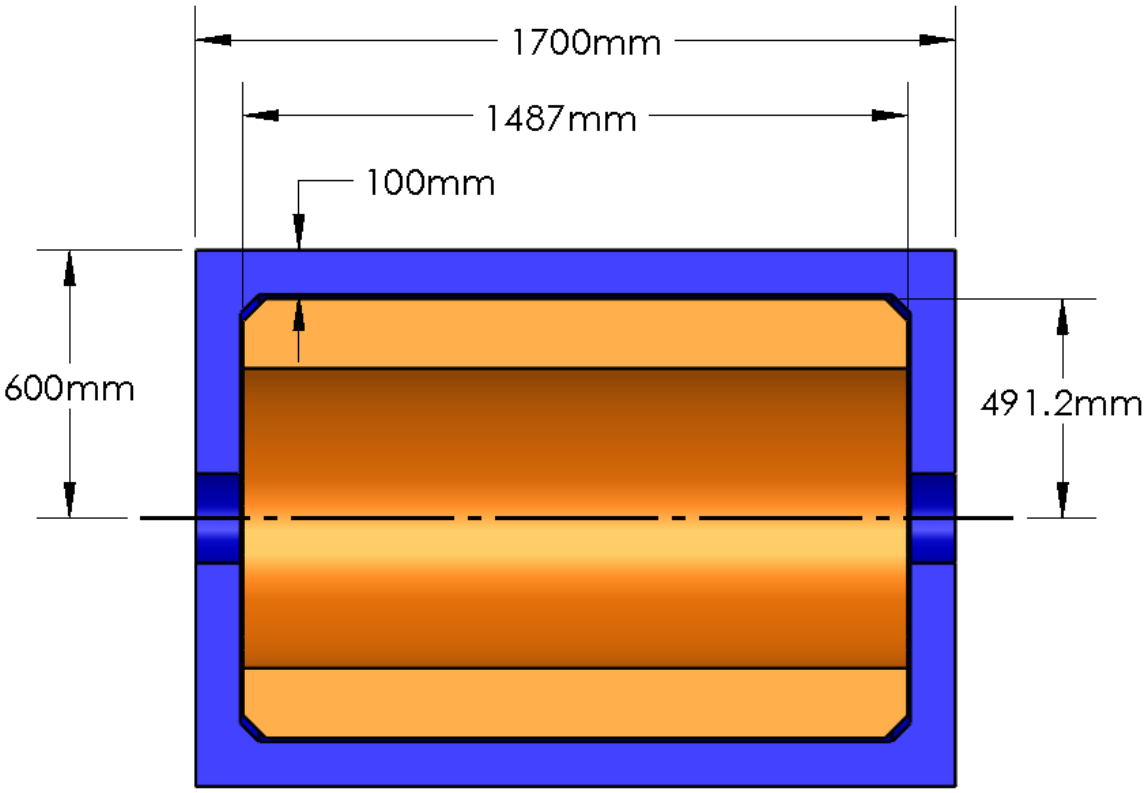

FIG. 25: Preliminary engineering concept of the solenoidal magnet.

Yoke (in/out radius) (m)	Yoke (length) (m)	Coil (layers)	Coil (length) (m)	Coil (loops)	Total turns	Conductor (total length) (m)
0.5/0.6	1.7	7	1.49	67	469	1237

TABLE VII: Yoke dimensions and conductor coil arrangements.

Current (A)	Flux (A-turns)	Resistance (series) Ohm	Voltage (V)	Power (kW)	T_{water} (in/out) (°C)	Δ P (per cooling path) (atm)
1273	597037	0.093	119	151	20/50	4.2

TABLE VIII: Operational parameters for the 0.5 T solenoid.

Tables VII and Table VIII.

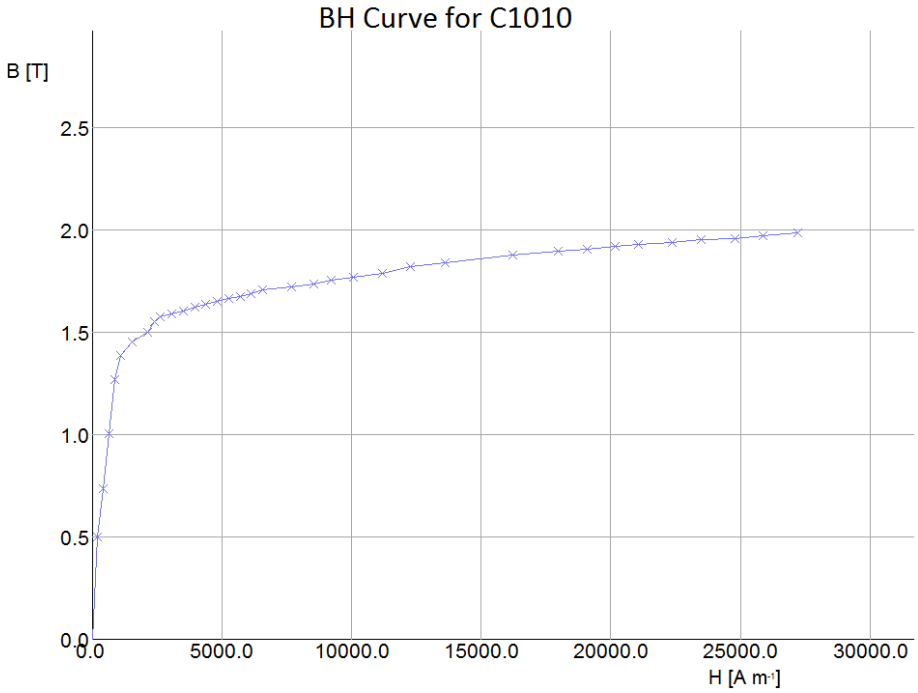

FIG. 26: Magnetization curve for steel C1010 as implemented in the code OPERA.

A view of the solenoid and the yoke is shown in Figure 27. Only a quarter of the yoke is shown to illustrate the interior. The color code on the yoke indicates the field strength there and the scale used is shown on the axis at the left of the figure. The figure on the right is a close up of the corner of the cylinder with the end cup and the field on this sharp corner of the yoke is very high bringing the yoke material close to saturation. To reduce this effect the proposed design as shown in Fig. 25 has a 45° cut around this sharp corner.

The magnitude of the magnetic field along the z-axis, i.e. beam line, is shown in Fig. 28. One curve shows the field due only to the coils while the most uniform curve is that obtained when the yoke is added to the solenoidal coil. The field is also very uniform over the detection region as can be seen in Fig. 29 that shows a color profile of the magnetic field magnitude on the yz-plane covering about 1.6 m along the beam line and about 1.2 m in the vertical direction. The field throughout most the yoke is constant, about 0.65 T, except on the sharp corners as already noted. In this regime the value of the field inside the yoke is very dependent on the sharp rise in the magnetization curve before saturation.

The trajectories of elastic scattering electrons from hydrogen have been calculated for the above magnetic field configurations. The scattered electron angles and energies correspond

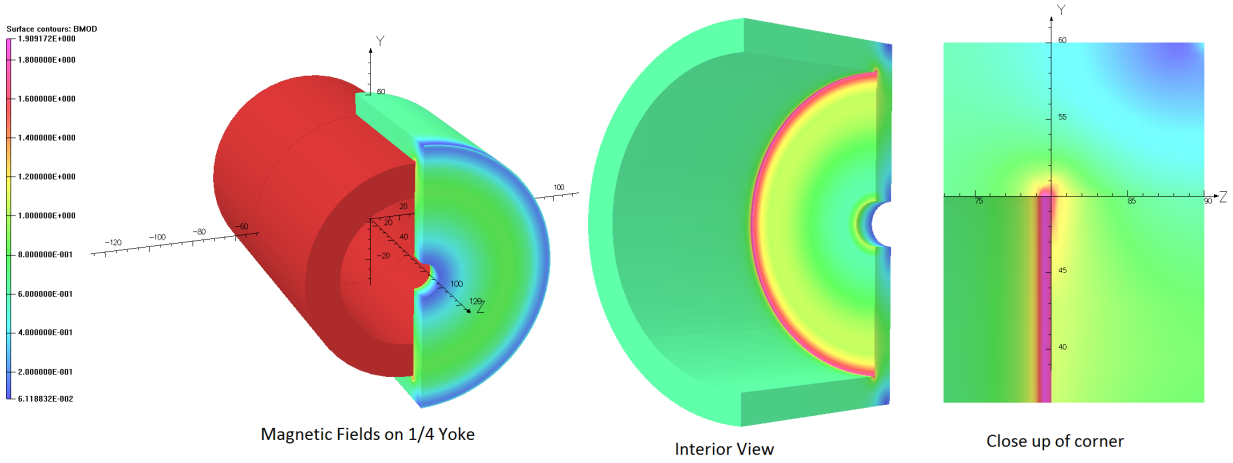

FIG. 27: The solenoid and the yoke as built in the code OPERA. The color code on the yoke represents field strength, the scale used is on the left. The picture on the right is a close up of the corner between the cylinder and the end cup of the yoke.

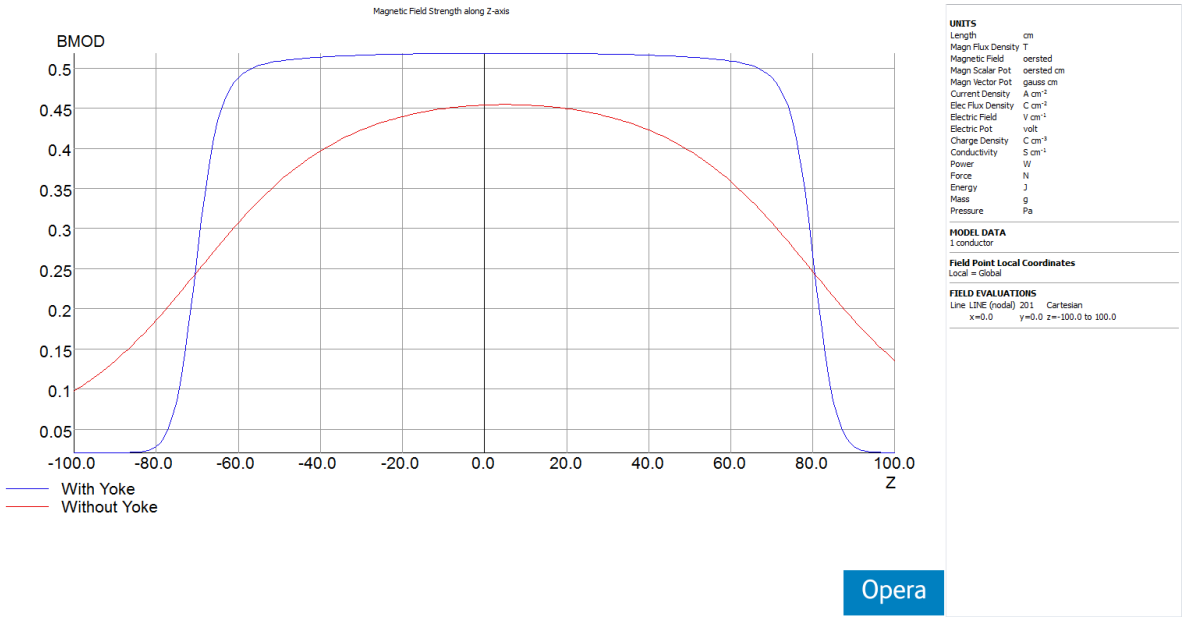

FIG. 28: Magnitude of the magnetic field along the beam line, field is in T and distances in cm. The curves are for the field with and without the yoke around the solenoidal coil.

to those from elastic scattering. The trajectories are shown in Figure 30 and are drawn in the $y-z$ plane, where y is the vertical direction and z the beam direction. Tracking electron detectors are expected to cover the entire z-range shown and the y-range between 15-35 cm approximately.

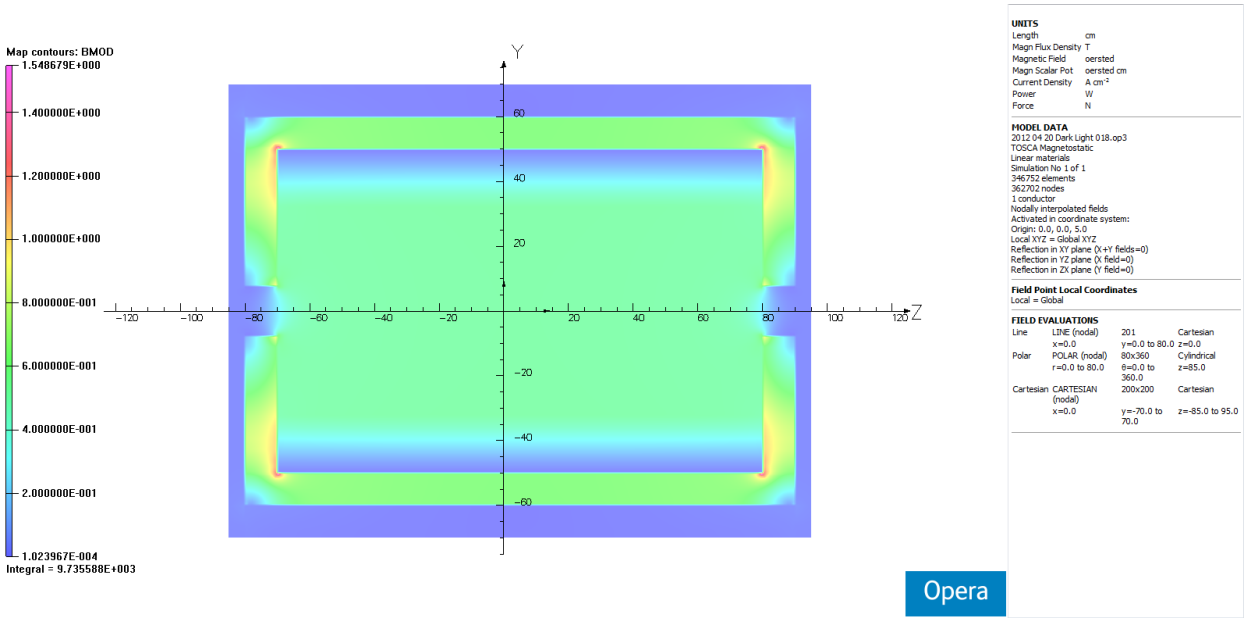

FIG. 29: Magnetic field profile on the yz-plane.

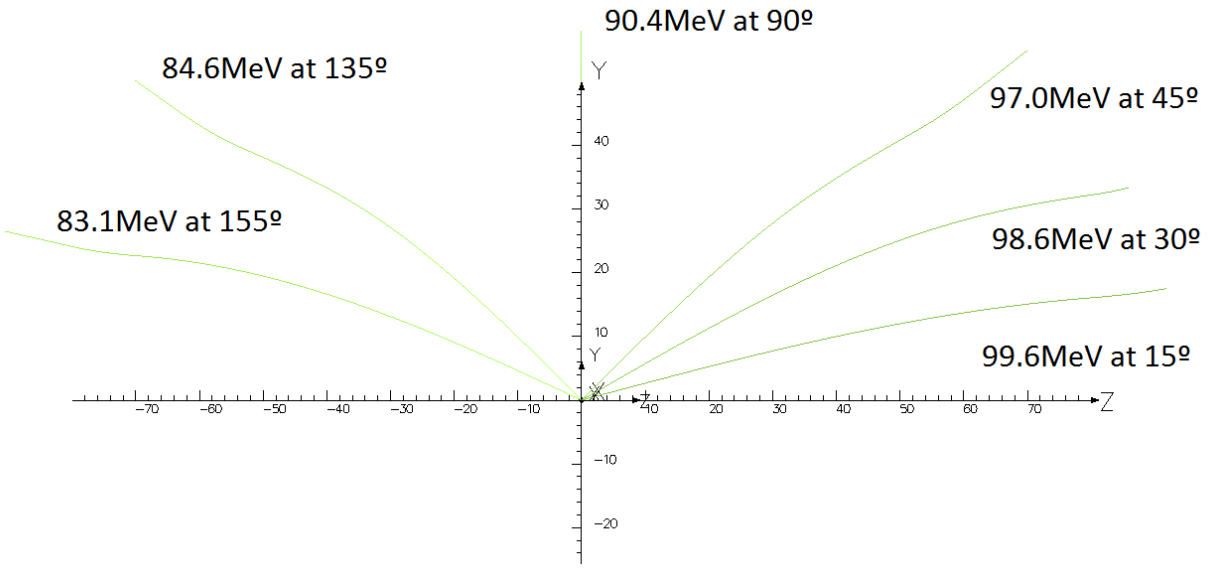

FIG. 30: Trajectories of electrons scattered elastically from hydrogen for a 100 MeV electron beam.

The DarkLight experiment requires the detection of the elastically scattered protons whose energy are in the few MeV range, and the detection of electron and positrons within the 10-50 MeV range, in addition to the elastic electrons. The proposed field does not affect significantly the proton trajectories while allowing leptons of at least 10-15 MeV to reach past the 15 cm into the lepton tracking system. This is illustrated in Figure 31 for 1 MeV

protons and in Figure 32 for 30 MeV electrons.

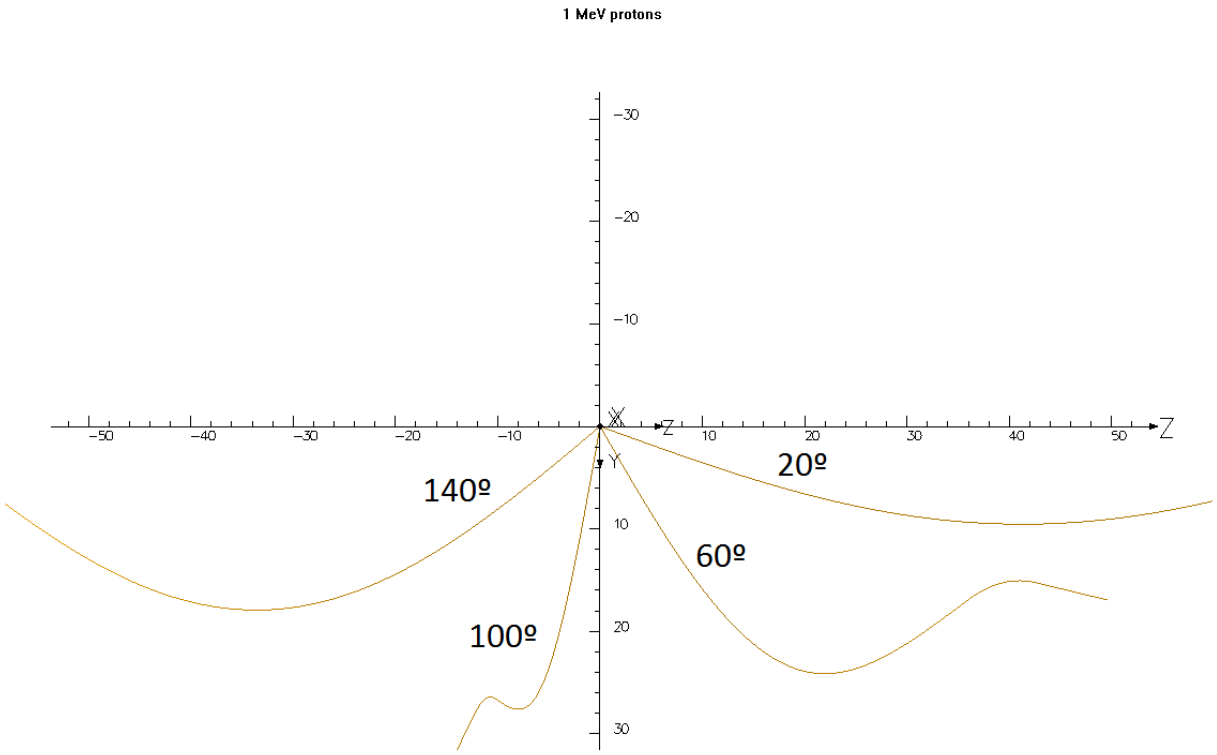

FIG. 31: Trajectories of 1 MeV protons as function of the scattering angle.

The design of the mechanical structure of the proposed magnet is driven by the weight of the entire device. The magnetic forces on the proposed coil configuration are about a tenth of the weight of the magnet.

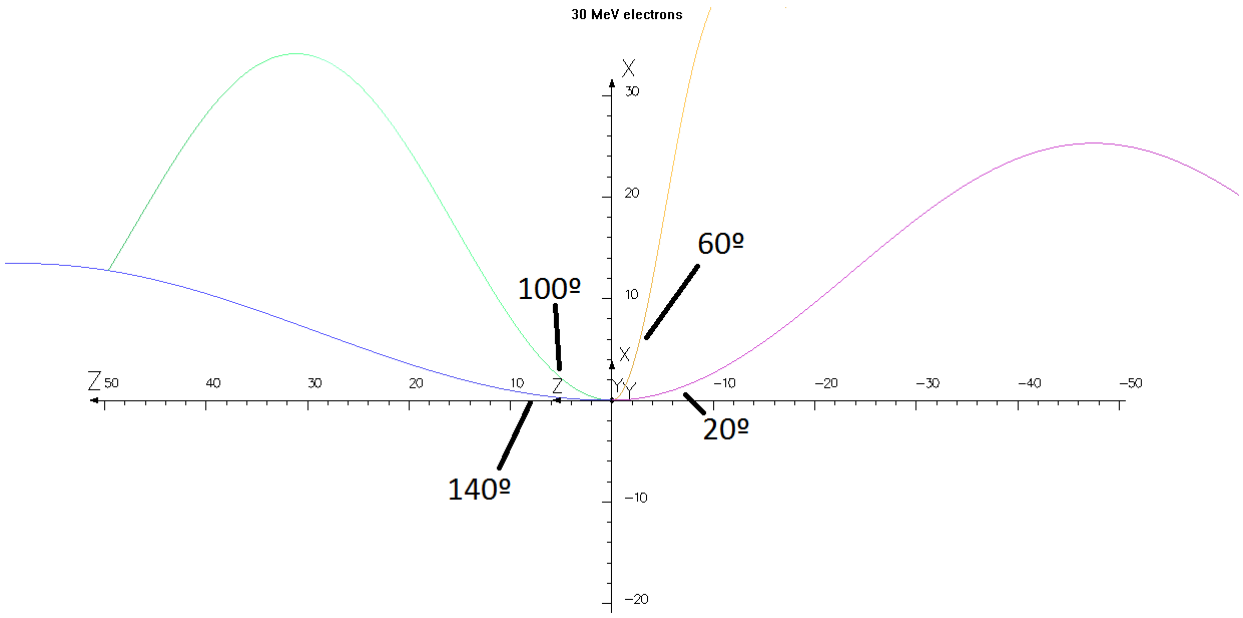

FIG. 32: Trajectories of 30 MeV electrons as function of the scattering angle.

C. Detectors

1. Lepton tracker

The lepton tracker in DarkLight must detect the final state e^- in coincidence with the e^+e^- pair from QED and via the A' decay. It must have the following characteristics:

- operate in a high rate (of order GHz) environment
- have low ($< 1\%$ rad. length) material thickness to provide 1 MeV resolution in the mass of the A′
- have cylindrical geometry in a solenoidal magnet
- provide a position resolution of 250 μm
- trigger at a rate of about 1 kHz

The GEM-TPC developed by the GEM-TPC collaboration from Technische Universität München, HISKP Bonn, GSI Darmstadt, SMI Wien, and Universität Heidelberg [49], originally motivated by the proposed Panda experiment at FAIR, GSI, Darmstadt, Germany, is very well matched to the above requirements and is the proposed technology for DarkLight.

The GEM consists of a 50 μm thin insulating Polyimide foil with copper coated surfaces, typically 2 to 5 μm thick. The foil is perforated by photo-lithographic processing, forming a dense, regular pattern of (double-conical) holes. Usually the holes have an inner diameter of 50 μm. A large GEM-TPC prototype has been constructed, as shown in Fig. 33, and has been operated successfully [51]. It is a 60% scale prototype of the proposed DarkLight tracker and its characteristics are described in Table IX.

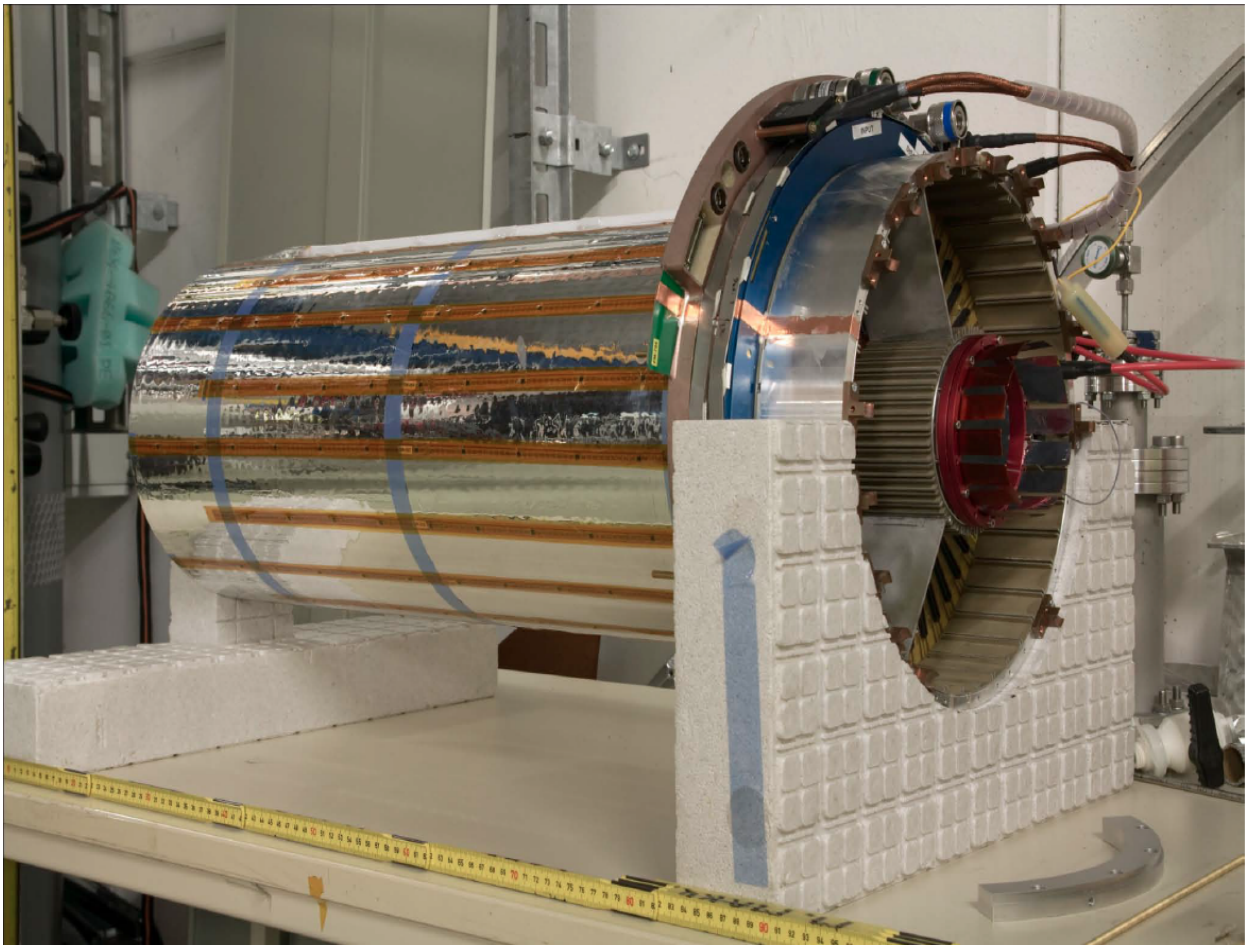

FIG. 33: Photograph of the prototype constructed by the GEM-TPC collaboration.

The GEM-TPC prototype material thickness satisfies the design requirements as shown in Fig. 35. . The GEM-TPC prototype has been installed in the FOPI detector at GSI and was used for data taking in 2011. It will also be used in the Crystal Barrel detector at ELSA, U. Bonn, Germany. The TPC operates continuously as an analog event pipeline.

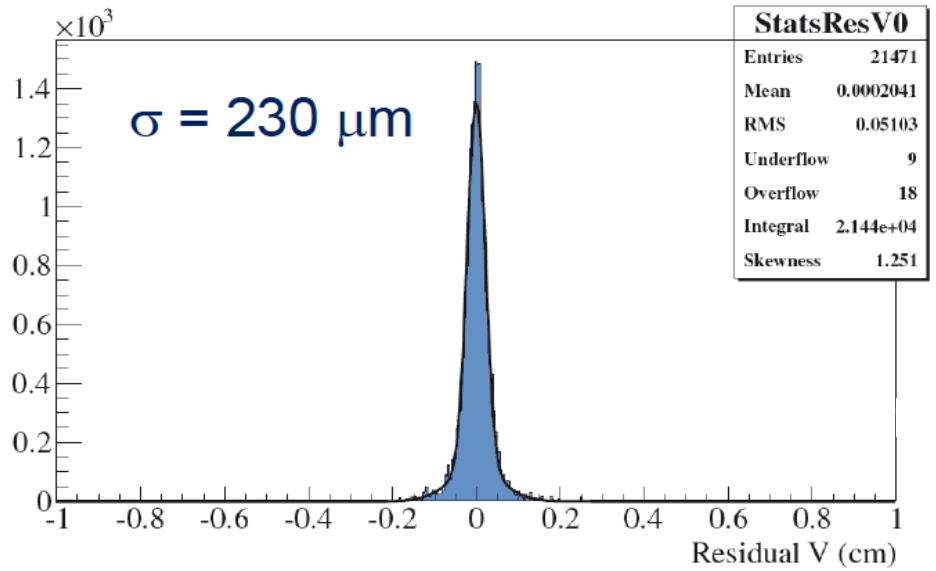

FIG. 34: Spatial resolution of the GEM-TPC prototype determined using cosmic rays. Here the field was 360 V cm^{-1} and the gain was 3700. The magnetic field was zero.

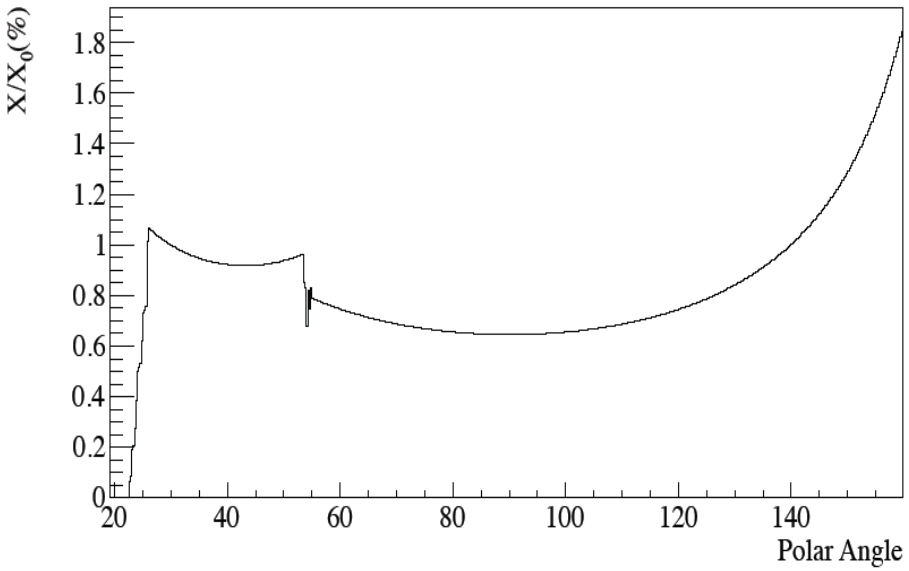

FIG. 35: Radiation length vs. polar angle for the GEM-TPC prototype [49].

TABLE IX: Characteristics of the GEM-TPC prototype [51, 52].

Drift length	725 mm
Outer diameter	300 mm
Inner diameter	105 mm
Triple GEM stack	gain O(1000)
10254 channels	
AFTER T2K analog sampling readout	
Gas	Ar(Ne)/CO_2 (90/10)
Position resolution (σ)	250 μm

The readout electronics is based on the AFTER T2K chip and the sampling frequency is 10 to 50 MHz based on an external clock.

Electronics and Data Acquisition

The electronics for the GEM TPC prototype has to fulfill two important requirements, to cover long electron drift times up to 25μs and to cope with high channel densities. The AFTER ASIC [53] developed for the TPCs of the near detector of T2K was the only available chip that satisfyied these requirements. As the TPC is a full 3D tracking device, it delivers large event sizes due to the high granularity in space and time. A full occupancy event in the TPC prototype corresponds to an event size of 20 MB assuming 32 bit per sample.

The AFTER chip is a low noise ASIC developed for the T2K near detector TPCs [54], which operates at low event rates. It has 72 input channels and a low power consumption of 11 mW/ch. All the important parameters of the components can be set by the slow control of the chip. The preamplifier charge range can be chosen to be from 120 fC to 600 fC. The shaper has an adjustable peaking time in the range from 116 ns to 1.9 μs. After the shaper the signals are sampled into an analog buffer which is implemented as two switched capacitor arrays (SCA) each with 36 channels and a depth of 511 samples. Each of the SCAs has two internal channels not connected to the input which can be used to correct for common mode noise, fixed pattern noise and SCA-leakage. The sampling clock is supplied from outside and can be programmed in the range from 10-50MHz. Up on a trigger the content of the SCA is multiplexed to the output at a frequency of 20 MHz. The main parameters of the AFTER ASIC can be found in Table X.

TABLE X: Main specifications of the AFTER ASCI [54].

Number of channels	72
Samples per channel	511
Dynamic range	120-600 fC (4 values)
Peaking time	100 ns to 2 μs (16 values)
Sampling frequency	1 to 50 MHz
Readout frequency	20 to 40 MHz

Due to the extremely high data rate of interactions per second the selection of physics events requires a continuous readout of all detectors without any pre-knowledge from a hardware trigger. This means all detectors have to perform a standalone online event reconstruction. In a second step every detector has to contribute to the event selection by identifying the physics events and filtering out backgrounds. In a third step one selects the event by combining the information of all detectors to finally build and reconstruct a physics event online.

2. Inner silicon detector

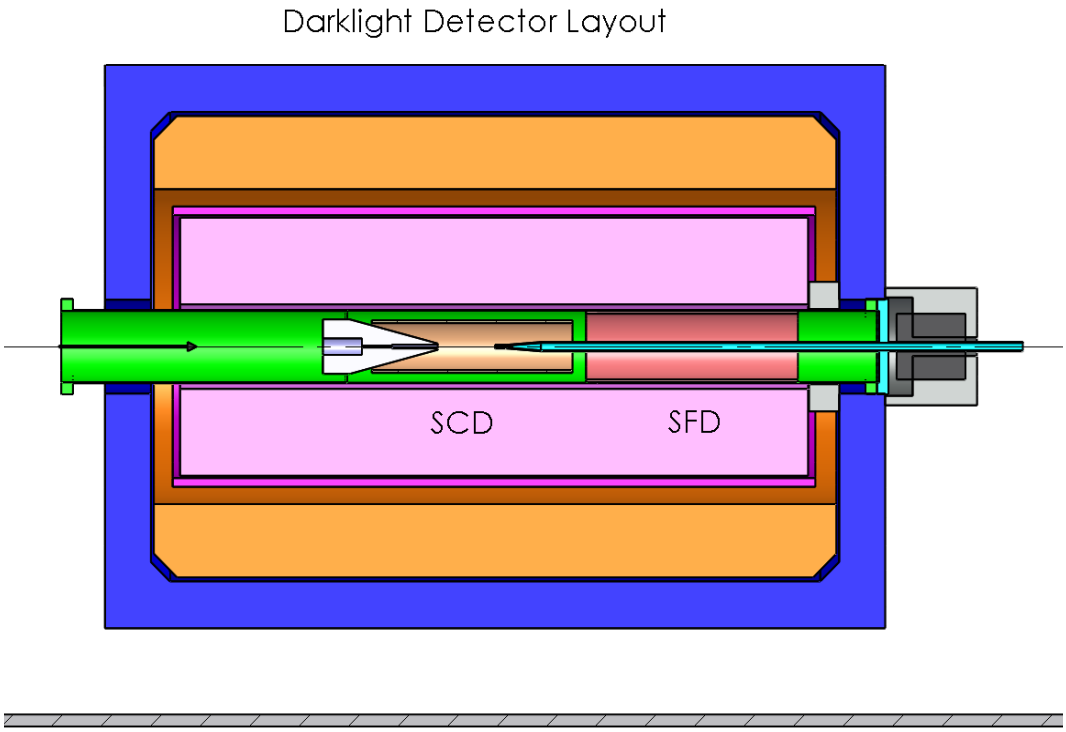

FIG. 36: Layout of the DarkLight experiment highlighting the location of the Silicon Central Detector (SCD) and the Silicon Forward Detector (SFD).

The silicon system of the DarkLight experiment serves two functions, the tagging and energy measurement of the recoil proton at the level of a few MeV in kinetic energy and the measurement of the hit location of final-state leptons. The layout is meant to aid the identification of recoil protons compared to final-state leptons. The silicon detector system is divided into two parts:

- Silicon Central Detector (SCD) (Polar angle range: $17° - 163°$)
- Silicon Forward Detector (SFD) (Polar angle range: $6.1° - 19°$)

Figure 36 shows the layout of the DarkLight experiment highlighting the location of both detector systems. The layout of this system is based on two independent sensors addressing the need for recoil proton and lepton measurements covering rather different energy ranges.

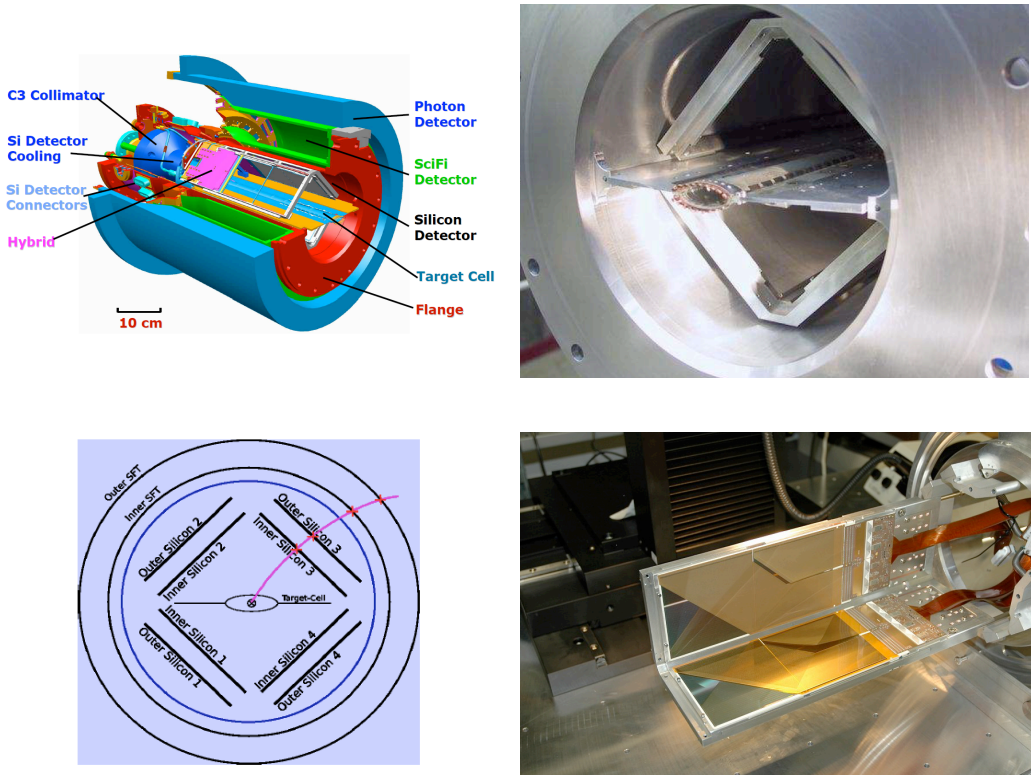

FIG. 37: Overview of the HERMES Proton Recoil Detector.

There are several examples of silicon sensor based detector systems focusing on measuring the energy and hit location of recoil nuclei such as the CNI polarimeter system at RHIC [55] and the proton recoil detector at HERMES [56]. Both silicon systems are operated inside the actual beam vacuum. Figure 37 provides an overview of the HERMES proton recoil detector. The silicon detector is based on four large double-sided silicon sensors stations each with two sensors referred to as inner and outer silicon. The silicon system for the DarkLight experiment is based on conventional, well-understood single-sided silicon sensors providing a robust silicon detector scheme while at the same time avoiding a long and costly R&D phase.

The first two sections discuss the requirements, followed by a description of the layout, the design concept and specifications. The last three sections focus on silicon ladder concept, the silicon sensors with a brief remark on the cooling system at the end.

The DarkLight silicon detector systems, i.e. the SCD and the SFD (Figure 38), will be operated inside the actual beam vacuum. This addresses in part the need for minimizing the dead material which is expected to stay below 1% X_0. A careful design on the choice of

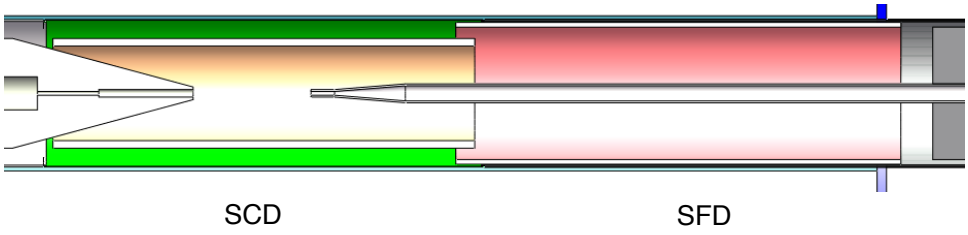

FIG. 38: Side view of the silicon-detector system for the DarkLight experiment with the Silicon Central Detector (SCD) and the Silicon Forward Detector (SFD).

any support and service material is mandatory minimizing outgas rate. The following list summarizes all basic requirements:

- Central and forward measurements of recoil proton and final-state leptons covering a polar angle range of $17° - 163°$ and $6.1° - 19°$, respectively.
- Proton recoil energy and location measurement.
- Linearity in energy response for the proton recoil measurement.
- Hit location of final-state leptons.
- Dead material in active detector area below 1% X_0.
- Low outgas rate of any active and passive material.
- Radiation hard silicon sensors.
- Fast readout system to potentially contribute to the actual trigger system.
- Liquid cooled system of the chip front-end electronics.

Figures 39 and 40 show a cross-section view of the SCD and SFD, respectively together with a list of basic design parameters. Figures 41 and 42 show a side view of the SCD and SFD, respectively.

Both detector systems consist of three ladder arrangements each with a central rigid ceramic support frame. The support frame material has to be carefully chosen to provide proper rigidity and good thermal conductivity while at the same time minimizing outgassing.

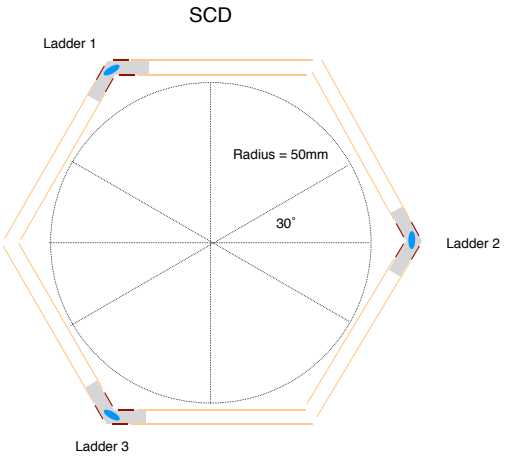

- Radius: 50mm
- Φ-coverage: 360˚
- θ-coverage: 17˚ - 163˚
- Number of ladders: 3
- Ladder length: 430mm
- Sensor dimensions: 56.5mm X 60.0mm / 52.5mm X 60.0mm
- Number of sensors: 28 per ladder
- Sensor thickness: 300µm
- Total number of sensors: 84
- Power dissipation: 0.3W per chip / 50W per ladder
- Radiation tolerance of sensors: 1MRad
- Radiation tolerance of readout chip: >>1MRad

FIG. 39: Cross-section view of the DarkLight Silicon Central Detector (SCD).

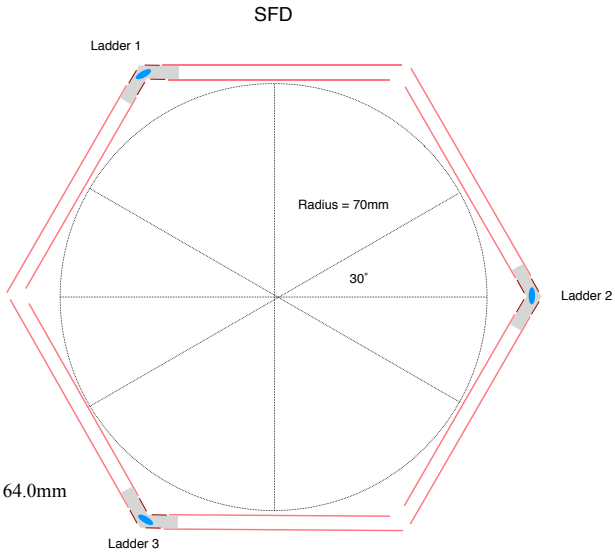

- Radius: 70mm
- Φ-coverage: 360˚
- θ-coverage: 6.1˚ - 19˚
- Number of ladders: 3
- Ladder length: 458mm
- Sensor dimensions: 78.5mm X 64.0mm / 72.5mm X 64.0mm
- Number of sensors: 28 per ladder
- Sensor thickness: 300µm
- Total number of sensors: 84
- Power dissipation: 0.3W per chip / 50W per ladder
- Radiation tolerance of sensors: 1MRad
- Radiation tolerance of readout chip: >>1MRad

FIG. 40: Cross-section view of the DarkLight Silicon Forward Detector (SFD).

The support frame has an embedded cooling tube. Each support frame will support two silicon sensors on either side with a total of seven silicon senors in a row as shown in Figures 41 and 42, respectively. Each sensor is only held in place on one side. The actual active area therefore consists of only two 300μm thick sensors providing a total radiation length of approximately 0.65% X_0. The inner most sensor and the front-end electronics part will be optimized for the recoil proton measurement while the outer sensor is focusing on the hit location measurement of the final-state leptons. The combination of both is meant to aid in distinguishing recoil protons from final-state leptons.

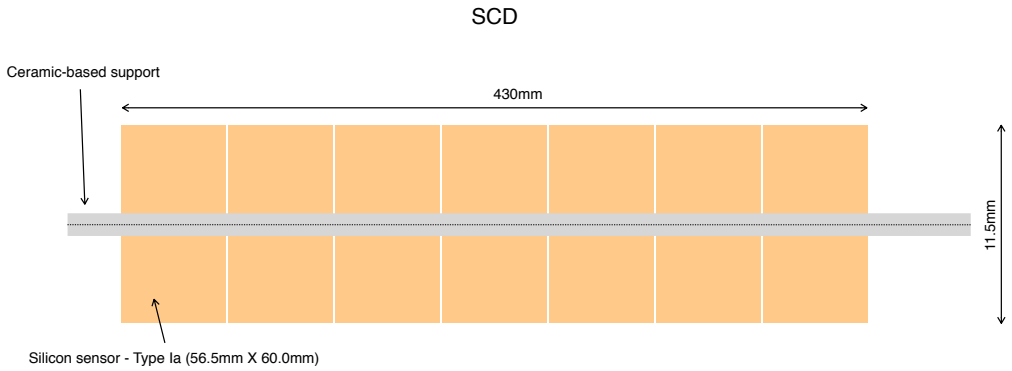

FIG. 41: Side view of the DarkLight Silicon Central Detector (SCD).

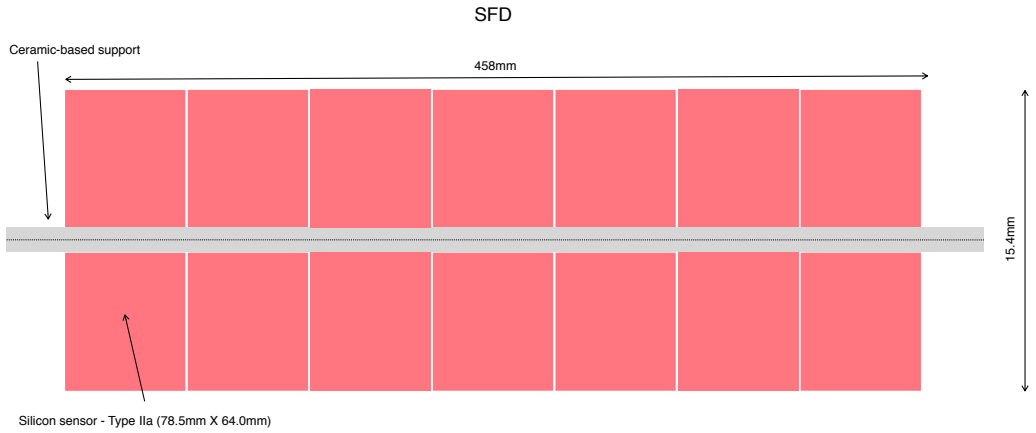

FIG. 42: Side view of the DarkLight Silicon Central Detector (SCD).

Figure 43 shows a cross-section of a ladder for the Silicon Central Detector (SCD) (left) and the Silicon Forward Detector (SFD) (right). Each sensor is glued on a central ceramic-

based support frame in addition to the actual readout chip. Three ladder arrangements are needed for the SCD and SFD.

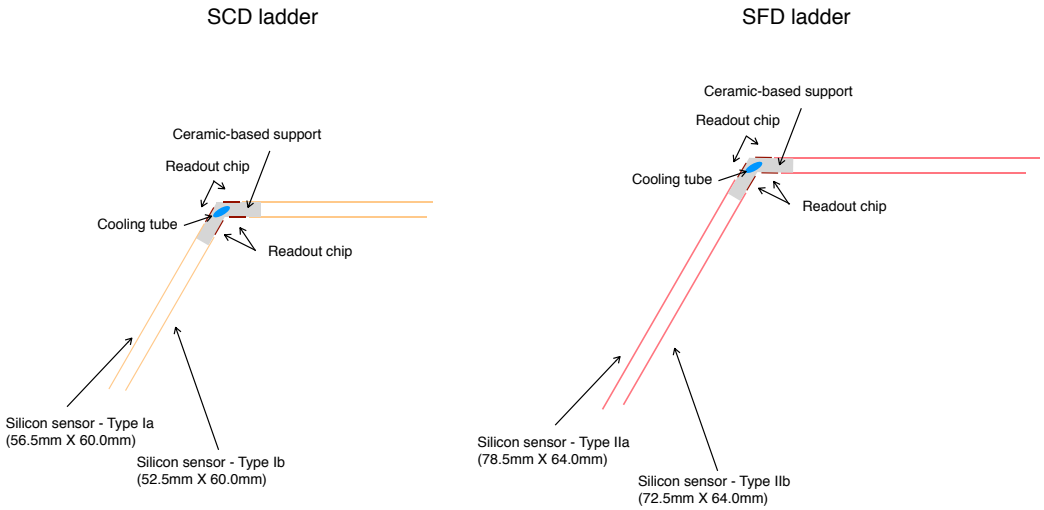

FIG. 43: Cross-section of the ladder.

As discussed earlier, the sensors are based on single-sided silicon sensors, specifically double-metal layer sensors. The manufacturing techniques for such silicon sensors are well established. The preference is to produce single sided devices with p-implants on n-bulk silicon and poly-silicon biased. Those sensors are relatively easy to produce with high yields and can also be handled without much difficulty in a standard semi-conductor lab. In contrast, double-sided devices have lower yields (thus more expensive) and need special equipment to handle them. Several experiments such as PHOBOS [57] and STAR [58] have extensive experience in dealing with those type of sensors. The final choice of a readout chip has not been made yet as well as the actual layout of the readout hybrid. Figure 44 shows a cross-section of a double-metal silicon sensor. Those type of sensors are radiation hard sensors at the level of 1 Mrad.

The expected heat dissipation for each silicon system is about 50W per ladder, 150W for the whole system of SCD and SFD each. A liquid cooling system is mandatory and would add at most 0.2% X_0.

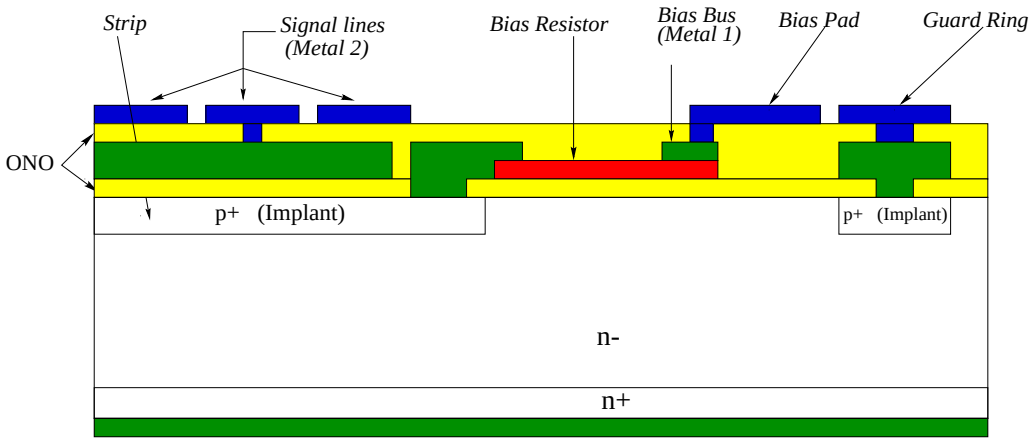

FIG. 44: Silicon pad sensor.

3. Scintillator detector

Surrounding the GEM TPC is a simple calorimeter aimed at detecting photons as a veto for the invisible decay mode search as described in A 1. The detector is located at a radius of 300 mm and consists three layers of lead (2cm, 2cm and 1 cm) interleaved with three layers of 1 cm thick, 10 cm wide scintillator bars, for a total of 68 scintillator bars. We anticipate reading out each bar with three scintillating fibers with each end connected to a 16 channel PMT located outside the magnet, giving a total of 408 channels or 27 PMTs. This scheme has been used by MINOS with good results.

The photon spectrum from $e^- + p \rightarrow e^- + p + \gamma$, a potential pileup background for the invisible search, is shown in Fig. 45 and lies in the 10-30 MeV region, so the appropriate measure is the photon cross section on lead, which is 50 b in this energy region. This gives an attenuation length of 6 mm or a 96% probability of interaction in each 2 cm layer of lead. We anticipate using the third layer as a coincidence. This gives a better than 99% probability of a photon interacting in the lead with detectable energy making it in to the neighboring scintillator. Timing may be used to locate the interaction locating to within 10 cm along the bar, allowing the identification of isolated photons. The efficiency of the system will be dominated by the gas between the scintillator bars and should be better than 95% for photon above a few MeV.

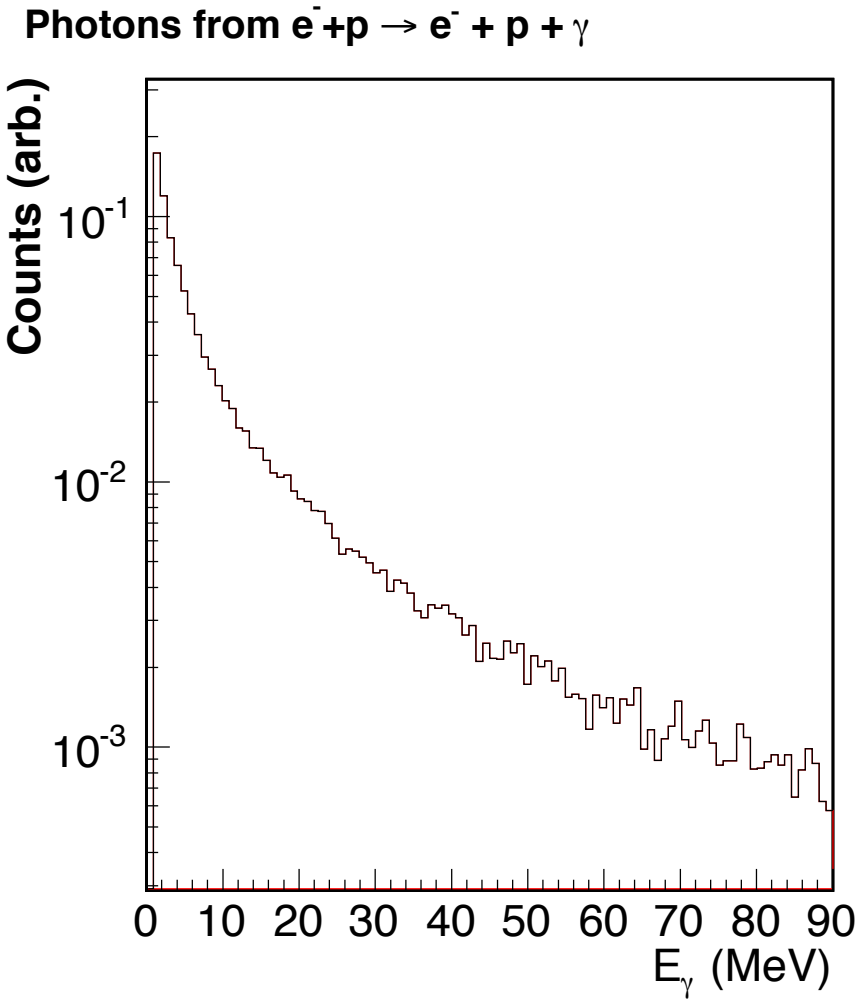

FIG. 45: Photon spectrum from $e^- + p \rightarrow e^- + P + \gamma$.

D. Target

1. Concept

The conceptual design of the target is shown in Fig. 46. The target gas is contained inside a beam pipe between two small-diameter outflow channels centered on the beam axis upstream and downstream of the interaction region. The upstream outflow channel is embedded in a massive tungsten collimator designed to absorb any beam halo outside the channel diameter. The channel is recessed from the collimator exit to shield the detectors from electrons scattered from the channel entrance edge. The target gas parameters for a hydrogen target at room temperature are listed in Table XI. The gas pressure required to produce a target thickness of 10^{19} atoms/cm^2 in a 10 cm long interaction region results in viscous laminar gas flow through the outflow channels. The corresponding gas flow characteristics (Mach number η, Reynolds number R_e, pressure p, and target thickness t) at the entrance to the outflow channels of 2 mm diameter and 5 cm length are shown in Fig. 47 as functions of the outflow rate Q. These rates of tens of Torr-liter/s require sizable blower-type pumps at the first stages of the vacuum pumping cascades. To handle the required gas flow rates of tens of Torr-liter/s and reduce the gas pressure in the beam pipe to levels below 10^{-8} Torr required by the FEL, a set of three pumping stages is needed starting with a large mechanical booster pump followed by two turbo pump stages separated by flow limiters.

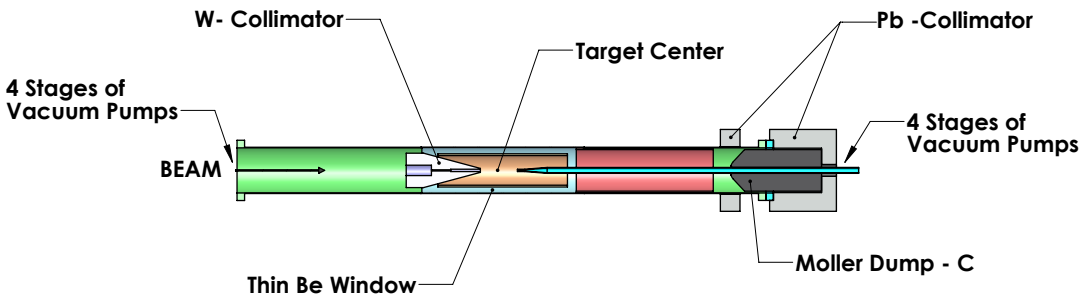

FIG. 46: Schematic layout of the proposed DarkLight windowless hydrogen gas target.

The innermost proton detectors inside the target gas volume are dimensioned to lie outside the envelope of Møller electrons emanating from the interaction region and contained by the

magnetic field. The Møller envelope is shown in Fig. 46. Near the exit from this field, the Møller electrons are absorbed in a Møller dump made of graphite to minimize showering and shielded with lead. The pipe containing the gas and the proton detectors contains a section made of beryllium in the region of acceptance (25^o to 165^o) for electrons in order to minimize electron scattering.

TABLE XI: Gas target specifications for the DarkLight experiment.

Outflow channel diameter	D=2 mm
Outflow channel length	l= 5 cm
Mach number at channel entrance	$\eta = 0.18$
Reynolds number at channel entrance	$R_e = 250$
Target pressure	$p = 12$ Torr
Target thickness	$t = 10^{19}$ atoms/cm^2
Gas outflow rate in each channel	$Q = 15$ Torr-liter/s

In addition, we have considered the possible use of plasma windows [59] to provide a conductance limiter to generate the required target thickness. A plasma window's viscosity and high temperature allows the separation of gas at pressures ≈ 1 atmosphere from vacuum. It could allow larger diameter conductance tubes and reduce the gas flow. Fig. 48 shows a possible layout using 6 mm diameter plasma portholes. This option is under consideration.

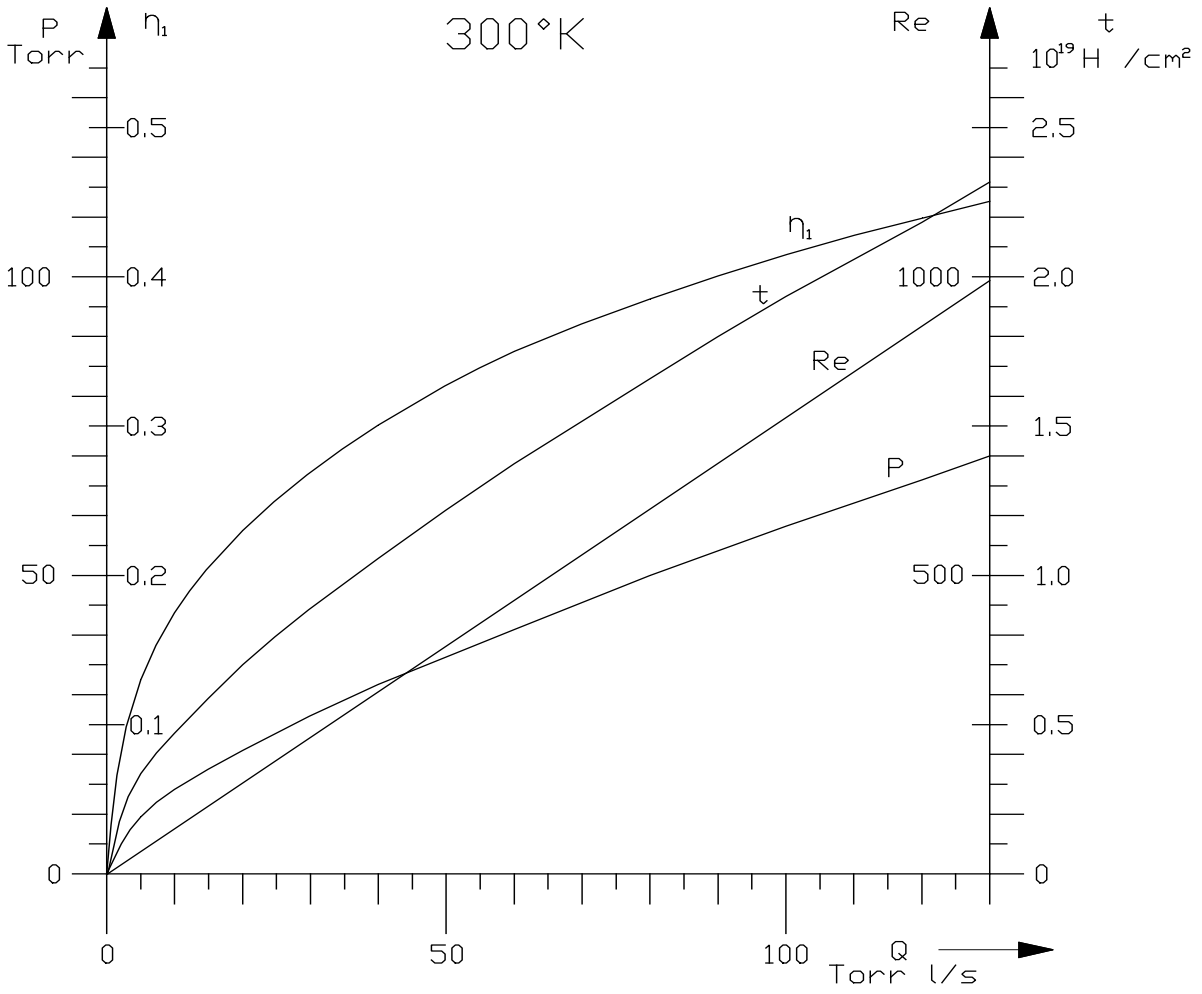

FIG. 47: Gas flow characteristics vs. outflow rate Q.

2. Beam interaction with the target

Calculations of the interaction of the 100 MeV electron beam and the gas target have been carried out for both hydrogen and xenon targets. While DarkLight is initially proposed

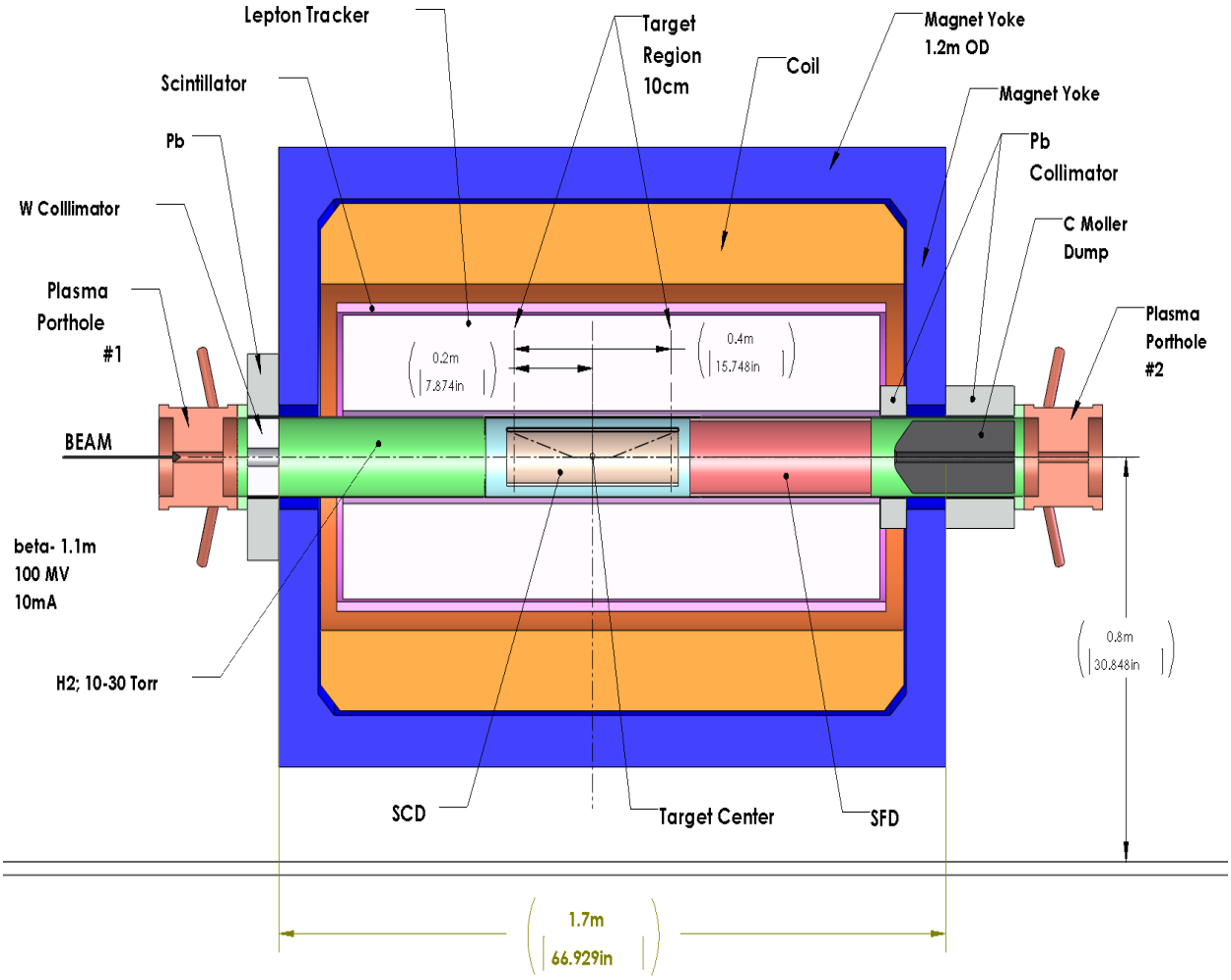

FIG. 48: Schematic layout of target with plasma windows .

using a hydrogen target, the possibility to use a heavier gas target is also considered. Two processes contribute significantly to energy loss and two processes contribute significantly to electron loss due to beam spreading.

Ionization

The energy loss for an electron traveling through a material due to ionization is given by this version of the Bethe-Bloch equation [60]:

$$-\frac{dE}{dx} = 2\pi r_e^2 m_e c^2 \rho Z \frac{1}{\beta^2}\left[\ln\frac{\tau^2(\tau+2)}{2(I/m_e c^2)^2} + F(\tau) - \delta - 2\frac{C}{Z}\right]$$

$$F(\tau) = 1 - \beta^2 + \frac{\frac{1}{8}\tau^2 - (2\tau+1)\ln 2}{(\tau+1)^2}$$

where τ is the kinetic energy of the electron in units of the electron mass. The electrons are energetic enough that the shell-correction is definitely negligible ($C = 0$). The mean excitation potentials are $I_{\mathrm{H}} \approx 19$ eV and $I_{\mathrm{Xe}} \approx 482$ eV.

From [61], we can estimate the density effect in hydrogen with:

$$\delta_{\mathrm{H}} = 4.6X - 9.6 + 0.035(3.5 - X)^{6.79}$$

$$\delta_{\mathrm{Xe}} = 4.6X - 12.7 + 0.133(5.0 - X)^{3.02}$$

When $X = \log_{10}(\beta\gamma) = \log_{10}(200) \approx 2.30$, we get $\delta_{\mathrm{H}} \approx 1.2$ and $\delta_{\mathrm{Xe}} \approx 0.6$.

Putting this all together, we get that the energy loss due to ionization is

$$\Delta E_{\mathrm{H}}/\sigma_{\mathrm{H}} = (2.6 \times 10^{-25}\ \mathrm{MeV\ cm^2})34.5 \approx 8.8 \times 10^{-24}\ \mathrm{MeV\ cm^2}$$

$$\Delta E_{\mathrm{Xe}}/\sigma_{\mathrm{Xe}} = (1.4 \times 10^{-23}\ \mathrm{MeV\ cm^2})28.6 \approx 4 \times 10^{-22}\ \mathrm{MeV\ cm^2}$$

For a target of thickness 10^{19} hydrogen atoms cm^{-2}, these energy losses are negligible.

Bremsstrahlung

When $E_0 \gg 137 m_e c^2 Z^{-1/3}$, we can use complete screening as an approximation. The total cross subsection is given by:

$$\frac{d\sigma}{d\omega} \approx 4\frac{\alpha r_0^2}{\omega} Z(Z+1)\left[\left(1 - \frac{2}{3}\varepsilon + \varepsilon^2\right)\ln\frac{183}{Z^{1/3}} + \frac{1}{9}\varepsilon\right]$$

where

$$\varepsilon = \frac{E_0 - \hbar\omega}{E_0}$$

The energy loss is given by multiplying the cross subsection by the photon energy and integrating over all possible photon energies (approximately ε from 0 to 1):

$$-\left(\frac{dE}{dx}\right) = N\int_0^{E_0/\hbar} \hbar\omega \frac{d\sigma}{d\omega} d\omega = N E_0 \alpha r_0^2 Z(Z+1)\left(\frac{1}{18} + \ln 183\right)$$

Thus, the energy loss over the cross-subsectional density is

$$\Delta E_{\mathrm{H}}/\sigma_{\mathrm{H}} \approx 4 \times 10^{-25}\ \mathrm{MeV\ cm^2}$$

$$\Delta E_{\mathrm{Xe}}/\sigma_{\mathrm{Xe}} \approx 7 \times 10^{-22}\ \mathrm{MeV\ cm^2}$$

Again, for the design target thickness of 10^{19} hydrogen atoms cm^{-2}, these energy losses are negligible.

Mott Scattering

Since the mass of the nucleus is large compared to the energy of the electron, we will neglect recoil of the proton and use the center-of-mass Mott cross subsection:

$$\frac{d\sigma}{d\Omega} = \left(\frac{Ze^2}{2E}\right)^2 \frac{\cos^2\theta/2}{\sin^4\theta/2}$$

Integrating over the solid angle:

$$\sigma = (6 \times 10^{-30}\ \mathrm{cm^2}) Z^2 \int_{\theta_c}^{\pi} \cot^3(\theta/2) d\theta \approx (2 \times 10^{-29}\ \mathrm{cm^2}) Z^2 {\theta_c}^{-2}$$

θ_c is the acceptance angle for the beam after interaction with the target. If we pick $\theta_c = 1\,\mathrm{mrad}$, for example, the cross subsection for hydrogen is 3×10^{-23} cm^2 and for xenon is 9×10^{-20} cm^2.

Møller Scattering

The scattering angle of the higher-energy electron is given by:

$$\cos^2\theta = \frac{(E_0 + mc^2)(E_0 - E)}{(E_0 - mc^2)(E_0 - E + 2mc^2)}$$

and for the lower-energy electron:

$$\cos^2\theta' = \frac{(E - mc^2)(E_0 + mc^2)}{(E_0 - mc^2)(E + mc^2)}$$

as determined by kinematics, where E is the final energy of the electron initially at rest. The total cross subsection is

$$\sigma = 2\pi \frac{Z^2 e^4}{mc^2} \int_{E_c - mc^2}^{E_0/2} \frac{1}{E^2} dE$$

to first order. $\theta_c = 1\,\text{mrad}$ corresponds to an energy of $E_c - mc^2 = 0.01$ MeV. This corresponds to a cross subsection the same size as the Mott cross subsection for both hydrogen and xenon.

E. Integration

The Darklight detector occupies a small footprint while having a full array of detectors. See Figs. 49 and 50. This will present challenges in assembly as well as providing services to the detector. The limited space will drive many of the design features for the magnet and detectors.

The fact that the magnet is a solenoid means that we cannot easily have a split magnet design. The magnet therefore will be of a barrel design. The detectors and vacuum system will have to be designed to be inserted from the ends of the magnet. We will design the magnet endcaps to be easily removable to accommodate this constraint and allow assembly of the detectors and vacuum system.

The lepton tracker and scintillator detector will have a cradle support. The proton detector and collimator will be located and supported inside the vacuum system. The vacuum system will then be instrumented with cabling and cooling services. This assembly will then be inserted into the lepton tracker and attached via kinematic mounts to the cradle support of the lepton tracker. This sub-assembly will then be inserted into the magnet bore via assembly fixturing. The cradle support will then be mounted to the magnet steel. In the design of the magnet and sub-systems we will have to be sensitive to providing adequate space for these supports and services.

The gas system will be remotely located. Due to the high flows the vacuum system will be substantial. However, most of the pumping will take place outside of the footprint of the Darklight detector so integration will be more important in regards to the inlet and outlet beamline.

The Darklight detector as a whole will be mounted on rails to allow retraction and insertion into the beamline. This assists us in assembly of the system. This will also allow us to perform limited repair in the event of equipment failures.

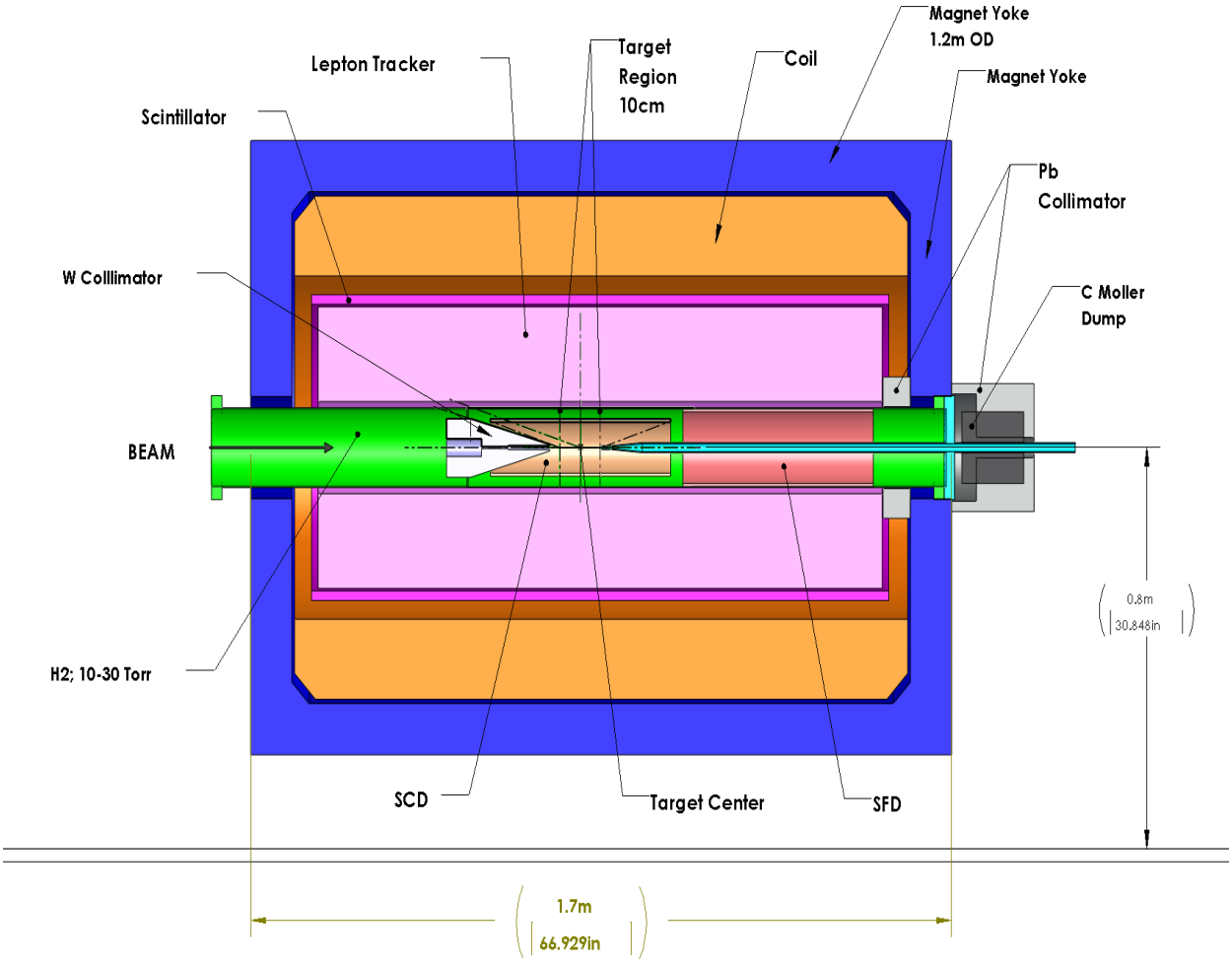

FIG. 49: Schematic layout of the DarkLight experiment.

F. Trigger

The resonance signal of A′ decay lies on top of a large QED background and both must be detected amidst even larger elastic scattering and Møller rates. These large rates require a trigger able to select events with a proton and three leptons in the final state. We propose a trigger concept as follows:

- The TPC tracker will be used as the primary trigger source. The estimated rate in the TPC is 20 MHz. The inner radius of the tracker is at 100 mm from the beam line to exclude the high rate M øllers.

- The current TPC prototype uses the AFTER readout chip.

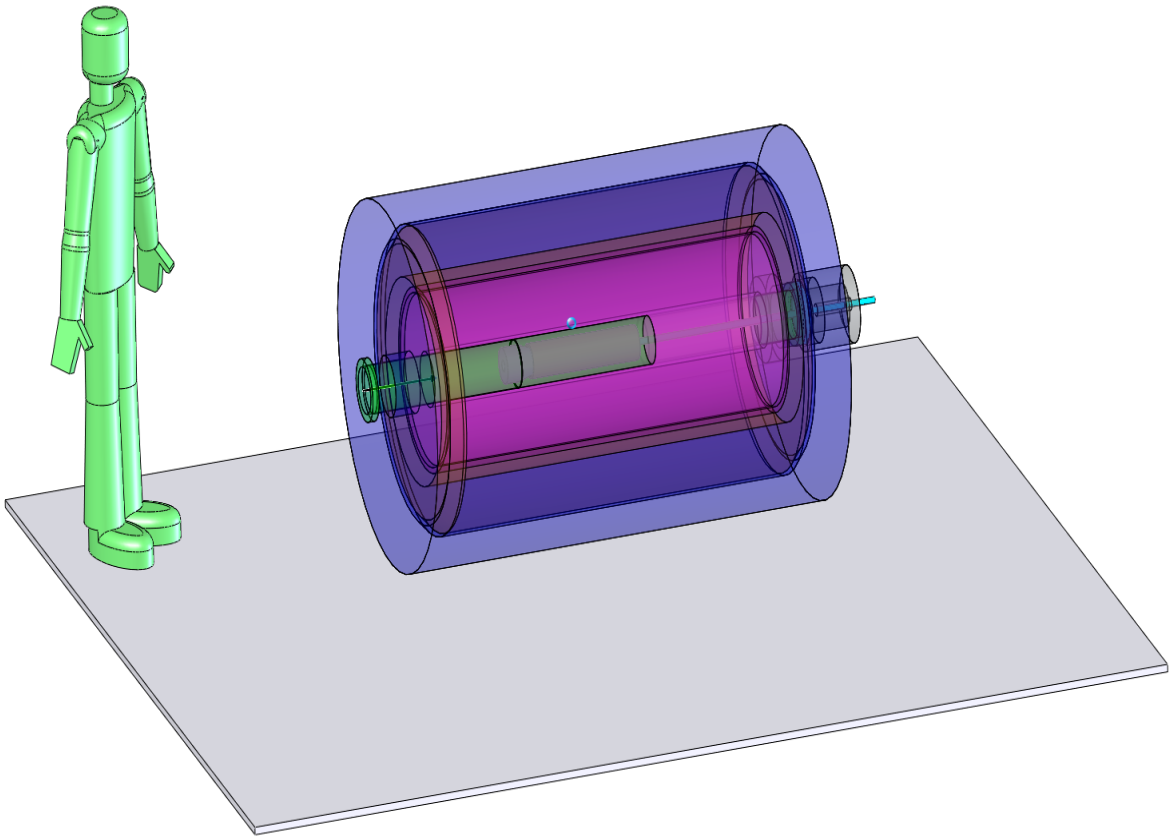

FIG. 50: The scale of the DarkLight experiment.

- Data from the readout chip is then digitized (if not already) and fed into the trigger pipeline. The pipeline will perform the following:

  - Hit Detection, determining which channels had charge collected above a certain threshold
  - Zero Suppression, removing channels which were not hit from the data stream
  - Preliminary Track Construction, collecting hits which are in close proximity to each other in space and time
  - Track Angle Determination, calculating the angle of the track based on the time difference between the start and end points of the track
  - Charge Determination, calculating the charge based on the curvature of the track in the magnetic field

  - Data-packaging to DAQ, tagging data with a time stamp, compressing if necessary, and sending to Data Acquisition Computers.

- Triggers will be issued by the system based on the angle of the tracks and number of particles. One example is triggering on a lepton with $\theta > 90^o$ as well as having 3 lepton tracks. We estimate trigger rate here of 1MHz.

- The next level trigger uses inputs from the proton detector to further require that a proton with energy > 0.5 MeV was detected.

- We estimate that this will result in a 10 kHz trigger rate which will be fed into the event builder and written to disk.

- We may also consider using the S-ALTRO chip developed by CERN. The S-ALTERO chip provides onboard ADC conversion, baseline correction, and zero suppression. This will reduce the data-rate in the next stage of the trigger, and reduce the processing power required. The SPADIC chip is another readout possibility.

We believe that such a hierarchical trigger scheme can provide the efficiency rates necessary for the experiment.

VI. EXPECTED PERFORMANCE

The DarkLight experiment offers unique ability to search for resonances in the 10-100 MeV range because of three important features:

- Full reconstruction of the four particle final state with reasonable efficiency and resolution.

- Average invariant mass resolution for the e^+e^- pair resulting from an A' of 1 MeV across the entire kinematic range

- Reasonable photon identification for A' decays to invisible final states

Reconstruction of all final state particles presents the major advantage and key challenge to the DarkLight experiment. The reconstruction of all final state particles will allow strong

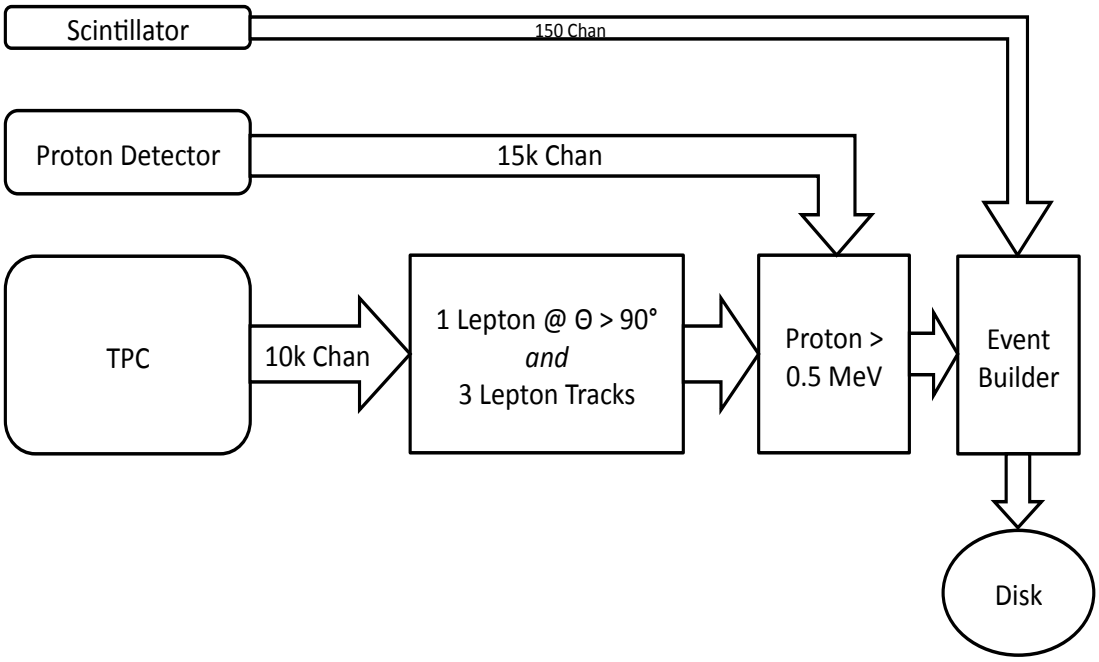

FIG. 51: Trigger block diagram for the DarkLight experiment.

application of kinematic constraints, leading to high background rejection. A tracking system extending from 105 to 300 mm in cylindrical radius ρ and in the forward directions acts to identify the final state leptons and measure their momenta precisely.

Fig. 52 shows how the e^+e^- pairs from the A' decay share energy. Near the upper kinematic boundary of the A' mass of 92 MeV, the A' is nearly at rest and the leptons come out with similar energies around 40 MeV, while at the lower end of the kinematic range, the energies of the leptons may be very different. We have carried out our planning based on optimizing the detector and run plan for A' masses in the 10-100 MeV range. We will discuss possible modifications to this below.

The geometrical design and choice of field are driven by the kinematics of the Møller and elastic backgrounds. The 0.5 T field (necessary to confine the Møller electrons) and the 50 mm inner tracking radius imposes a $p_T > 10$ MeV cut on the final state leptons. The elastic rates in the forward region restrict the minimum forward tracking angle to $\theta_l > 25°$ (there is no physics restriction on the backward scattering angle, but very few events lie

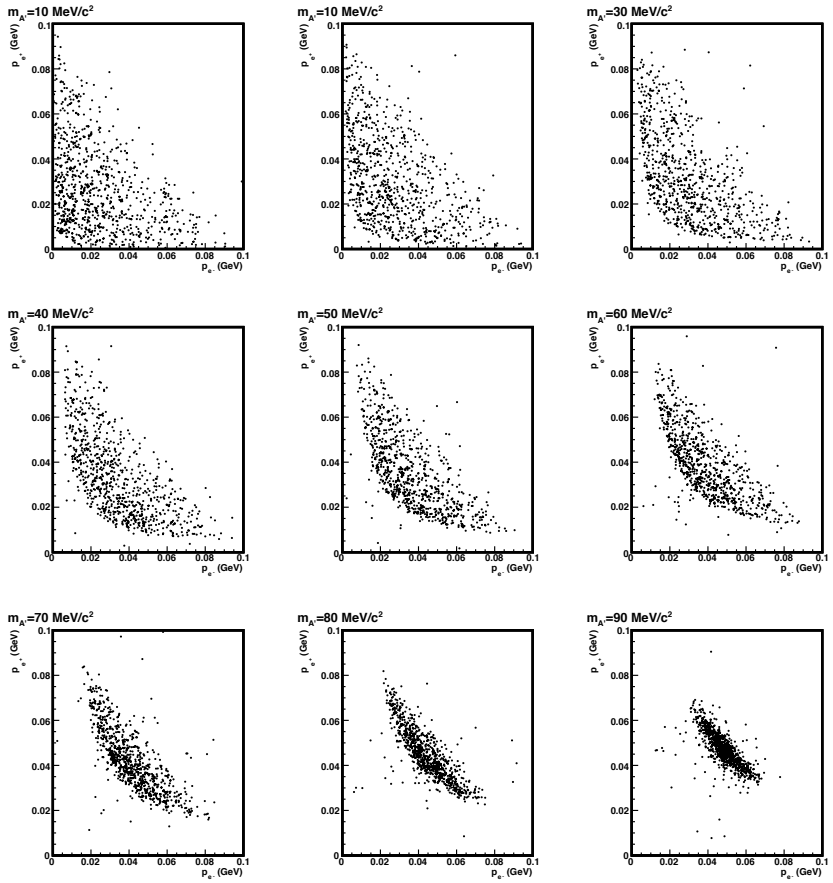

FIG. 52: Sharing of lepton momenta. Each scatter plot shows the reconstructed momenta of the e^+e^- pair for different A' masses.

in this region) and the elastic backgrounds restrict the minimum proton kinetic energy to $K_p > 1$ MeV. Combining these conditions gives an acceptance cross section as a function of A' mass shown in Fig. 53. For most of the cross section, the signal cross section lies in the range 0.01-10 pb and should be compared with the irreducible QED background cross section (across all A' masses) of about 10^5 pb.

Identification of the recoil proton also presents a key ingredient. Fig. 54 shows the ability of the silicon recoil detector to separate leptons from protons and the measurement of the proton energy. Detection of the proton is not the dominant limitation on the acceptance. However, the 30% uncertainty on the proton energy measurement does dominate the total uncertainty on the measurement of the total energy and momentum of the event, Fig. 54.

The second key feature of DarkLight is the e^+e^- invariant mass resolution. The GEM-TPC has demonstrated a momentum resolution of $\sigma_{p_T}/p_T = 0.06$ at $p_T = 200$ MeV (which

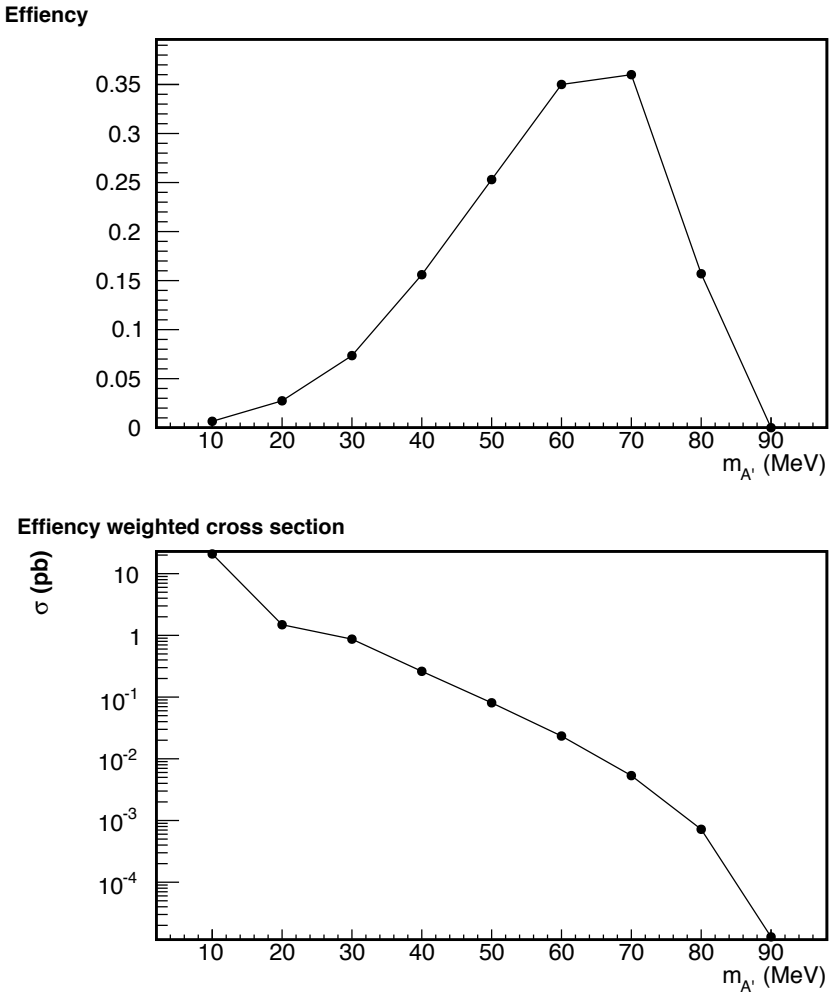

FIG. 53: The upper panel shows the four particle final state acceptance. Lower panel shows efficiency weighted cross section for $\alpha' = 10^8$. The lower efficiency at the low mass end results from loss of leptons with $p_T < 10$ MeV, as is apparent from Fig. 52.

scales like $1/\sqrt{p_T}$) over an angular range relevant for DarkLight and we have approximately verified this with our Monte Carlo. Along with the inner tracker wall, the proton detector and beam pipe in our current design total 0.01 X_o, giving an invariant mass resolution ranging from 0.2-2 MeV over the 10-100 MeV range, Fig. 55. This resolution is based on the measured resolution of the GEM TPC in [49], which has not been optimized for DarkLight.

Identification and measurement of all the final state particles will allow a constraints from the total energy and momentum of the system: event with total energy that does not add up to 100 MeV or momentum that differs from 100 MeV/c $\hat{z}$ will be rejected, reducing

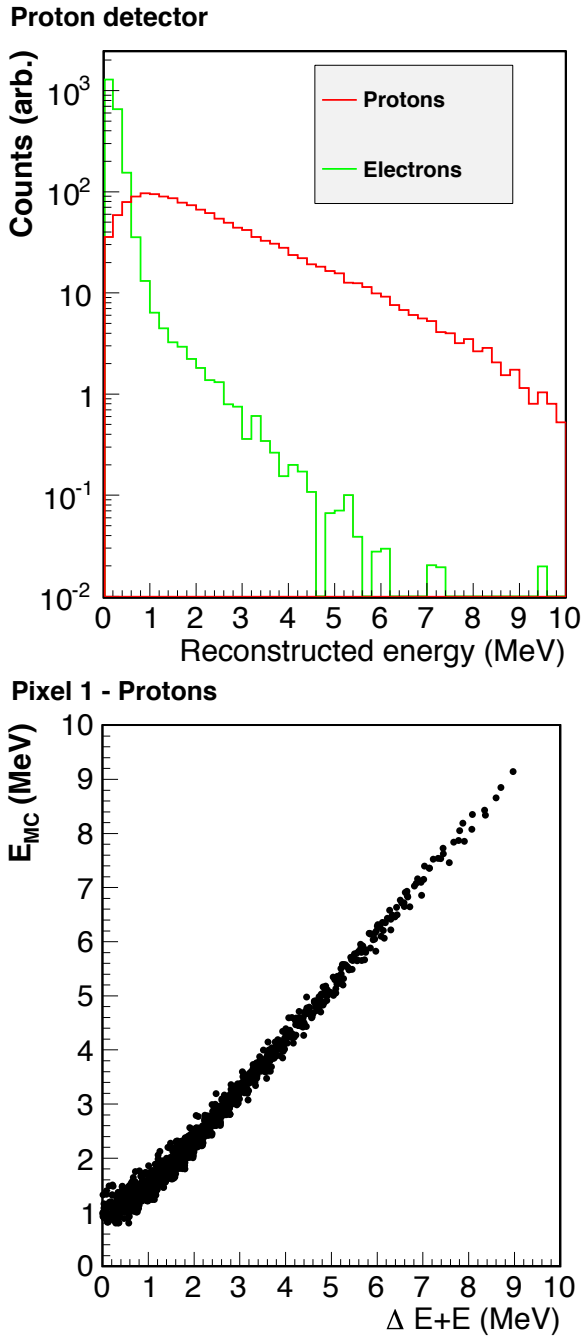

FIG. 54: The upper panel shows the separation between protons and electrons based on the particle's kinetic energy in a 1 mm^2 area on the proton detector. The lower panel shows the proton kineitc energy reconstructed from the pixel detector compared with the initial energy from the Monte Carlo. The bend at low energies is from energy loss of the proton in the target region of the detector.

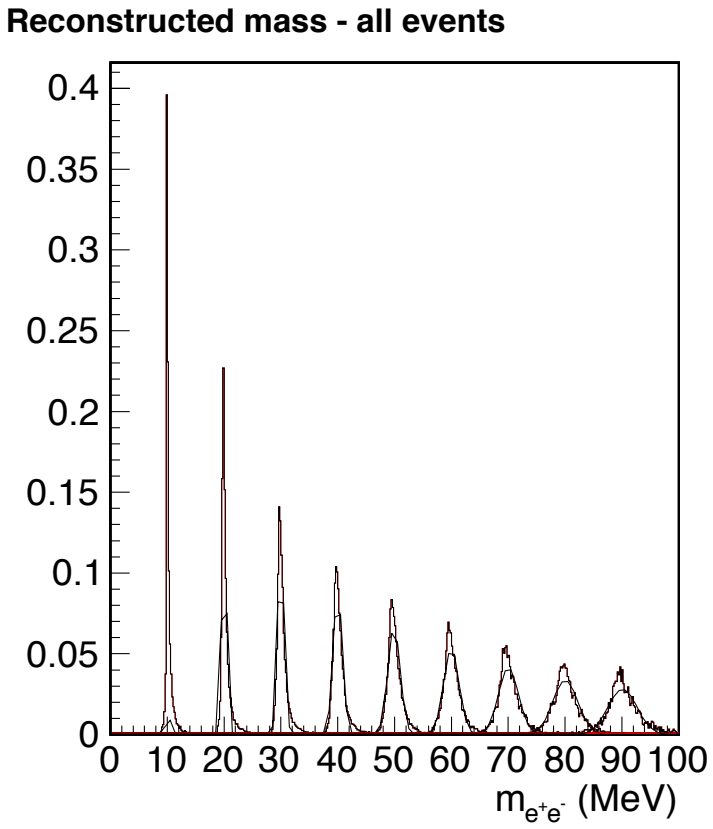

FIG. 55: The upper panel shows fits to reconstructed e^-e^+ masses for A' decays.

pileup. The power of this rejection will be ascertained from a full simulation. At this stage in the development of the experiment, we believe that simply identifying the four particle final state will result in very substantial background reduction from pileup.

The performance of the lead-scintillator calorimeter in vetoing photons as pileup- background to $e^- + p \rightarrow e^- + p + A'$, where the A' decays invisibly has not yet been carried out. The number of 95% detection efficiency above 10 MeV given in Section V C 3 represent a reasonable estimate.

VII. RESOURCES AND SCHEDULE

A. Resources

To continue the realization of the DarkLight experiment, resources will be required as follows:

- to support engineering and design of the experiment

  Assuming that the experiment is given a green light to proceed by PAC39, the collaboration would like to proceed with the technical design of the experiment in a timely way. The cost of the DarkLight experiment is estimated to be in excess of $ 2 million and the construction project will need to follow DOE order 413.3 A. It is estimated that about 38 man-months of engineering (mechanical, electrical, and vacuum) and about 12 man-months of drafting will be required to bring DarkLight from CD-0, through CD-1 to CD-2.

- to develop the required FEL 100 MeV electron beam

  To make progress on beam development, resources will be required to support FEL personnel and to provide for delivery of the FEL beam. We estimate that we will need the equivalent of 30 days running assuming 100% efficiency.

- An integrated production data taking luminosity of 1/ab. In terms of FEL running time, this translates to 60 days at 100% efficiency.

B. Schedule

A possible schedule to realization of the DarkLight experiment is as follows:

- DarkLight science case reaffirmed and technical design endorsed by PAC39 June 2012
- Successful initial test run July 2012
- FY2013 funds made available for technical design
- Technical review summer 2013
- DarkLight construction begins Fall 2013
- DarkLight detector commissioning begins in 2015
- DarkLight data taking begins 2016

VIII. SUMMARY

The DarkLight experiment provides a unique opportunity to search for the A' boson that could explain the origin of dark matter. DarkLight will be a challenging experiment, but an achievable one in the coming five years. Over the same time, results from cosmic ray and nuclear recoil experiments and the LHC may shape a new picture of dark matter, one in which DarkLight will play a key role.

This proposal has laid out a scientific case for DarkLight and shown the experiment is technically feasible at the Jefferson Lab Free Electron Laser. We are asking for an endorsement for DarkLight from PAC37 and PAC39 in order to move forward with the design of the experiment in the coming years. An endorsement of DarkLight will also enable us to begin discussions with Jefferson Lab and the agencies for support of the project.

Our formal beam-time request at the FEL request to carry out the measurement we have proposed is for the equivalent of 60 running days (assuming 100% accelerator efficiency) for data taking and the equivalent of 30 running days (assuming 100% efficiency) for beam studies, check-out and calibration.

Appendix A: Other Physics Capabilities

1. Searches for Invisible Decay Modes

DarkLight is designed to search for an A' boson through $ep \to epA' \to epe^+e^-$. We can also use the experiment to search for an invisibly decaying A', $ep \to epA'$, where we only observe the final state electron and proton. The dominant backgrounds are $ep \to ep\gamma$, $ep \to ep\gamma\gamma$, and pileup where we mis-reconstruct the outgoing 4-vectors from two or more different events. The irreducible background $ep \to ep\nu\nu$ is negligible at our beam energy of 100 MeV since we are so far from the Z pole. We will argue that dominant reducible background is $ep \to ep\gamma\gamma$, and hence our reach is dramatically improved by adding photon detection. The kinematics for the remaining background events, including pileup, are different enough from the signal that they can in principle be controlled.

For the remaining discussion, we consider the processes $e^-p \to e^-p\,x$, where $x = \gamma, \gamma\gamma, A'$, etc. We denote the incoming four-vectors as $p_{e^-} \equiv p_1, p_p \equiv p_2$, and the outgoing four-vectors as $p'_{e^-} \equiv p_3, p'_p \equiv p_4$. For most of the analysis, we assume *zero* photon detection efficiency (i.e. all photons are invisible); we make some comments at the end about how the reach improves with photon detection. We first consider possible backgrounds where only one event is seen during the timing window, and then consider the effects of pileup.

Single scattering backgrounds can be eliminated just by vetoing events with "missing invariant mass" equal to zero. Assuming full kinematic reconstruction, the quantity $(p_1+p_2-p_3-p_4)^2$ is strictly zero for an elastic event, or for a single photon event, $ep \to ep\gamma$. Indeed, with a 1 MeV invariant mass resolution, the number of these events which can fake an invariant mass of 10 MeV is well below the number of signal events given our design luminosity, and since DarkLight is only designed to search for $m'_A \gtrsim 10$MeV, we can ignore this background entirely. With zero photon detection efficiency, the main reducible background for the invisible search is two-photon bremsstrahlung, $ep \to ep\gamma\gamma$. The two photons can have a broad invariant mass spectrum, and the cross-section for this QED process is larger than the corresponding signal process $ep \to epA'$ by a factor of α/α'. Note that even with photon detection, the process $ep \to ep\gamma\gamma$ where both photons go down the beampipe cannot be reduced.

Next consider the case of pileup, where an elastic event $p_1 + p_2 \to p_3 + p_4$ and any other

event $p_1 + p_2 \to p_3' + p_4' + q$ (where q is not observed) occur during the same trigger window. Suppose the electron from the second event is mis-reconstructed as belonging to the elastic event:

$$p_1 + p_2 \to p_3' + p_4. \tag{A1}$$

Then, since $p_1 + p_2 = p_3 + p_4$ from four-momentum conservation in the elastic event, we have the missing invariant mass

$$\begin{aligned} m^2 &= (p_1 + p_2 - p_3' - p_4)^2 \\ &= (p_3 + p_4 - p_3' - p_4)^2 \\ &= (p_3 - p_3')^2 \\ &= 2m_e^2 - 2E_3E_3' + 2\sqrt{(E_3^2 - m_e^2)(E_3'^2 - m_e^2)}\cos\theta_{33'}, \end{aligned}$$

where $\theta_{33'}$ is the angle between the two outgoing electrons. It turns out that this expression is strictly non-positive, and is zero only when $E = E'$ and $\theta_{33'} = 0$, that is, when the two events have identical kinematics for the electrons. Identical arguments hold for the other mis-reconstructed event, with the electron mass, energies, and angles replaced by the corresponding quantities for the protons. Therefore, for pileup with any elastic event, the reconstructed invariant mass is non-positive and cannot contaminate the signal.

Thus, the dominant pileup background comes from coincident $ep \to ep\gamma$ events. We now give a sketch of a vetoing procedure that can migigate this background for the invisible search. We assume exactly two events in the timing window, which is consistent with the average occupancy with the anticipated DarkLight collision rate, and leave a study of 3-event pileup to future work. For two events, we have the following final state possibilities:

- Background: ep/ep, $ep/ep\gamma$, $ep/ep\gamma\gamma$, $ep\gamma/ep\gamma$
- Signal: ep/epA', $ep\gamma/epA'$

Pileup of $ep\gamma\gamma$ with a signal event epA' is subdominant and so can be ignored in a first approximation. Assuming we see all four charged tracks, we now pair both electrons with both protons to form four invariant masses: m_{11}^2, m_{12}^2, m_{21}^2, and m_{22}^2, where m_{ij}^2 means the invariant mass from pairing electron i with proton j. A signal event is defined by having one of the masses, say m_{11}^2, equal to zero (from the elastic or single-photon event), and the other "diagonal" mass positive and equal to $m_{22}^2 = (m_{A'})^2$. We first veto any event where there is

no invariant mass greater than 10 MeV: by the missing invariant mass argument above, this eliminates the first two background processes, which contain elastic events with only zero or negative invariant masses. We then veto any remaining event with $m_{11}^2 > (10\text{MeV})^2$ and $m_{22}^2 \neq 0$. This gets rid of the $ep\gamma/ep\gamma$ events where one of the pairs fakes a large invariant mass, except in the case where the other pair happens to have exactly zero invariant mass to within our 1 MeV resolution. Finally, we can veto events with precisely three of the invariant masses are zero, which effectively removes the $ep\gamma$ pileup background. This leaves only $ep/ep\gamma\gamma$, which has the same kinematics as ep/epA'; we thus simply ignore the spurious negative or zero invariant masses, and count the single positive invariant mass, so $ep\gamma\gamma$ contributes as a background exactly as it does for non-pileup events.

Since we can effectively control pileup in principle, we estimate our experimental reach using only $ep\gamma\gamma$ as background. If we assume a nonzero photon detection efficiency ε, then the cross-section for the background scales as $(1-\varepsilon)^2$, since one would have to miss both photons in a $\gamma\gamma$ event in order for the background to fake a signal. (Of course, this simple picture is distorted somewhat when one or both photons leave the tracking region from $25^\circ - 165^\circ$.) But since the statistical fluctuations in the background scale as the square root of the number of background events, the overall reach increases approximately linearly with $1-\epsilon$. In other words, if the probability that we miss a photon drops by a factor of 2, then our reach improves by approximately a factor of 2 throughout the whole mass range. Taking into account the photon kinematics and requiring a 5σ signal-to-background significance, we find the reach for the invisible search shown in Figure 56.

The shaded areas represent excluded regions of parameter space from constrains on the electron and muon anomalous magnetic moment. The red line is the DarkLight reach for the e^+e^- search shown earlier in Figure 2. The green region represents the discrepancy between experimental and theoretical values for $(g-2)_\mu$, such that the discovery of an A' with mass and coupling within the band would explain the discrepancy. We see that even with modest (90%) photon detection efficiency, we can probe the vast majority of the preferred region.

2. Measurement of the proton charge radius using $e-p$ scattering

The electromagnetic form factors of the proton at low Q^2 have long been one of the interesting measurements in the standard model. Such measurements have gained renewed

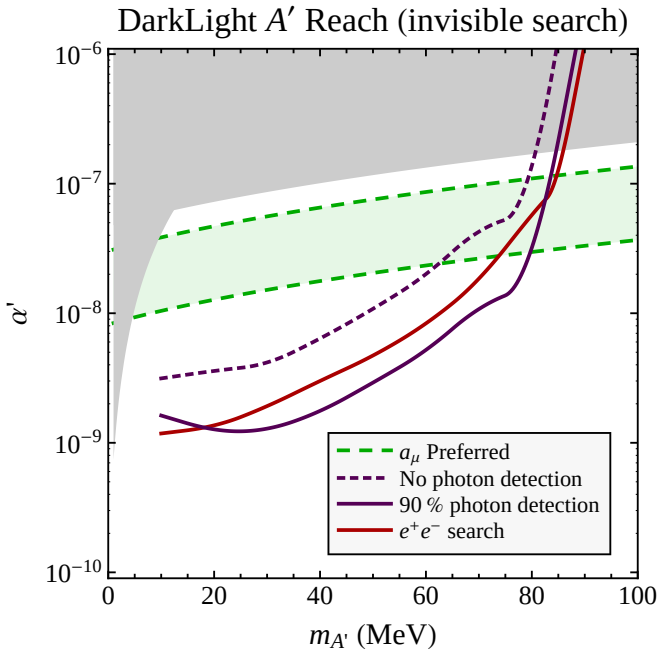

FIG. 56: DarkLight reach for invisibly decaying A'

interest with the recent measurement of the muonic Lamb shift [62] from which a proton charge radius was extracted that is seven standard deviations smaller than the best determination from previous extractions using *ep* scattering data [63–65] and determinations from spectroscopy of electronic hydrogen [66–68]. Since the proton charge radius $\langle r_p^2 \rangle$ is defined in terms of the slope of the electric form factor $G_p^E(Q^2)$ as

$$\langle r_p^2 \rangle = -6 \left. \frac{\mathrm{d}G_p^E(Q^2)}{\mathrm{d}Q^2} \right|_{Q^2=0}$$

precise and accurate measurements of $G_p^E(Q^2)$ can be used to extract the proton charge radius and compare to the recent measurements.

With an electron beam energy of 100 MeV and an electron acceptance between 25° and 165°, DarkLight is sensitive to Q^2 values in ep elastic scattering between 0.0019 $(\mathrm{GeV}/c)^2$, a factor of 2 smaller value than [65], and 0.033 $(\mathrm{GeV}/c)^2$, with even lower values accessible with a lower beam energy and extended forward acceptance.

Using a model for G_p^M, the proton charge radius can be extracted from a measurement at one energy alone, since the cross section at forward angles and low Q^2 is dominated by the electric form factor.

A variation of the beam energy will allow us to separate the form factors using the

Rosenbluth technique model independently. The comparatively small Q^2 values even at backward angles give us the opportunity to determine both G_p^E and G_p^M with good precision in this low Q^2 regime, where only few reliable data points exist. Such a separation would also yield precise charge and magnetization radii. While it is hard to determine the absolute cross section with uncertainties small enough to add a meaningful data set to the world data, it should be possible to fix the global normalization with an extrapolation of the cross section or of the form factors to $Q^2 = 0$, where their values are known, a method already used in [65].

[1] V. C. Rubin and W. K. Ford, Jr., Astrophys. J. **159**, 379 (1970).

[2] J. K. Adelman-McCarthy et al. (SDSS), Astrophys. J. Suppl. **162**, 38 (2006), astro-ph/0507711.

[3] E. Komatsu et al. (WMAP), Astrophys. J. Suppl. **180**, 330 (2009), 0803.0547.

[4] U. G. Briel and J. P. Henry (1997), astro-ph/9711237.

[5] D. P. Finkbeiner and N. Weiner, Phys. Rev. **D76**, 083519 (2007), astro-ph/0702587.

[6] M. Pospelov, A. Ritz, and M. B. Voloshin, Phys. Lett. **B662**, 53 (2008), 0711.4866.

[7] N. Arkani-Hamed, D. P. Finkbeiner, T. R. Slatyer, and N. Weiner, Phys. Rev. **D79**, 015014 (2009), 0810.0713.

[8] Y. Nomura and J. Thaler (2008), 0810.5397.

[9] D. P. Finkbeiner (2004), astro-ph/0409027.

[10] D. Hooper, D. P. Finkbeiner, and G. Dobler, Phys. Rev. **D76**, 083012 (2007), 0705.3655.

[11] O. Adriani et al. (PAMELA), Nature **458**, 607 (2009), 0810.4995.

[12] A. A. Abdo et al. (The Fermi LAT), Phys. Rev. Lett. **102**, 181101 (2009), 0905.0025.

[13] F. Aharonian et al. (H.E.S.S.), Phys. Rev. Lett. **101**, 261104 (2008), 0811.3894.

[14] F. Aharonian et al. (H.E.S.S.) (2009), 0905.0105.

[15] G. Weidenspointner et al., Astron. Astrophys. **450**, 1013 (2006), astro-ph/0601673.

[16] J. Knodlseder et al., Astron. Astrophys. **411**, L457 (2003), astro-ph/0309442.

[17] R. Bernabei et al. (DAMA), Eur. Phys. J. **C56**, 333 (2008), 0804.2741.

[18] P. Meade, M. Papucci, and T. Volansky (2009), 0901.2925.

[19] J. Mardon, Y. Nomura, and J. Thaler, Phys. Rev. **D80**, 035013 (2009), 0905.3749.

[20] P. Meade, M. Papucci, A. Strumia, and T. Volansky (2009), 0905.0480.

[21] M. Davier, A. Hoecker, B. Malaescu, and Z. Zhang, Eur.Phys.J. **C71**, 1515 (2011).

[22] N. Borodatchenkova, D. Choudhury, and M. Drees, Phys. Rev. Lett. **96**, 141802 (2006), hep-ph/0510147.

[23] P. Fayet, Phys. Rev. **D75**, 115017 (2007), hep-ph/0702176.

[24] B. Batell, M. Pospelov, and A. Ritz (2009), 0903.0363.

[25] R. Essig, P. Schuster, and N. Toro (2009), 0903.3941.

[26] M. Reece and L.-T. Wang (2009), 0904.1743.

[27] D. E. Morrissey, D. Poland, and K. M. Zurek (2009), 0904.2567.

[28] P.-f. Yin, J. Liu, and S.-h. Zhu (2009), 0904.4644.

[29] E. M. Riordan et al., Phys. Rev. Lett. **59**, 755 (1987).

[30] A. Bross et al., Phys. Rev. Lett. **67**, 2942 (1991).

[31] J. D. Bjorken, R. Essig, P. Schuster, and N. Toro (2009), 0906.0580.

[32] R. Essig, P. Schuster, N. Toro, and B. Wojtsekhowski, JHEP **1102**, 009 (2011), 1001.2557.

[33] Y. Kahn, M. Schmitt, and T. M. P. Tait, Phys. Rev. **D78**, 115002 (2008), 0712.0007.

[34] M. Pospelov (2008), 0811.1030.

[35] E. Abouzaid et al. (KTeV), Phys. Rev. **D75**, 012004 (2007), hep-ex/0610072.

[36] B. Wojtsekhowski, AIP Conf. Proc. **1160**, 149 (2009), 0906.5265.

[37] G. Neil, C. Bohn, S. Benson, G. Biallas, D. Douglas, et al., Phys.Rev.Lett. **84**, 662 (2000).

[38] C. Tennant, *Th3pbi03, proceedings of pac09* (2009).

[39] A. Chao, *The Physics of Collective Beam Instabilities in High Energy Accelerators* (John Wiley and Sons, 1993).

[40] K. Bane and M. Sands, *The short-range resistive wall wake fields* (1995).

[41] J. Wang and J. Wu, Phys. Rev. ST Accel. Beams **7**, 034402 (2004).

[42] *Proceedings of the ERL07* (2007).

[43] *Proceedings of the ERL09* (2009).

[44] S. Zhang, *Proceedings of the erl workshop, cornell* (2009).

[45] D. Hasell, T. Akdogan, R. Alarcon, W. Bertozzi, E. Booth, et al., Nucl.Instrum.Meth. **A603**, 247 (2009).

[46] D. K. Hasell, R. G. Milner, R. P. Redwine, R. Alarcon, H. Gao, et al., Ann.Rev.Nucl.Part.Sci. **61**, 409 (2011).

[47] T. O. Collaboration, URL `Seehttp://web.mit.edu/olympus`.

[48] P. Balakrishnan et al., *A proposal for the darklight experiment at the jefferson laboratory free electron laser, pac37* (2010).

[49] T. P. Collaboration, *Technical design report for the central tracking system of the panda experiment* (2011).

[50] M. Freytsis, G. Ovanesyan, and J. Thaler (2009), 0909.2862.

[51] B. Ketzer, *Development of a high-rate gem-tpc, presentation to i3hp2 jointgem meeting* (2011).

[52] F. Bohmer, H. Angerer, S. Dorheim, C. Hoppner, B. Ketzer, et al., Nucl.Phys.Proc.Suppl.

215, 278 (2011).

[53] C. Hearty et al., *,t2k nd280 tpc technical design report version1.0 t2k internal note.*

[54] E. Baron et al., *After, an asic for the readout of the large t2k time projection chamber.*

[55] H. Huang et al., *Conf. proc. c0806233* (2008).

[56] C. Van Hulse et al. (HERMES), Nucl. Inst. and Meth A **623**, 359 (2010).

[57] R. Back et al., Nucl. Inst. and Meth. A **447**, 257 (2000).

[58] S. Margetis, Acta Phys. Polon. Supp. **3**, 1009 (2010).

[59] A. Hershcovitz, Journal of Applied Physics **78** (1995).

[60] W. Leo, *Techniques for Nuclear and Particle Physics Experiments* (Spring, 1987).

[61] R. M. Sternheimer, S. M. Seltzer, and M. J. Berger, Phys. Rev. B (1982).

[62] M. Pohl and D. Eichler, PoS **TEXAS2010**, 135 (2010).

[63] I. Sick, Phys.Lett. **B576**, 62 (2003), nucl-ex/0310008.

[64] P. G. Blunden and I. Sick, Phys.Rev. **C72**, 057601 (2005), nucl-th/0508037.

[65] J. C. Bernauer, P. Achenbach, C. Ayerbe Gayoso, R. Böhm, D. Bosnar, L. Debenjak, M. O. Distler, L. Doria, A. Esser, H. Fonvieille, et al. (A1 Collaboration), Phys. Rev. Lett. **105**, 242001 (2010), URL `http://link.aps.org/doi/10.1103/PhysRevLett.105.242001`.

[66] K. Melnikov and T. van Ritbergen, Phys. Rev. Lett. **84**, 1673 (2000), URL `http://link.aps.org/doi/10.1103/PhysRevLett.84.1673`.

[67] T. Udem, A. Huber, B. Gross, J. Reichert, M. Prevedelli, et al., Phys.Rev.Lett. **79**, 2646 (1997).

[68] P. J. Mohr, B. N. Taylor, and D. B. Newell, Rev. Mod. Phys. **80**, 633 (2008), URL `http://link.aps.org/doi/10.1103/RevModPhys.80.633`.